Surface/Interface Modulation of Hematite-based Photoanodes for Efficient Photoelectrochemical Water Oxidation

（表面/界面構造制御によるヘマタイト系光電極の効率的な水の酸化反応に関する研究）

Gaoliang YANG

Graduate School of Chemical Sciences and Engineering

Hokkaido University

2021

Contents

Contents I

Abstract 1

Chapter 1 Introduction 3

1.1 General introduction of photoelectrochemical water splitting 3

1.2 Properties of n-type α-Fe_2O_3 5

1.3 General strategies to improve the PEC performance of α-Fe_2O_3 6

1.3.1 Morphology control 7

1.3.2 Element doping 8

1.3.3 Heterojunction construction 9

1.3.4 Surface modification 10

1.3.4.1 Passivation overlayers 11

1.3.4.2 Co-catalysts 12

1.3.5 Interface modulation between α-Fe_2O_3 and co-catalysts 15

1.3.5.1 Different mediators to modulate the interfacial charge transfer 16

1.3.5.2 Carbon-based co-catalysts for PEC water oxidation 19

1.3.5.3 Interfacial engineering between α-Fe_2O_3 and carbon-based co-catalysts 22

1.4 Thesis motivations and organization 23

References 26

Chapter 2 Ultrathin cobalt-manganese nanosheets: an efficient platform for enhanced photoelectrochemical water oxidation with electron-donating effect 32

2.1 Introduction 32

2.2 Experimental section 33

2.2.1 Materials preparation 33

2.2.2 Material characterization 34

2.2.3 Photoelectrochemical measurement 34

Contents

2.3 Results and discussion 37

2.3.1 The optimization of Co-Mn nanosheets 37

2.3.2 Characterization of the modified films with Co-Mn nanosheets 40

2.3.3 PEC performance characterization 45

2.3.4 Research on catalytic mechanism 52

2.4 Conclusions 58

References 58

Chapter 3 A universal strategy boosting photoelectrochemical water oxidation by utilizing MXene nanosheets as hole transfer mediators 63

3.1 Introduction 63

3.2 Experimental section 65

3.2.1 Materials preparation 65

3.2.2 Material characterization 66

3.2.3 Photoelectrochemical measurement 66

3.3 Results and discussion 68

3.3.1 Synthesis and characterization of MXene nanosheets (MNs) 68

3.3.2 Characterization of modified photoanodes 72

3.3.3 PEC performance of different photoanodes 76

3.3.4 Research on the catalytic mechanism 82

4.4 Conclusions 91

References 92

Chapter 4 Constructing chemical interaction between hematite and carbon nanosheets with single active sites for efficient photoelectrochemical water oxidation 95

4.1 Introduction 95

4.2 Experimental section 96

4.2.1 Material preparation 96

4.2.2 Material characterization 97

4.2.3 Photoelectrochemical measurements 98

Contents

4.3 Results and discussion 100

4.3.1 Characterization of the Ni-NC catalyst 100

4.3.2 Characterization of the modified films with Ni-NC 106

4.3.3 PEC performance of different photoanodes 110

4.3.4 Research on catalytic mechanism 114

3.4 Conclusions 124

References 125

Chapter 5 Conclusions and future prospects 129

5.1 General conclusions 129

5.2 Future prospects 131

Acknowledgement 133

Abstract

Photoelectrochemical (PEC) water splitting is a promising approach for direct conversion of solar energy to hydrogen. Among various semiconductors, hematite (α-Fe_2O_3) has emerged as an excellent photoanode material due to its significant light absorption, chemical stability in aqueous solutions, and earth abundant property. However, its performance has been crucially limited by poor optoelectronic properties and sluggish reaction kinetics for water oxidation. Two essential criteria, including sufficient targeted reaction sites and efficient interfacial charge transfer, should be considered to enhance the performance of hematite-based photoanodes. Thus, this thesis focused on rationally designing efficient co-catalysts with modulated active sites as well as interface engineering by inserting hole transfer mediators/constructing direct chemical interaction between α-Fe_2O_3 and co-catalysts.

In chapter 1, a general background about photoelectrochemistry and a simple overview of α-Fe_2O_3 photoanodes is introduced. Then, the recent development of modulation strategies to promote the PEC performance of α-Fe_2O_3 is summarized.

In chapter 2, an ultrathin cobalt-manganese (Co-Mn) nanosheet, consisting of amorphous $Co(OH)_x$ layers and ultrasmall Mn_3O_4 nanocrystals, is designed as an efficient co-catalyst on α-Fe_2O_3 film for PEC water oxidation. The uniformly distributed Co-Mn nanosheets lead to a remarkable 2.6-fold enhancement on the photocurrent density at 1.23 V vs. reversible hydrogen electrode (RHE) and an impressive cathodic shift (~200 mV) of onset potential compared with bare α-Fe_2O_3 film. Furthermore, the decorated photoanode exhibits a prominent resistance against photo-corrosion with an excellent stability for over 10 h. Detailed mechanism investigation manifests that incorporation of Mn sites in the nanosheets could create electron donation to Co sites and facilitate the activation of OH group, which drastically increases the catalytic activities for water oxidation. These findings provide valuable guidance for designing high-performance co-catalysts for PEC applications and open new avenues towards controlled fabrication of mixed metallic composites.

In chapter 3, in order to reinforce the interfacial interaction at the α-Fe_2O_3/co-catalyst interface, a novel charge transfer system for PEC water oxidation is designed by inserting MXene nanosheets (MNs) between α-Fe_2O_3 and co-catalyst. In this system, MNs act as

the hole transfer mediators to efficiently suppress the interfacial charge recombination owing to the high hole mobility of MNs and the formation of built-in electric field at the MNs/α-Fe_2O_3 junction. Meanwhile, the co-catalyst layers, in turn, can protect the MNs from oxidation to achieve a prominent stability. The optimized photoanode of Co-Pi/MNs/α-Fe_2O_3 can achieve a remarkable photocurrent density, up to 3.20 mA cm^{-2} at 1.23 V vs. reversible hydrogen electrode (RHE) under AM 1.5 G illumination. An impressive cathodic onset potential shift of ~250 mV is obtained with the synergistic effect of MNs and co-catalyst (Co-Pi). Furthermore, this strategy is also applicable to other photoanode materials, such as $BiVO_4$, WO_3 and ZnO, verifying the versatility by utilizing the MNs as hole transfer mediators for efficient photogenerated charge separation to enhance the PEC water oxidation.

In chapter 4, direct chemical interaction is constructed at the interface of α-Fe_2O_3 and carbon nanosheets with single-nickel sites (Ni-NC) to accelerate the reaction kinetics by providing additional charge transport channels and abundant active sites. The interfacial carrier path induced by the chemical coupling and the efficient single-nickel sites work collaboratively, achieving an impressive photocurrent density of 1.85 mA cm^{-2} at 1.23 V vs. RHE, up to 2.2 times higher than that of pure α-Fe_2O_3. These findings shed light on an interface modulation strategy and provide an alternative towards utilizing unique single active sites for efficient photoelectrochemical water splitting.

In chapter 5, an overall summary of this dissertation work was presented. This thesis carried out a systematic study on the surface modification of hematite-based photoanodes for efficient photoelectrochemical water oxidation. In α-Fe_2O_3-based PEC water oxidation system, co-catalysts decoration has been demonstrated to be the most efficient way to lower the reaction barrier and promote charge injection to the reactants. And the delicate modification of the interface between the α-Fe_2O_3 and the co-catalysts is critical for promoting charge transfer from the bulk of α-Fe_2O_3 to the co-catalysts, which can directly influence the surface catalysis. The relevant findings in this study deepen the understanding of α-Fe_2O_3-based PEC water oxidation system and highlight the importance of semiconductor/co-catalyst interface modulation for the overall photoelectrocatalytic processes.

Chapter 1 Introduction

1.1 General introduction of photoelectrochemical water splitting

The exploitation of clean and sustainable energy sources has been regarded as a top priority for the human society as the increasing demand for the finite fossil fuel and the ensuing environmental problems.[1] Inexhaustible solar energy is one of the most promising candidates to alleviate these issues, as the solar energy supplied to the earth surface (173000 TW) is much larger than the total global energy consumption (17.91 TW in 2017).[2-3] However, the intermittency of solar energy together with the temporal and geographical divergence means that it is urgently needed to develop efficient strategies for the harvesting and storage. Accordingly, there are several technologies to covert the solar energy into the chemical energy, among which, photoelectrochemical (PEC) water splitting, using the earth abundant semiconductors to produce the clean hydrogen energy with zero emission, is one of the ultimate solutions for the solar energy conversion revolution.[4-5]

Water splitting reaction (generating H_2 and O_2 molecules) is energetically uphill, requiring a standard free energy change (ΔG^o) of 237.2 kJ mol^{-1}, or a potential of 1.23 V for each electron (according to the Nernst equation). So the water reduction reaction needs two electrons, while four holes are required to produce the O_2 molecule according to equation (2) and (3):

light absorption: $SC + h\nu \left(\geq E_g\right) \rightarrow e_{cb}^- + h_{vb}^+$ (1)

oxygen evolution reaction (OER): $2H_2O + 4h_{vb}^+ \rightarrow O_2 + 4H^+$ (2)

hydrogen evolution reaction (HER): $4H^+ + 4e_{cb}^- \rightarrow 2H_2$ (3)

overall water splitting: $2H_2O \rightarrow 2H_2 + O_2$ $\Delta G^o = 237.2$ kJ mol^{-1} (4)

As shown in Figure 1.1, to drive this reaction with light by a semiconductor (SC), the photons should supply energy greater than 1.23 eV to excite charge carriers from the bulk of semiconductor and conduct redox reactions at the surface sites. Actually, the photons are provided from the sunlight with the spectrum presented in Fig. 1.1a. Thus, the bandgap (E_g) of a semiconductor must be large enough to provide the energy for water splitting, while the band positions should be located appropriately to drive the two half reactions by photogenerated electrons (e_{cb}^-) and holes (h_{vb}^+) upon light illumination.[6]

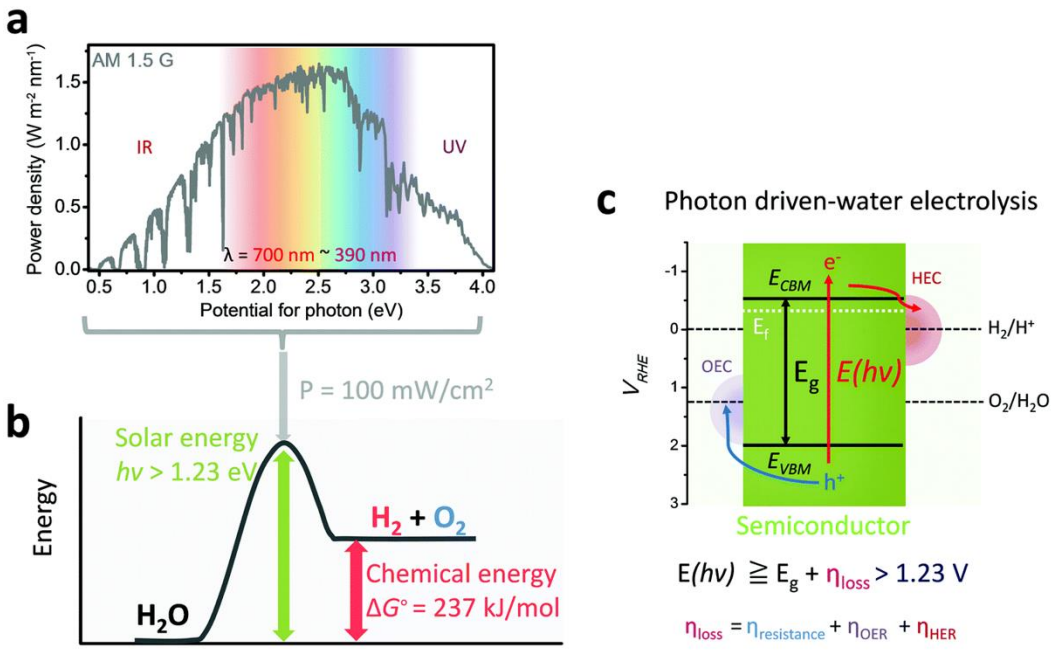

Figure 1.1 a) Spectrum of AM 1.5 G illumination (1 sun condition with power density of 100 mW cm^{-2}). b) The kinetics progress of PEC water splitting (an energetically uphill reaction). c) Excitation processes of electron/hole pairs by light of sufficient energy (hν ≥ E_g) for redox reactions of overall water splitting.[7]

A typical PEC cell for water splitting is composed of two connected electrodes immersed in a suitable electrolyte, in which at least one should be photoelectrode with a semiconductor to absorb the light. As shown in Figure 1.2, when the semiconductor harvests photons with energy equal to/higher than its bandgap, electrons will be excited from the valence band (VB) to the unoccupied conduction band (CB), leaving the holes in the VB. Then the excited electrons are collected by the conducing substrate, withdrawn over the external circuit and finally arrive at the cathode for HER, while the corresponding holes diffuse to the surface of photoanode and participate in the water oxidation reaction. In practical condition, serious recombination will be occurred after the excitation of charge carriers from the photoelectrode, thus a bias should be applied to the PEC system as an assistance to promote the migration of the charge carriers and suppress the unnecessary recombination.[8] The objective of the PEC device is producing the largest photocurrent with a minimum bias. This could be achieved by maximizing light absorption using a semiconductor with an appropriate E_g and minimizing the loss of charges due to bulk/surface recombination by proper modifications of the semiconductor.[9]

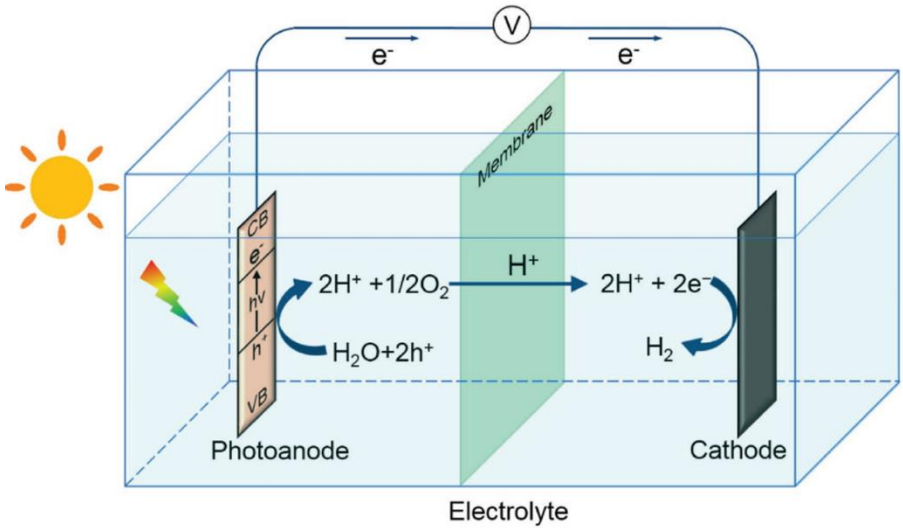

Figure 1.2 A sketch of the typical PEC cell for water splitting with an n-type semiconductor as the photoanode and a metallic cathode.[10]

Therefore, for the semiconductors that should be employed as the electrode in a PEC water splitting system, several prerequisites need to fulfill as below. Firstly, the band gap of semiconductor should be suitable to drive the reaction through absorbing the visible part of the solar light. Secondly, the VB top for an n-type semiconductor (or CB bottom for a p-type semiconductor) should be high enough to drive the water oxidation (or reduction) reaction. Thirdly, the compositions of the semiconductor should be earth-abundant with low cost. Finally, the materials should be stable under the harsh conditions for water splitting. However, it is usually difficult to achieve overall water splitting on a single semiconductor, even if its band structure meets the thermodynamic requirements for reaction. In addition, compared to water reduction, water oxidation is considered as the rate-limiting step for water splitting due to the higher energy barrier and complex four-electron processes. Therefore, the development for effective photoanodes is indispensable.

1.2 Properties of n-type α-Fe_2O_3

Since the first demonstration of PEC water splitting with TiO_2 in 1972, extensive efforts have been devoted to the development of various materials for photoanodes.[11] Because of the wide bandgap (3.0-3.2 eV), the pure TiO_2 can only harvest the ultraviolet (UV) light, which only accounts for about 4% of the solar energy. Therefore, the theoretical solar-to-hydrogen (STH) efficiency can only reach ~2% under the solar illumination, severely impeding the effective utilization of solar energy. Similar

limitations could be applied into other wide-bandgap photoanode materials, such as ZnO,[12] Ta_2O_5[13] and WO_3.[14] Therefore, it is significantly important to develop the semiconductors that can utilize the visible light to achieve sustainable utilization of solar energy.

Hematite (α-Fe_2O_3), with a suitable bandgap of 2.0-2.2 eV and a theoretical maximum STH efficiency of ~16%, has emerged as one of the most promising photoanode materials.[15-16] Compared with other semiconductors with a narrow bandgap, several additional advantages, such as high chemical stability in alkaline environment, nontoxicity and low cost, endow α-Fe_2O_3 a huge potential for the proof-of-concept demonstration of water splitting as the photoanode.[15, 17] However, the gases evolution rates and STH efficiency of α-Fe_2O_3 are usually much lower than the theoretical values in practical application owing to some intrinsic disadvantages. Firstly, the poor charge mobility (in the order of 10^{-2} cm^2 V^{-1} s^{-1}) and extremely short hole diffusion length (~2–4 nm) are significantly limiting the charge separation and injection efficiency of α-Fe_2O_3 for the PEC water oxidation.[18] Secondly, the slow sluggish kinetics for the targeted reaction (OER) and a high density of surface states result in a low reaction activity and require a larger external bias to drive the reaction at the electrode. Generally, an external bias of 0.3-0.4 V vs. RHE is enough to initiate the water oxidation based on the reported flat band potential for α-Fe_2O_3, which is much different from the observed onset potential of 0.8-1.0 V vs. RHE for the single α-Fe_2O_3 electrode in the alkaline electrolyte.[15] The remaining overpotential of ~0.5-0.6 V vs. RHE is the major drawback for the practical application of α-Fe_2O_3-based PEC system, which can be attributed to the abundant surface states and sluggish reaction kinetics. Therefore, it is urgently needed to develop delicate modification methods to overcome these limitations and thus achieve an efficient hematite-based PEC water splitting system.

1.3 General strategies to improve the PEC performance of α-Fe_2O_3

To address the limitations of α-Fe_2O_3 for PEC water splitting, significant efforts have been devoted to facilitating the charge transfer and promoting the reaction kinetic of this material over the past decades. Nanostructure engineering, such as nanorods and nanotubes can favor efficient charge collection and thus results in enhanced α-Fe_2O_3-based PEC water splitting activity.[19-20] Elemental doping is a simple and effective strategy to enhance the intrinsic conductivity of α-Fe_2O_3.[21-22] However, these two approaches still utilize a single material to conduct light absorption and charge transport.

Serious charge recombination may still exist to reduce the achievable efficiencies. Alternatively, hematite-based heterostructures are constructed by combining α-Fe_2O_3 with a second semiconductor for promoted charge separation, a surface passivation layer for reduced surface charge recombination, or a co-catalyst for accelerated water oxidation kinetics. Nevertheless, the introduction of the second phase on the surface of α-Fe_2O_3 will generate a new interface, which is extremely crucial for the separation and migration of photogenerated charge carriers between these two components. Thus the surface/interface modulation on the α-Fe_2O_3-based PEC system is necessary to boost the charge transfer for efficient water oxidation.

1.3.1 Morphology control

As mentioned, the short diffusion length of photogenerated holes greatly limits the performance of α-Fe_2O_3-based photoanodes. Accordingly, the harvesting depth of charge carriers would be seriously restricted and thus the holes generated in the bulk would be recombined before reaching to the surface sites for the reaction.[23] In this case, the ideal morphology of α-Fe_2O_3 should be thin enough to achieve a high efficiency. However, this ultrathin structure of the α-Fe_2O_3 results in a low absorption efficiency, which could be overcome by the method of stacking multiple layers in tandem, as suggested by Itoh and Bockris in 1984.[24] Although the stacking method can fundamentally solve the absorption issue, the high cost and cumbersome processes make it difficult to implement in practice. In recent years, nanostructuring of α-Fe_2O_3 for PEC water oxidation has attracted significant attentions.[25] The nanostructured materials are supposed to expose more surface area to the electrolyte, which is favorable for efficient transfer of charge carriers.[26-28] However, serious charge recombination would still occurred across the grain boundaries between particles in nanoparticles and mesoporous films.[29] One dimensional (1D) nanostructures with high aspect ratios (nanowires, nanorods or nanotubes) can enhance the collection for the charge carrier and reduce the recombination rates at the grain boundaries.[30] Furthermore, the smaller diameters of 1D nanostructures would shorten the diffusion distance of holes to the semiconductor/electrolyte interface, thereby avoiding the serious recombination during the transport process. For instance, Beermann et al. utilized hematite nanorod arrays as photoanodes for water oxidation, which allowed more efficient transport of photogenerated charge carriers through a designed route compared to the sintered spherical particles. The relatively high efficiency was attributed to the better electron transport along the nanorodsand a directed movement

of the electrons toward the back contact. [31] As reported by Warren's group with a detailed comparison of nanofilm and 1D nanostructures of α-Fe_2O_3, a better photo-response could be obtained by the 1D nanostructured electrode for water oxidation.[32] Cauliflower nanostructures grown via atmosphere pressure chemical vapor deposition (APCVD) have shown significantly improved performances and made nanostructured hematite become a more promising photoanode material. As reported by Andreas et al., the cauliflower-like nanostructure minimized the diffusion distance of photogenerated holes to the α-Fe_2O_3/electrolyte interface, while still thick enough for efficient light absorption.[27] Until now, several different approaches have been taken to prepare nanostructured α-Fe_2O_3 for PEC water splitting application and further work on the nanostructuring should be emphasized on the facile synthesis processes with high solar utilization efficiencies.[15]

1.3.2 Element doping

Foreign element doping is a prevalent and effective strategy to enhance the intrinsic conductivity of α-Fe_2O_3 by increasing the carrier density in the bulk and promoting the charge transfer ability.[21-22] As mentioned in 1.2, the pristine α-Fe_2O_3 has a low carrier concentration and hole mobility, leading to a poor electrical conductivity. Since the intrinsic conductivity of the semiconductor is depending on the motion of charge carriers in the bulk, increasing the sum of carriers by doping is generally used to compensate for the low carrier mobility.[33] Owing to the intrinsic defects from the host lattice, such as the oxygen vacancies, α-Fe_2O_3 exhibits n-type semiconductor properties. Therefore, the n-type dopants (metal ions of +4 or +5) will induce the enhancement of donor levels and thereby improve the charge separation, while the p-type dopants (metal ions of charge lower than +3) will increase the positive charge carriers and then convert the α-Fe_2O_3 to p-type.[34]

So far, varieties of dopants have been tried to modify the properties of α-Fe_2O_3, among which Ti and Sn are most widely used for improving the performance of α-Fe_2O_3. Pu et al. found that Ti-doping and generated oxygen vacancies in α-Fe_2O_3 could achieve superior water oxidation activity. The oxygen vacancies could improve the donor density, while Ti-doping provided more active sites for water oxidation with enhanced surface catalytic effects.[35] Zandi et al. deposited uniform thin Ti-doped α-Fe_2O_3 film on fluorine doped SnO_2 (FTO) glass using atomic layer deposition (ALD). The ALD technique allowed precise control of the morphology and thickness of α-Fe_2O_3 films. And the

incorporation of Ti dopant atoms into hematite electrodes could improve the hole diffusion length and water oxidation efficiency.[36] Sn has also been doped into hematite to boost its conductivity. Ling et al. developed Sn-doped hematite nanocorals with a remarkable photocurrent density, owing to the improved carrier density and optimized structural morphology.[37] The p-type α-Fe_2O_3 could be prepared by doping with divalent metal dopants, which could replace Fe^{3+} in the lattice and forming hole carriers.[38-39] Another way of doping for α-Fe_2O_3 could create oxygen vacancies artificially by some treatments, which is named as "self-doping". The Fe^{2+} sites in hematite could significantly increase the conductivity of the material through a polaron hopping mechanism.[40] Ling et al. fabricated self-doped hematite nanowire arrays through thermal decomposition of β-FeOOH in an oxygen-deficient atmosphere. The enhanced activity was owing to the increased donor density resulting from the formation of oxygen vacancies.[41]

1.3.3 Heterojunction construction

As discussed, the extremely short carrier diffusion length is the inherent limitation for α-Fe_2O_3, although the nanostructuring strategy has addressed this issue to a certain extent. There is still a great chance of recombination along the charge transfer path in the nanostructured α-Fe_2O_3. This limitation can be overcome by coupling α-Fe_2O_3 with a second semiconductor, which should have a proper band structure to fabricate a heterojunction.[42] The charge recombination between two semiconductors would be suppressed due to the formation of an internal electric field at the heterojunction interface.[8] The light absorption of α-Fe_2O_3 can be also improved by forming heterojunctions with small band gap semiconductors, which are mainly responsible for enhancing the visible light absorption of α-Fe_2O_3 electrode.[34]

As a typical heterostructure, delicately designed WO_3/α-Fe_2O_3 architectures have been intensively studied for PEC water oxidation.[43-44] WO_3 has suitable band positions and electronic properties to form a type-II junction with α-Fe_2O_3.[45] Thus, cascadal electron injection from α-Fe_2O_3 to WO_3 is expected, which improves the charge separation efficiency. For example, Sivula et al. deposited a thin layer of α-Fe_2O_3 nanoparticles on nanostructured WO_3 scaffold. An enhanced photocurrent density was obtained for WO_3/α-Fe_2O_3 photoanodes, which could be attributed to a greater light absorption.[44] As another example, a ZnO@α-Fe_2O_3 core/shell electrode displayed excellent performance for PEC water oxidation, with a doubling photocurrent and greater stability. This heterojunction structure would increase the surface band bending and reduce the flat-band

potential.[46] Similarly, Mayer et al. deposited an α-Fe_2O_3 overlayer on the Si nanowires, forming a Si/α-Fe_2O_3 dual-absorber system. The Si nanowires could extend the absorption region for the solar energy and provide additional photovoltage to assist PEC water splitting by hematite, thus exhibiting greatly enhanced PEC performance.[47] Finally, a p-type NiO nanoparticles was found to form a built-in electric field with the n-type α-Fe_2O_3. This system could reduce the overpotential for water oxidation, which was attributed to enhanced charge separation by the p-n junction and catalytic effect of NiO nanoparticles for water oxidation.[48]

1.3.4 Surface modification

For bare α-Fe_2O_3, the rate limiting step during the water oxidation processes should be the hole injection into the electrolyte.[49] Therefore, the surface charge recombination would severely limit the efficiency for water oxidation (Figure 1.3a), especially at low or without applied bias.[50] Surface modification is an effective way to improve the reaction kinetics and promote the hole transfer at the photoanode/electrolyte interface. The surface modification strategies including decoration of passivation overlayers and oxygen evolution co-catalysts. The sluggish hole transfer (injection) from the electrode to electrolyte can be improved by employing passivation layers (Figure 1.3b) or co-catalysts (Figure 1.3c) on the surface of the semiconductor. The fundamental mechanisms of these two approaches to enhance the PEC performance are totally different. Surface passivation is a non-catalytic process, reducing the rate of charge recombination by passivating the surface defects. And co-catalyst decoration usually signifies the oxidation of metallic elements in the co-catalyst, assisting hole transport from the surface to the electrolyte.

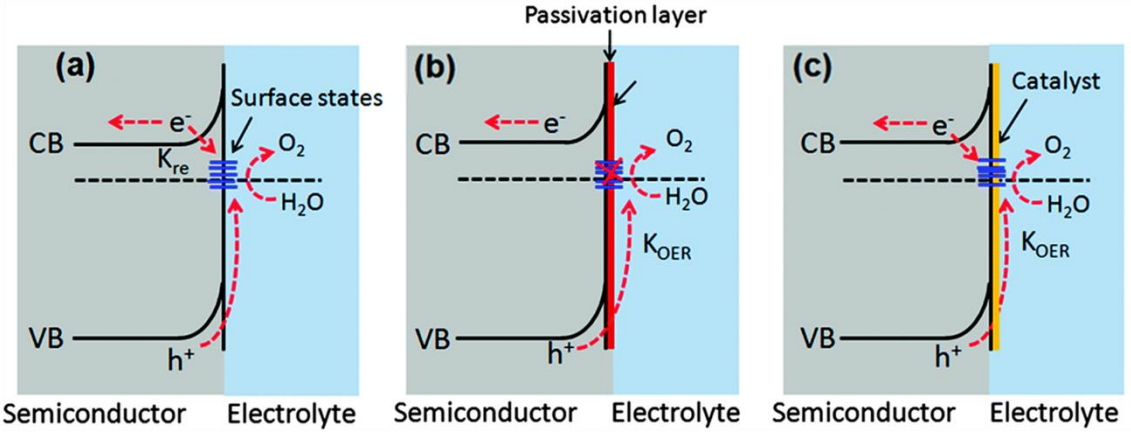

Figure 1.3 Comparison of the band energetics at the semiconductor/electrolyte interface for an n-type semiconductor. a) Inefficient water oxidation due to high charge

recombination at surface states. b) Non-catalytic passivation layers to suppress surface recombination. c) Co-catalyst layers to promote hole transfer and provide abundant reaction sites.[34]

1.3.4.1 Passivation overlayers

Typically, due to the oxygen vacancies or crystal defects, electronic states within the bandgap are produced on the surface of the oxide semiconductors, which are named as the surface states.[50] These surface states can trap charge carriers, leading to another favorable pathway for an indirect charge transfer with undesirable recombination. Thus, the water oxidation reaction would be occurred with the hole from the surface states, rather than the valence band.[51] As a consequence, hole accumulation at the surface states is essential for the water oxidation, thus the charge recombination at the surface states becomes the main limiting step for the PEC activity.[20, 52] An effective approach was developed to reduce the surface states by introducing a surface passivation layer, which were expected to reduce the charge recombination and enhance the charge transfer on the photoanodes, enabling high efficiency for PEC water oxidation.

Several noncatalytic oxide layers with wide bandgap have shown their potentials as the surface passivation layers, which could effectively reduce the surface states of α-Fe_2O_3. For example, Xi et al. found that the deposition of thin ZnO overlayers on the surface of α-Fe_2O_3 could reduce the onset potential and increase the photocurrent density, which could be attributed to the reduced surface defects and optimized flat-band potential.[53] Likewise, an ultrathin TiO_2 overlayer grown on the α-Fe_2O_3 by ALD method could significantly reduce the onset potential by ~100 mV. The enhanced performance was owing to reduced charge recombination, facilitated charge separation and larger photovoltage induced by the TiO_2 overlayer.[54] In particular, a Ga_2O_3 overlayer displayed a cathodically shifted onset potential by ~200 mV with an enhanced photocurrent density, attributing to the lower charge recombination in α-Fe_2O_3.[55] Similarly, Le Formal et al. discovered that the decoration of an ultra-thin Al_2O_3 on the nanostructured α-Fe_2O_3 could reduce the onset potential of ~100 mV and achieve a 3.5-fold enhancement on the photocurrent density at 1.0 V vs. RHE. More importantly, the addition of Co^{2+} ions as catalysts could further decrease the overpotential, suggesting that synergetic effect between the surface passivation strategies and catalytic approaches.[56] In this regards, it is applicable to employing surface passivation layers and catalysts sequentially, which is

a promising and practical strategy to achieve dramatic enhanced performance for PEC water splitting (more details are provided in Section 1.3.4.3).[57]

1.3.4.2 Co-catalysts

Due to the complex processes of four-electrons transfer, the OER is more difficult than the HER and is the rate-limiting step for the overall water splitting. And the reaction with sluggish kinetics should compete with the much faster charge recombination, resulting in a poor/moderate performance.[58] Therefore, loading co-catalysts with targeted active sites on the semiconductors is a necessary and useful way to boost the efficiency of PEC systems.[59] Generally, co-catalysts mainly play two pivotal roles during the PEC processes: (1) lowering the overpotential for water oxidation by providing a better pathway for photogenerated holes; (2) accelerating the charge separation and transfer across the semiconductor/co-catalyst junctions.[10] In addition, the suitable co-catalysts can efficiently suppress the photocorrosion of semiconductors during the water oxidation process.[60]

In general, several important requirements should be considered to develop efficient co-catalysts for the improved PEC water oxidation: (1) delicate design of active centers for activating and converting the H_2O molecules, with moderate adsorption strength of pivotal intermediates to achieve robust activity; (2) highly conductive to carrier, realizing fast injection of holes into the active sites for driving the reactions; (3) abundant surface functionalities to establish intimate interface connection with semiconductors for fast interfacial charge transport; (4) robust structural stability, enabling long-term operation under harsh experimental condition (5) the amount of the co-catalysts must be optimized, which should not block the light from reaching to the semiconductor.

As an effective strategy to accelerate the reaction kinetics of α-Fe_2O_3, co-catalysts decoration attracted great attention in recent years. So far, due to the excellent intrinsic ability for water oxidation, noble metal oxides such as RuO_2 and IrO_2,[61-62] are considered to be efficient water oxidation co-catalysts for improving the PEC water oxidation of α-Fe_2O_3. Grätzel et al. first deposited IrO_2 on the α-Fe_2O_3 photoanode, achieving a photocurrent of over 3 mA cm^{-2} at 1.23 vs RHE under AM 1.5 G illumination. The dramatic enhancement of the activity was attributed to the low kinetic barrier of IrO_2 for charge transfer, thereby lowing the overpotential for water oxidation.[63] Later, Li et al. deposited a heterogeneous multilayer of IrO_x on α-Fe_2O_3, which could be stable in acid

solution. This modified photoanode could decrease the onset potential by ~250 mV and maintain stable in acid electrolyte (pH 1.01) for 5 h.[64] Similarly, RuO_2 was also reported to reduce the onset potential of α-Fe_2O_3 by 120 mV, while photocurrent density kept unchanged.[65] Fan et al. constructed a novel semiconductor/molecule interface by immobilizing a molecular ruthenium co-catalyst on α-Fe_2O_3, achieving a 2-fold enhancement in photocurrent density compared with the bare α-Fe_2O_3.[66]

However, high cost and limited abundance of the noble metals seriously restrict their wide applications. As the alternatives to noble metal-based co-catalysts, many kinds of cost-effective transition-metal based co-catalysts have been exploited in recent years.[67] As the most common used water oxidation catalyst, since the first fabrication by Kanan et al. through a facile electrodeposition method,[68] cobalt phosphate (Co-Pi) has been extensively studied as the co-catalyst coupled with various photoanodes for efficient PEC water oxidation.[69-71] Zhong et al. improved the deposition method of Co-Pi via a photoassisted electrodeposition (PED) approach. Compared with the electrodeposition or wet impregnation, PED generated a more uniform distribution of Co-Pi onto α-Fe_2O_3, exhibiting a nearly 170 mV cathodic shift of the onset potential and a photocurrent density of 2.8 mA cm^{-2} at 1.23 V vs. RHE.[72] By utilization of impedance and transient photocurrent spectroscopies, Hanann and co-workers pointed out that the role of Co-Pi layers during the water oxidation could be summarized as below: efficiently collect and store photogenerated holes from the α-Fe_2O_3 photoanode, enhance charge separation, reduce surface recombination and provide abundant reaction sites.[73] However, Durrant et al. discovered an entirely different mechanism about the effect of Co-Pi layers for the enhanced PEC performance of α-Fe_2O_3 photoanodes. They synthesized mesoporous Si-doped α-Fe_2O_3 photoanode with cauliflower shape by the APCVD technique. The detailed transient study revealed that the Co-Pi could trap the photogenerated electrons from α-Fe_2O_3, instead of the hole storage effect reported by Hamann. Therefore, the Co-Pi layers just acted as the electron trapper, while the water oxidation occurred on the α-Fe_2O_3 surface with improved hole concentration.[55] The main reason for these two diverging perspectives could be attributed to the structural or morphological differences for their respective photoanodes. Therefore, different degree of interfacial contact and disordering may be existed between the α-Fe_2O_3 and Co-Pi in these two cases, resulting in the different charge transfer behaviors.[74]

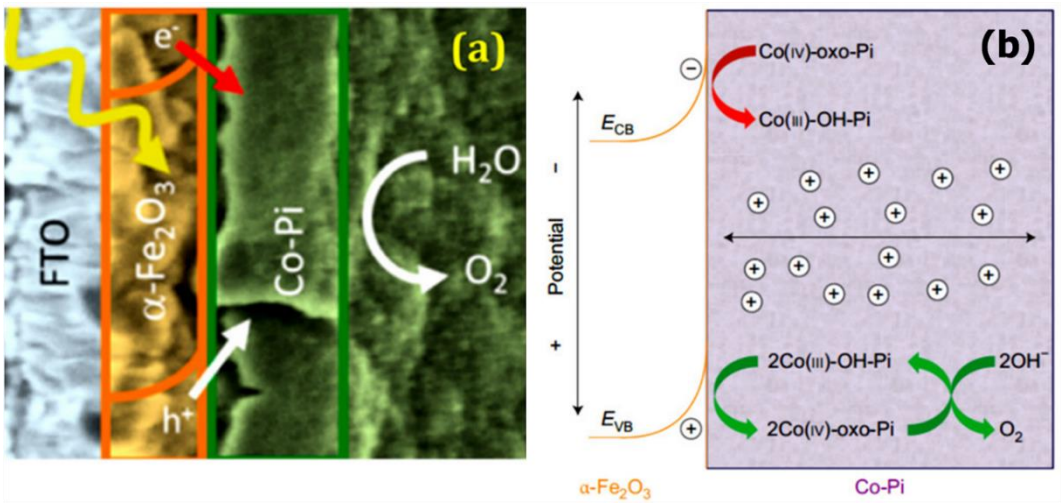

Figure 1.4. a) α-Fe_2O_3 films prepared by ALD with Co-Pi coating. b) Scheme of hole movement from α-Fe_2O_3 to Co-Pi under PEC water-oxidation conditions.[73]

Several other metal compounds have also been used as effective oxygen evolution co-catalysts over the α-Fe_2O_3 photoanodes. For instance, Hong et al. electrodeposited Ni-Bi thin layers on the α-Fe_2O_3 photoanode, which lowered the onset potential by ~200 mV and achieved a 9.5-fold enhancement in the photocurrent density at 0.86 V vs. RHE. However, owing to the kinetic limitation of Ni-Bi, the photocurrent density could be only enhanced at low overpotentials and a gradual decrease of the photocurrent density could be observed at higher overpotentials.[75] Another Ni-based co-catalyst of ultrathin amorphous NiOOH was photoelectrodeposited on α-Fe_2O_3 as an electrocatalyst, which could reduce the charge recombination at the interface of electrode/electrolyte and result in a huge enhancement on the PEC performance.[76] Likewise, Yu et al. photoelectrodeposited FeOOH on the α-Fe_2O_3 as co-catalysts, resulting in a 140 mV cathodic shift of the onset potential and a great enhanced photocurrent density. The improved activity was mainly attributed to the catalytic activity of FeOOH, which accelerated the kinetics for water oxidation and increased the amount of photogenerated holes for the reaction.[77] In addition, the researchers also tried to develop the co-catalysts with multiple metal sites, which tended to possess superior activity due to the synergetic effects caused by the interaction between different metal sites. Hu et al. designed a $FeNiO_x$ co-catalyst by a photoelectrochemical method with loadings of merely several micrograms per square centimeter. The low loading and high activity of the co-catalyst resulted in significantly deceased onset potential for PEC water oxidation.[78] Similarly, a hybrid co-catalyst of $CoFeO_x$ with lower light absorption, higher charge separation and better stability was reported to accelerate the water oxidation kinetics of α-Fe_2O_3. This

work pointed out the elegant design of the catalytic material could generate synergetic effects on improving PEC performance.[79]

1.3.5 Interface modulation between α-Fe_2O_3 and co-catalysts

The above discuss clearly demonstrates that robust co-catalysts are significantly important to promote the surface reaction by providing sufficient reaction sites and reducing the surface recombination. Once the co-catalysts were loaded on the semiconductors, a distinct interface could be formed between these two components. In order to match the fast reaction kinetics of the co-catalysts, sufficient photogenerated charge carriers must be extracted from the bulk of the semiconductors to the co-catalysts. Therefore, the co-catalyst/semiconductor interface is extremely crucial for the separation and migration of photogenerated charge carriers between two components.[80] Poor charge transder at the interface may lead to the accumulation and recombination of the carriers, thus leading to the poor efficiency of the PEC water splitting. Even though with the introduction of co-catalysts, the PEC water oxidation efficiency still remains challenging to reach the required level due to the ineffective charge transfer through the interface of semiconductor and co-catalyst, which may be resulted from the mismatch of crystal lattice or energy band level between the semiconductor and co-catalyst.[81] Therefore, much attention should be paid to the engineering of the co-catalyst/semiconductor interface.

There are two kinds of strategies for fabricating efficient co-catalyst/semiconductor interface to facilitate the charge transfer. The first one is introducing a carefully selected mediator between the semiconductor and co-catalyst to modulate the interfacial charge transfer. Those mediators locating at interfaces mainly play two roles for the whole PEC processes: (1) reduce the interfacial defects density; (2) enhance the transport of charge carriers from semiconductors to co-catalysts through strengthening the interfacial communication. The co-catalysts can perform admirable when the semiconductor and the mediators are exactly adaptive with the co-catalysts on the surface. Thus, the semiconductors, mediators and the co-catalysts should match well and work cooperatively from different aspects. The second approach is constructing interfacial interaction between semiconductors and co-catalysts. The interaction between two different components can be divided into the physical adsorption and chemical coupling.[82] The physical adsorption, such as the Van-der-Waals force, usually leads to a weak interaction; while the chemical coupling results in a much stronger interaction and

a modulated electronic structure.[83] Therefore, construction of chemical coupling between semiconductor and co-catalyst is highly desirable to improve the catalytic activity with a strong and compact interfacial interaction.[84] The following discussion will mainly focus on different mediators to optimize the charge transfer at the interfaces between semiconductors and co-catalysts, such as hole-storage layers, passivation layers and metal layers.

1.3.5.1 Different mediators to modulate the interfacial charge transfer

Due to the interfacial resistance between the co-catalysts and the semiconductor, an injection barrier would be existed at the semiconductor/co-catalyst interface, leading to the moderate hole transfer efficiency to the surface. If the holes could be exacted from the bulk of the semiconductor and stored temporarily in a mediator, then it would be much easier for them to transfer to the surface co-catalyst for water oxidation. Inspired by this motivation, introducing an hole-storage layer (HSL) between the semiconductor and the co-catalysts would be effective to promote the charge separation/transfer and thus enhance the activity of the photoanodes.[85] Recently, a layer of ferrihydrite (Fh) was introduced as a hole transfer channel between Ti-α-Fe_2O_3 and CoPi for efficient charge transfer. The tri-phase structure of CoPi/Fh/Ti-α-Fe_2O_3 exhibited a remarkable photocurrent density of 3.0 mA cm^{-2} at 1.23 V vs. RHE. Electrochemical measurements revealed that the Fh layer could improve the holes migration from Ti-α-Fe_2O_3 to the active sites of Co-Pi and facilitate the hole injection into the electrolyte. Therefore, as shown in Figure 1.5a and 1.5b, the introduction of Fh layers is beneficial for the holes transfer to Co-Pi co-catalysts, resulting in the dramatically enhanced PEC performance.[86] Similar phenomenon could be observed on $Ni(OH)_2$. As reported by Wang and co-workers, The conjugated co-catalysts of $Ni(OH)_2/IrO_2$ on the electrode could accelerate the reaction and decrease the onset potential by ~200 mV (Figure 1.5d). As displayed in Figure 1.5c, as a HSL, the $Ni(OH)_2$ can extract and store the holes generated from α-Fe_2O_3 and thus promote the charge transfer between α-Fe_2O_3 and IrO_2. Then the stored holes in $Ni(OH)_2$ can be utilized by IrO_2 more facilely, leading to the efficient water oxidation.[81]

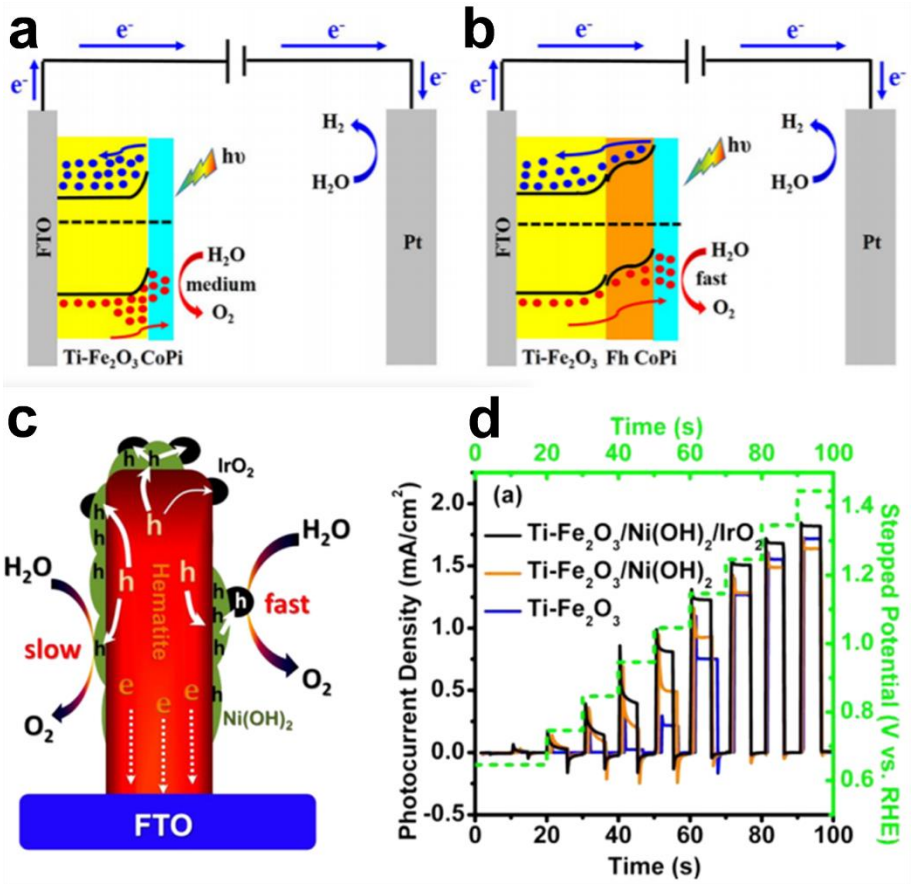

Figure 1.5. Charge transfer processes for a) Co-Pi/Ti-Fe_2O_3 and b) Co-Pi/Fh/Ti-Fe_2O_3 under illumination.[86] c) Scheme of the charge transfer from α-Fe_2O_3 to water through $Ni(OH)_2$ and/or IrO_2. d) Chronoamperometry measurement of Ti-Fe_2O_3, Ti-Fe_2O_3/$Ni(OH)_2$, and Ti-Fe_2O_3/$Ni(OH)_2$/IrO_2 under a stepped potential.[81]

As mention in Section 1.3.4.1, the utilization of passivation layers could facilitate the hole injection at the semiconductor/electrolyte interface by passivating the surface states. However, most of the passivation layers are unstable in alkaline solution or poorly contacted with the semiconductors, leading to the poor stability of the photoanodes in harsh condition for water oxidation. Then the combination of passivation layers and co-catalysts on the α-Fe_2O_3 photoanode could achieve an effect of two birds with one stone: the passivation layers would be protected by the outermost co-catalyst, while the charge transfer at the semiconductor/co-catalyst interface would be optimized by the passivation layers. Ahn et al. fabricated an efficient α-Fe_2O_3-based photoanode with the Ti-SiO_x passivation layer and a Co-Pi co-catalyst. Owing to the outstanding properties for hole extraction and proper conductivity, the passivation layer of Ti-SiO_x could reduce recombination by passivating the surface states of Ti-Fe_2O_3. As shown in Figure 1.6, with the passivation effect of Ti-SiO_x for the surface states, the activity of Co-Pi dramatically

increased. These results demonstrated that the optimized photoanode of Co-Pi/Ti-SiO_x/α-Fe_2O_3 could fully utilize the synergetic effect of the surface passivation layer, hole extraction property and co-catalyst for efficient PEC water oxidation.[87]

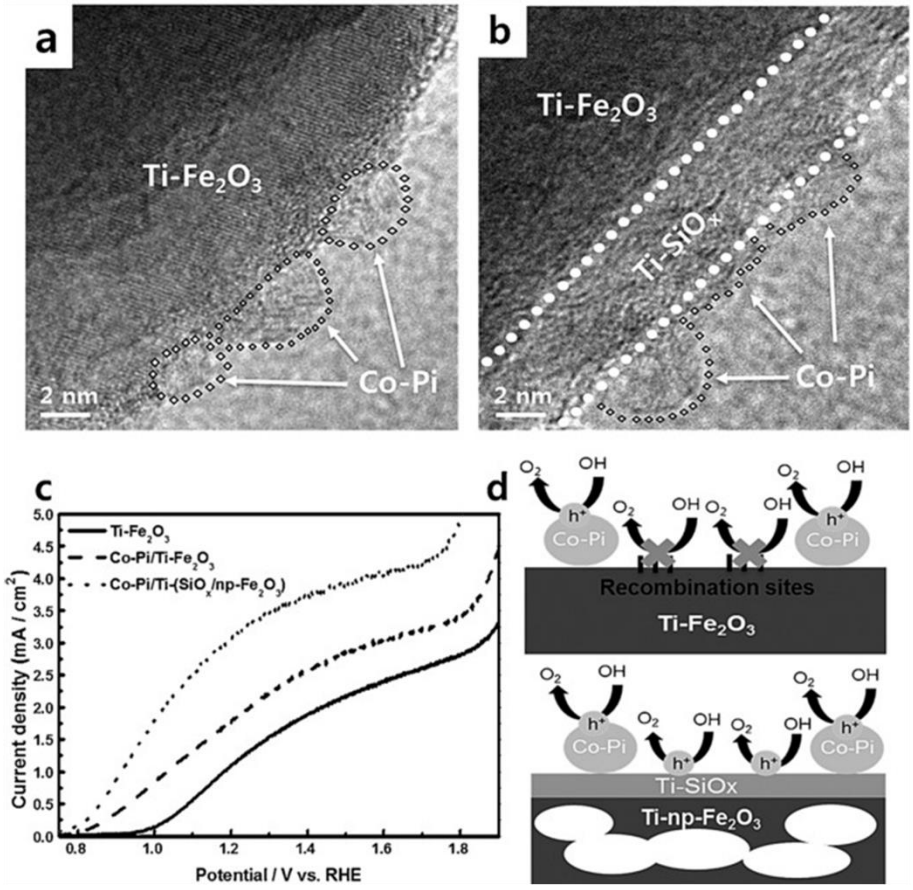

Figure 1.6. a) TEM image of the Co-Pi/Ti-Fe_2O_3, and b) Co-Pi/Ti-(SiO_x/np-Fe_2O_3). c) *J-V* curves of Ti-Fe_2O_3, Co-Pi/Ti-Fe_2O_3, and Co-Pi/Ti-(SiO_x/np-Fe_2O_3) under AM 1.5 G illumination in 1 M NaOH solution. d) The reaction mechanism of Co-Pi/Ti-Fe_2O_3 and Co-Pi/Ti-(SiO_x/np-Fe_2O_3).[87]

It was reported that the work function induced by the Fermi Level difference between metals and semiconductors can be effective to facilitate the charge transfer from metals to semiconductors, sometimes even faster than the lifetime of the photoexcited electrons.[88-89] Furthermore, the charge carrier conductivity of the metal is significantly better than the semiconductor and the co-catalyst, which then could provide an extra charge transfer channel for the photoanodes. For instance, Li and co-workers fabricated a core-shell Co/CoO_x modified Ti/α-Fe_2O_3 electrode. Due to the catalytic effect of CoO_x, the photogenerated holes could be collected and stored from the hematite electrode. However, it is difficult for the holes to transfer to the surface of the electrode due to the interfacial resistance between Ti/α-Fe_2O_3 and CoO_x. Meanwhile, the metallic Co could

provide a rapid charge transfer channel for the photogenerated holes and arrive at the surface of the photoanode readily, resulting in lower onset potentials and enhanced activity for water oxidation (Figure 1.7).[90]

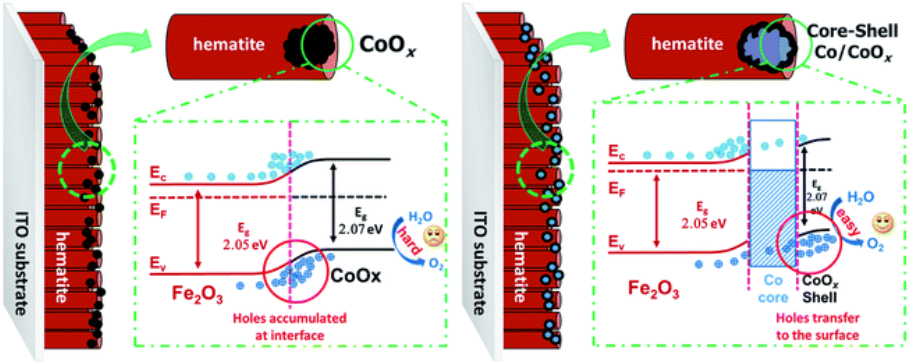

Figure 1.7. The charge separation and transfer process of CoO_x and core-shell Co/CoO_x-modified Ti/α-Fe_2O_3 under visible light illumination.[90]

As revealed by the excellent examples mentioned above, besides the structure/property of α-Fe_2O_3 and co-catalysts, the fabrication of a high-quality heterostructured interface is significant for the fast charge transfer across junctions and thus for achieving a remarkable PEC activity. Additionally, the interface engineering between the co-catalysts and the α-Fe_2O_3 is significantly important for the charge transfer from the α-Fe_2O_3 to the co-catalysts. Decorating hole transfer mediators at the semiconductor/co-catalyst interface can greatly enhance charge transfer efficiency. Therefore, a suitable mediator is significantly important to construct an efficient charge modulation system for PEC water oxidation.

1.3.5.2 Carbon-based co-catalysts for PEC water oxidation

Ideally, the co-catalysts should be low-cost, abundant, and efficient. In this regard, carbon-based materials provide a great opportunity for constructing cost-effective co-catalysts. Metal-free carbon-based materials, a promising alternative to those transition metal-based materials mentioned in Section 1.3.4.2, feature high electrical conductivity, surface functionality, excellent stability, and diverse morphologies. Particularly, it's feasible to optimize the property/activity of the carbon materials due to their editable structure. Recently, carbon-based materials without metal have attracted great interest to modify the α-Fe_2O_3 with improved activity for PEC water oxidation. Li and co-workers decorated the reduced graphene QDs (rGQDs) on α-Fe_2O_3 photoanode as surface passivation layers. The self-assembly fabrication process of loading the rGQDs

passivation layer was quite effective and resulted in a 8-fold increase in photocurrent density for rGQD/α-Fe_2O_3 photoanode.[91] Chen et al. demonstrated a one-step hydrothermal synthesis to fabricate CQDs/α-Fe_2O_3 heterojunction photoanode, which exhibited an enhanced photocurrent density and a cathodic shift of 300 mV in onset potential.[92] More recently, Yang et al. found that the α-Fe_2O_3 photoanode with poor conductivity and defective surface could be activated by graphene decoration through facilitated charge transfer. Electrochemical measurements signified that the surface recombination and surface charge carrier density can be optimized by the graphene overlayers, thus accelerating the water oxidation kinetics.[93]

Although those carbon materials, serving as surface modifier over α-Fe_2O_3, can exhibit good PEC performance regardless of possible doping contribution, rational functionalization and synthesis of carbon-based co-catalysts provide a great opportunity for further enhancing their intrinsic activity towards water oxidation. Recently, single-atom catalysts (SACs), with isolated metal sites supported on solid substrates, are emerging as a highly attractive class of catalysts because they integrate the merits of homogeneous and heterogeneous catalysis, such as high activity, selectivity, stability, and maximization of atom utilization efficiency. Notably, the atomization of metal sites on substrates usually possesses unsaturated coordination environment and large surface free energy compared with the subnano, nano, bulk ones. As such, those isolated sites is much active for chemical reactants (Figure 1.8a).[94]

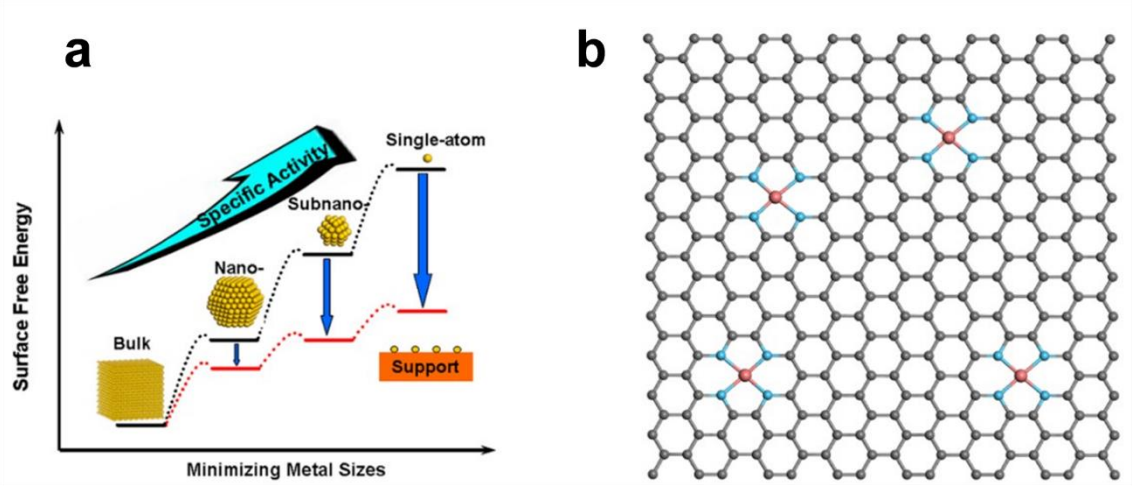

Figure 1.8. a) Schematic illustration of the changes of surface free energy and specific activity per metal atom with particle size and the support effects on stabilizing single atoms. b) Schematic molecular configurations of single atom incorporated graphene. Grey, blue, and red balls refer to carbon, nitrogen, and metal atom, respectively. [94]

Among various single-atom catalysts, single-atom incorporated N-rich carbon (M-NC, M typically refers to cost-effective transition metals, such as Fe, Co, Ni; the typical structure illustration is presented in Figure 1.8b) is particularly investigated.[95] It has attracted extensive attention in various fields, especially in electrocatalysis field, due to its low cost, editable metal center and coordination, unique electronic properties and unexpected performance.[96] However, the application of SACs supported on carbon-based materials in OER has been rarely reported compared with the HER and ORR. Recently, Fei et al. prepared a series of monodispersed atomic transition metals embedded N-doped graphene with a common and unambiguous MN_4C_4 (M refers to Fe, Co, Ni) moiety.[97] As shown in Figure 1.9, both the density functional theoretical (DFT) and electrochemical measurements confirmed that those anchored MN_4C_4 sites on carbon substrate could efficiently catalyze oxygen evolution with activities trend of Ni > Co > Fe. Specifically, the Ni–NC catalyst showed an onset potential of 1.43 V (at 0.5 mA cm^{-2}) and its overpotential at 10 mA cm^{-2} is 331 mV, much smaller than those of Co–NC (402 mV) and Fe–NC (488 mV). This advanced example could motive rational design and synthesis of single atom co-catalysts for improving PEC water oxidation performance. Double-atoms of metal have also been applied into the NC as the efficient catalyst. For example, Hu et al. found that Co species atomically dispersed on N-doped carbon (Co-N-C) could be activated by electrochemical activation in Fe-containing alkaline electrolyte. The Fe species could be incorporated into Co-N-C (forming a Co-Fe di-atom catalyst (Co-Fe-N-C)), which can critically enhance the activity for water oxidation compared to Co-N-C. It could be probed from The operando XAS probe the formation processes of the bonding with double atom motif.[98]

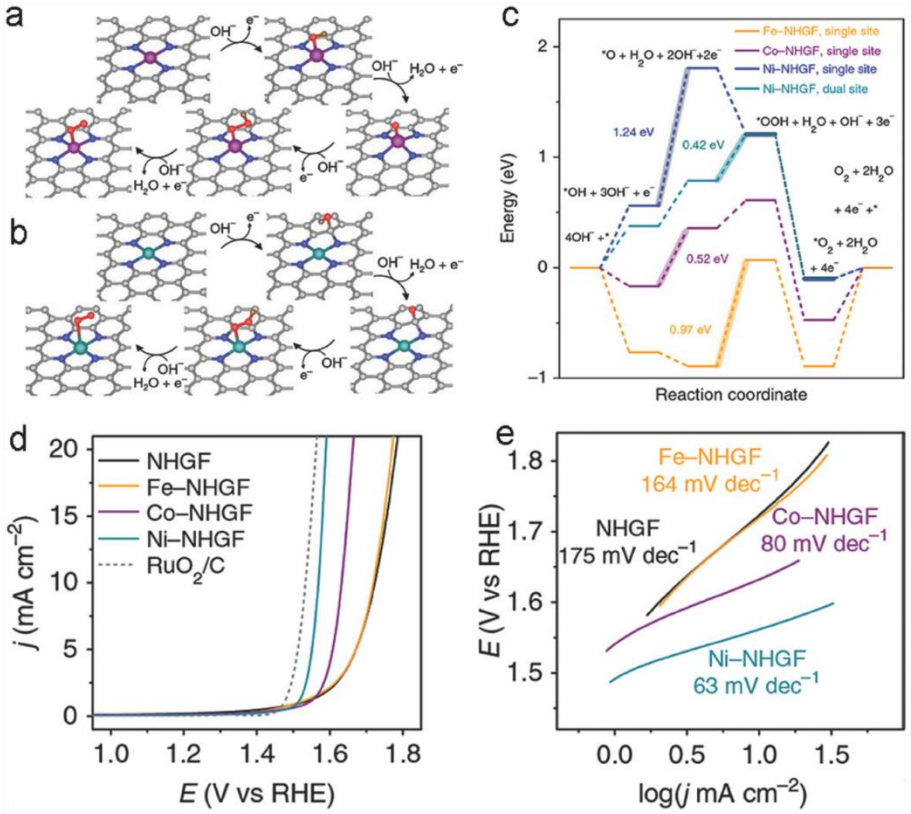

Figure 1.9. a, b) Proposed mechanism of MN_4C_4 with the intermediates adsorbed on the single site (M = Fe or Co) and dual site (M = Ni). c) Free energy diagram at 1.23 V vs. RHE for OER at M-NG with MN_4C_4 moieties. d) OER activity evaluated by LSV (with iR correction) in 1 M KOH at the potential scan rate of 5 mV s^{-1} for M-NG, NG, and commercial RuO_2/C. e) Corresponding Tafel plots of the catalysts.[97]

The superior electrochemical O_2 evolution activity related to the isolated metal sites highlights the great potential of M-NC employed as co-catalysts towards PEC water oxidation. However, such kind of material have rarely been used as co-catalysts in the photocatalytic system, especially for achieving outstanding performance in photoelectrocatalysis. In this regard, it's highly desirable to develop robust single atom incorporated NC with well-defined atomic coordination as efficient co-catalysts for the cost-effective PEC system.

1.3.5.3 Interfacial engineering between α-Fe_2O_3 and carbon-based co-catalysts

As mentioned in Section 1.3.5.2, the researchers mainly emphasized the effect of carbon materials as passivation layers and/or conductive scaffolds to suppress the surface recombination and facilitate the charge transfer. However, the lack of active sites on the carbon layers lead to a restricted activity, suggesting the great potential to enhance the

performance by implanting active sites into the carbon framework. For instance, Hou et al. developed a novel Co-N_x/P complex-doped carbon electrode as an advanced electrocatalyst for water oxidation reaction. The coordination of Co-N_x active centers hybridized with that of neighboring P atoms enhanced the electron transfer and optimized the charge distribution of the carbon surface, which synergistically promoted reaction kinetics by providing more exposed active sites. Then this Co-N_x/P carbon was integrated with α-Fe_2O_3 electrode as the co-catalyst, achieving highly efficient solar-driven water splitting.[99] However, it worth stressing that this integrated photoanode is obtained via direct deposition at room temperature without special treatment. In such hybrid photoanode, the interfacial coupling is usually weak, although limited charge transport phenomenon can be observed. Thus, suitable treatments before or after the formation of heterostructure are necessary and hold great potential to strengthen the interfacial coupling for rapid charge transfer across the junctions. For example, Co-doped carbon layer was prepared to decorated on hematite by a hydrothermal method, which produced a good contact between carbon layer and hematite. The improved performance can be attributed to the enhanced conductivity, the suppressed electron-hole recombination by the carbon layer and the accelerated OER kinetics by the embedded Co species.[100] However, the quantity of the metal in this Co-doped carbon layer was not precisely controlled, leading to a low atom utilization. Furthermore, the charge transfer behavior at the interface between the carbon layer and the α-Fe_2O_3 was not mentioned, resulting in an unclear fundamental mechanism. As mentioned in Section 1.3.5, strengthening the interface coupling is crucial to boost the charge carriers transfer across the junctions towards improving the photoelectrocatalytic efficiency. So how to combine the M-NC co-catalyst with the α-Fe_2O_3 properly is significantly important for the efficient charge transfer between these two components.

1.4 Thesis motivations and organization

PEC water splitting has been projected as a promising approach to meet the steadily growing demand for cleaner and renewable energy. On the basis of the above-mentioned overview, it can be concluded that three main components of the PEC system, including the semiconductors, co-catalysts, and interfaces between them, are crucial for the apparent photoelectrocatalytic efficiency. In this concern, in order to construct a robust system for efficient water oxidation, the above three factors should be particularly considered: (1) hematite (α-Fe_2O_3) was chosen as a prototype owing to its low cost,

suitable band structure and high chemical stability in alkaline environment; (2) novel co-catalysts should be designed to achieve comprehensive enhancement for PEC water splitting; (3) charge modulation should be optimized at the semiconductor/co-catalyst interface, which can boost the separation of photogenerated charge by injecting the charge carriers into the co-catalyst.

In this dissertation, two criteria of the hematite-based photoanodes are considered to enhance the catalytic activity, including novel co-catalyst decoration to reduce the overpotential for water oxidation and relevant interface modulation to facilitate the charge transfer between the α-Fe_2O_3 and co-catalyst. First, an ultrathin cobalt-manganese nanosheet is designed by modulating the metal site to achieve the superior OER activity. Then, two strategies, i.e., inserting hole transfer mediators and constructing direct chemical interaction at the interface between α-Fe_2O_3 and co-catalysts, are proposed to optimize the charge transfer within the photoanodes for boosting the PEC water oxidation.

This dissertation is divided into five chapters. A summary of the remaining four chapters is described as below:

Chapter 2 Ultrathin cobalt-manganese nanosheets: an efficient platform for enhanced photoelectrochemical water oxidation with electron-donating effect

As a water-oxidizing photoanode, the performance of α-Fe_2O_3 has been crucially limited by poor optoelectronic properties and sluggish reaction kinetics, which lead to severe surface charge recombination and high overpotential for photo-assisted water oxidation. Notably, loading oxygen evolution co-catalysts has been regarded as a particularly effective approach to enhance the surface reaction kinetics of α-Fe_2O_3. Meanwhile, the electrocatalysts with multiple metal sites have been reported to possess superior activity due to the synergetic effects caused by the interaction between different metal sites. Therefore, it is believed that bimetallic compounds, which are adjustable with different metal sites, are promising co-catalysts for PEC water oxidation owing to their abundant active sites and versatility in composition. In this chapter, ultrathin cobalt-manganese (Co-Mn) nanosheets, consisting of amorphous $Co(OH)_x$ layers and ultrasmall Mn_3O_4 nanocrystals, were designed as co-catalysts on α-Fe_2O_3 for PEC water oxidation. It was believed that incorporation of Mn sites in the nanosheets could create electron donation to Co sites and facilitate the activation of OH group, which then might drastically increase the catalytic activities for OER. Therefore, the Co-Mn nanosheets were expected to enhance water oxidation performance of α-Fe_2O_3 by facilitating surface

hole transport and promoting charge separation efficiency along with passivating the surface states.

Chapter 3 A universal strategy boosting photoelectrochemical water oxidation by utilizing MXene nanosheets as hole transfer mediators

Even though with the introduction of co-catalysts, the PEC water oxidation efficiency still remains challenging to reach the required level due to the inefficient charge transfer through the interface of semiconductor and co-catalyst, which may be resulted from the mismatch of structural properties and energy levels between the semiconductor and co-catalyst. This limitation signifies that interfacial charge modulation should be implemented to boost the charge separation on the photoanodes. In this chapter, we aim to construct a novel interfacial charge modulation system by integrating ultrathin MXene nanosheets (MNs) as hole transfer mediators between α-Fe_2O_3 nanorods and conventional co-catalyst layers. Due to the different working potentials between metallic MNs and α-Fe_2O_3, a MNs/α-Fe_2O_3 Schottky junction can be formed with an interfacial built-in electric field, resulting in a reduced recombination during the charge separation and transfer process. After decorating with the co-catalyst layers, photogenerated holes were expected to be driven from the α-Fe_2O_3 to the reaction sites on the co-catalysts, resulting in enhanced PEC performance for water oxidation.

Chapter 4 Constructing chemical interaction between hematite and carbon nanosheets with single active sites for efficient photoelectrochemical water oxidation

In order to fabricate efficient co-catalyst/semiconductor interface for facilitating the charge transfer, another approach is constructing direct interfacial interaction between semiconductors and co-catalysts, which is highly desirable to improve the catalytic activity. Considering the high atom utilization efficiency and extraordinary catalytic properties, single-atom catalysts exhibit huge potentials to be efficient co-catalysts for PEC water oxidation. How to compactly integrate the single-atom catalysts with the α-Fe_2O_3 still remains challenging. In this chapter, atomically dispersed nickel embedded ultrathin nitrogen-rich carbon (Ni-NC) was fabricated and subsequently anchored on α-Fe_2O_3 with optimized annealing treatment. Due to the intrinsic defects on the α-Fe_2O_3 and abundant oxygen-containing groups in the Ni-NC, direct chemical interaction can be easily constructed between α-Fe_2O_3 and Ni-NC. The newly formed chemical bonds at the interface of α-Fe_2O_3 and Ni-NC were expected to act as interfacial charge shuttle channels to mediate the hole transfer. In addition, atomically dispersed Ni sites with identical Ni-

N_4 moiety on the carbon nanosheets could provide abundant active sites for favorable PEC water oxidation upon accepting the massive photogenerated holes through the interfacial chemical bonding. By combining the direct chemical interaction between α-Fe_2O_3 and Ni-NC and robust single Ni sites for OER, the designed heterostructure system may exhibit highly efficient PEC water oxidation.

Chapter 5 General conclusions and future prospects

This chapter presents an overall summary and conclusion of this dissertation and gives the prospects for future work.

References

[1] T. Faunce, S. Styring, M. R. Wasielewski, G. W. Brudvig, A. W. Rutherford, J. Messinger, A. F. Lee, C. L. Hill, H. Degroot, M. Fontecave, *Energy Environ. Sci.* **2013**, 6, 1074.

[2] I. Roger, M. A. Shipman, M. D. Symes, *Nat. Rev. Chem.* **2017**, 1, 1.

[3] N. S. Lewis, *Science* **2016**, 351.

[4] M. G. Walter, E. L. Warren, J. R. McKone, S. W. Boettcher, Q. Mi, E. A. Santori, N. S. Lewis, *Chem. Rev.* **2010**, 110, 6446.

[5] B. A. Pinaud, J. D. Benck, L. C. Seitz, A. J. Forman, Z. Chen, T. G. Deutsch, B. D. James, K. N. Baum, G. N. Baum, S. Ardo, *Energy Environ. Sci.* **2013**, 6, 1983.

[6] J. A. Turner, *Science* **1999**, 285, 687.

[7] J. H. Kim, D. Hansora, P. Sharma, J.-W. Jang, J. S. Lee, *Chem. Soc. Rev.* **2019**, 48, 1908.

[8] G. Wang, Y. Ling, H. Wang, L. Xihong, Y. Li, *J. Photochem. Photobiol. C* **2014**, 19, 35.

[9] J. H. Kim, J. S. Lee, *Adv. Mater.* **2019**, 31, 1806938.

[10] X. T. Xu, L. Pan, X. Zhang, L. Wang, J. J. Zou, *Adv. Science* **2019**, 6, 1801505.

[11] A. Fujishima, K. Honda, *Nature* **1972**, 238, 37.

[12] X. Yang, A. Wolcott, G. Wang, A. Sobo, R. C. Fitzmorris, F. Qian, J. Z. Zhang, Y. Li, *Nano Lett.* **2009**, 9, 2331.

[13] A. Dabirian, R. Van De Krol, *Chem. Mater.* **2015**, 27, 708.

[14] W. Li, P. Da, Y. Zhang, Y. Wang, X. Lin, X. Gong, G. Zheng, *ACS Nano* **2014**, 8, 11770.

[15] K. Sivula, F. Le Formal, M. Grätzel, *ChemSusChem* **2011**, 4, 432.

[16] A. Murphy, P. Barnes, L. Randeniya, I. Plumb, I. Grey, M. Horne, J. Glasscock, *Int. J. Hydrog. Energy* **2006**, 31, 1999.

[17] M. J. Katz, S. C. Riha, N. C. Jeong, A. B. Martinson, O. K. Farha, J. T. Hupp, *Coord. Chem. Rev.* **2012**, 256, 2521.

[18] J. H. Kennedy, K. W. Frese Jr, *J. Electrochem. Soc.* **1978**, 125, 709.

[19] Y. Lin, G. Yuan, R. Liu, S. Zhou, S. W. Sheehan, D. Wang, *Chem. Phys. Lett.* **2011**, 507, 209.

[20] D. A. Wheeler, G. Wang, Y. Ling, Y. Li, J. Z. Zhang, *Energy Environ. Sci.* **2012**, 5, 6682.

[21] S. Shen, *J. Mater. Res.* **2014**, 29, 29.

[22] Y. Ling, Y. Li, *Part. Part. Syst. Charact.* **2014**, 31, 1113.

[23] B. Iandolo, B. Wickman, I. Zorić, A. Hellman, *J. Mater. Chem. A* **2015**, 3, 16896.

[24] K. Itoh, J. M. Bockris, *J. Electrochem. Soc.* **1984**, 131, 1266.

[25] B. D. Alexander, P. J. Kulesza, I. Rutkowska, R. Solarska, J. Augustynski, *J. Mater. Chem.* **2008**, 18, 2298.

[26] I. Cesar, A. Kay, J. A. Gonzalez Martinez, M. Grätzel, *J. Am. Chem. Soc.* **2006**, 128, 4582.

[27] A. Kay, I. Cesar, M. Grätzel, *J. Am. Chem. Soc.* **2006**, 128, 15714.

[28] G. Wang, Y. Ling, D. A. Wheeler, K. E. George, K. Horsley, C. Heske, J. Z. Zhang, Y. Li, *Nano Lett.* **2011**, 11, 3503.

[29] T. Vincent, M. Gross, H. Dotan, A. Rothschild, *Int. J. Hydrog. Energy* **2012**, 37, 8102.

[30] L. Li, Y. Yu, F. Meng, Y. Tan, R. J. Hamers, S. Jin, *Nano Lett.* **2012**, 12, 724.

[31] N. Beermann, L. Vayssieres, S. E. Lindquist, A. Hagfeldt, *J. Electrochem. Soc.* **2000**, 147, 2456.

[32] S. U. Khan, T. Sultana, *Sol. Energy Mater. Sol. Cells* **2003**, 76, 211.

[33] P. S. Bassi, L. H. Wong, J. Barber, *Phys. Chem. Chem. Phys.* **2014**, 16, 11834.

[34] A. G. Tamirat, J. Rick, A. A. Dubale, W.-N. Su, B.-J. Hwang, *Nanoscale Horiz.* **2016**, 1, 243.

[35] A. Pu, J. Deng, M. Li, J. Gao, H. Zhang, Y. Hao, J. Zhong, X. Sun, *J. Mater. Chem. A* **2014**, 2, 2491.

[36] O. Zandi, B. M. Klahr, T. W. Hamann, *Energy Environ. Sci.* **2013**, 6, 634.

[37] Y. Ling, G. Wang, D. A. Wheeler, J. Z. Zhang, Y. Li, *Nano Lett.* **2011**, 11, 2119.

[38] P. Liao, E. A. Carter, *J. Appl. Phys.* **2012**, 112, 013701.

[39] Y. Lin, Y. Xu, M. T. Mayer, Z. I. Simpson, G. McMahon, S. Zhou, D. Wang, *J. Am. Chem. Soc.* **2012**, 134, 5508.

[40] M. Zhang, W. Luo, Z. Li, T. Yu, Z. Zou, *Appl. Phys. Lett.* **2010**, 97, 042105.

[41] Y. Ling, G. Wang, J. Reddy, C. Wang, J. Z. Zhang, Y. Li, *Angew. Chem. Int. Ed.* **2012**, 124, 4150.

[42] M. T. Mayer, Y. Lin, G. Yuan, D. Wang, *Accounts Chem. Res.* **2013**, 46, 1558.

[43] A. Memar, W. R. W. Daud, S. Hosseini, E. Eftekhari, L. J. Minggu, *Sol. Energy* **2010**, 84, 1538.

[44] K. Sivula, F. L. Formal, M. Gratzel, *Chem. Mater.* **2009**, 21, 2862.

[45] C. A. Bignozzi, S. Caramori, V. Cristino, R. Argazzi, L. Meda, A. Tacca, *Chem. Soc. Rev.* **2013**, 42, 2228.

[46] Y.-K. Hsu, Y.-C. Chen, Y.-G. Lin, *ACS Appl. Mater. Interfaces* **2015**, 7, 14157.

[47] M. T. Mayer, C. Du, D. Wang, *J. Am. Chem. Soc.* **2012**, 134, 12406.

[48] J. Li, F. Meng, S. Suri, W. Ding, F. Huang, N. Wu, *Chem. Commun.* **2012**, 48, 8213.

[49] J. Zhang, S. Eslava, *Sustain. Energy Fuels* **2019**, 3, 1351.

[50] P. Tang, J. Arbiol, *Nanoscale Horiz.* **2019**, 4, 1256.

[51] K. U. Wijayantha, S. Saremi-Yarahmadi, L. M. Peter, *Phys. Chem. Chem. Phys.* **2011**, 13, 5264.

[52] D. K. Bora, A. Braun, E. C. Constable, *Energy Environ. Sci.* **2013**, 6, 407.

[53] L. Xi, P. S. Bassi, S. Y. Chiam, W. F. Mak, P. D. Tran, J. Barber, J. S. C. Loo, L. H. Wong, *Nanoscale* **2012**, 4, 4430.

[54] X. Yang, R. Liu, C. Du, P. Dai, Z. Zheng, D. Wang, *ACS Appl. Mater. Interfaces* **2014**, 6, 12005.

[55] M. Barroso, C. A. Mesa, S. R. Pendlebury, A. J. Cowan, T. Hisatomi, K. Sivula, M. Grätzel, D. R. Klug, J. R. Durrant, *Proc. Natl. Acad. Sci.* **2012**, 109, 15640.

[56] F. Le Formal, N. Tetreault, M. Cornuz, T. Moehl, M. Grätzel, K. Sivula, *Chem. Sci.* **2011**, 2, 737.

[57] K. Sivula, J. Phys. Chem. Lett. **2013**, 4, 1624.

[58] Y. Kuang, T. Yamada, K. Domen, *Joule* **2017**, 1, 290.

[59] M. W. Kanan, Y. Surendranath, D. G. Nocera, *Chem. Soc. Rev.* **2009**, 38, 109.

[60] J. Ran, J. Zhang, J. Yu, M. Jaroniec, S. Z. Qiao, *Chem. Soc. Rev.* **2014**, 43, 7787.

[61] J. Sato, N. Saito, Y. Yamada, K. Maeda, T. Takata, J. N. Kondo, M. Hara, H. Kobayashi, K. Domen, Y. Inoue, *J. Am. Chem. Soc.* **2005**, 127, 4150.

[62] B. Ma, J. Yang, H. Han, J. Wang, X. Zhang, C. Li, *J. Phys. Chem. C* **2010**, 114, 12818.

[63] S. D. Tilley, M. Cornuz, K. Sivula, M. Grätzel, *Angew. Chem. Int. Ed.* **2010**, 49, 6405.

[64] W. Li, S. W. Sheehan, D. He, Y. He, X. Yao, R. L. Grimm, G. W. Brudvig, D. Wang, *Angew. Chem. Int. Ed.* **2015**, 127, 11590.

[65] S. Majumder, S. Khan, *Int. J. Hydrog. Energy* **1994**, 19, 881.

[66] K. Fan, F. Li, L. Wang, Q. Daniel, H. Chen, E. Gabrielsson, J. Sun, L. Sun, *ChemSusChem* **2015**, 8, 3242.

[67] J. Ran, J. Zhang, J. Yu, M. Jaroniec, S. Z. Qiao, *Chem. Soc. Rev.* **2014**, 43, 7787.

[68] M. W. Kanan, D. G. Nocera, *Science* **2008**, 321, 1072.

[69] E. M. Steinmiller, K.-S. Choi, *Proc. Natl. Acad. Sci.* **2009**, 106, 20633.

[70] D. K. Zhong, S. Choi, D. R. Gamelin, *J. Am. Chem. Soc.* **2011**, 133, 18370.

[71] J. J. Pijpers, M. T. Winkler, Y. Surendranath, T. Buonassisi, D. G. Nocera, *Proc. Natl. Acad. Sci.* **2011**, 108, 10056.

[72] D. K. Zhong, M. Cornuz, K. Sivula, M. Grätzel, D. R. Gamelin, *Energy Environ. Sci.* **2011**, 4, 1759.

[73] B. Klahr, S. Gimenez, F. Fabregat-Santiago, J. Bisquert, T. W. Hamann, *J. Am. Chem. Soc.* **2012**, 134, 16693.

[74] D. R. Gamelin, *Nat. Chem.* **2012**, 4, 965.

[75] Y.-R. Hong, Z. Liu, S. F. B. Al-Bukhari, C. J. J. Lee, D. L. Yung, D. Chi, T. A. Hor, *Chem. Commun.* **2011**, 47, 10653.

[76] F. Malara, A. Minguzzi, M. Marelli, S. Morandi, R. Psaro, V. Dal Santo, A. Naldoni, *ACS Catal.* **2015**, 5, 5292.

[77] Q. Yu, X. Meng, T. Wang, P. Li, J. Ye, *Adv. Func. Mater.* **2015**, 25, 2686.

[78] C. G. Morales-Guio, M. T. Mayer, A. Yella, S. D. Tilley, M. Grätzel, X. Hu, *J. Am. Chem. Soc.* **2015**, 137, 9927.

[79] Y. F. Xu, X. D. Wang, H. Y. Chen, D. B. Kuang, C. Y. Su, *Adv. Func. Mater.* **2016**, 26, 4414.

[80] C. Ding, J. Shi, Z. Wang, C. Li, *ACS Catal.* **2017**, 7, 675.

[81] Z. Wang, G. Liu, C. Ding, Z. Chen, F. Zhang, J. Shi, C. Li, *J. Phys. Chem. C* **2015**, 119, 19607.

[82] J. Zhou, H. Song, L. Ma, X. Chen, *RSC Adv.* **2011**, 1, 782.

[83] Z. Zhang, F. Ahmad, W. Zhao, W. Yan, W. Zhang, H. Huang, C. Ma, J. Zeng, *Nano Lett.* **2019**, 19, 4029.

[84] P. Chen, N. Zhang, S. Wang, T. Zhou, Y. Tong, C. Ao, W. Yan, L. Zhang, W. Chu, C. Wu, *Proc. Natl. Acad. Sci.* **2019**, 116, 6635.

[85] G. Liu, J. Shi, F. Zhang, Z. Chen, J. Han, C. Ding, S. Chen, Z. Wang, H. Han, C. Li, *Angew. Chem.Int. Ed.* **2014**, 53, 7295.

[86] Q. Bu, S. Li, K. Zhang, Y. Lin, D. Wang, X. Zou, T. Xie, *ACS Sustain. Chem. Eng.* **2019**, 7, 10971.

[87] H. J. Ahn, K. Y. Yoon, M. J. Kwak, J. H. Jang, *Angew. Chem.Int. Ed.* **2016**, 128, 10076.

[88] K. Appavoo, B. Wang, N. F. Brady, M. Seo, J. Nag, R. P. Prasankumar, D. J. Hilton, S. T. Pantelides, R. F. Haglund Jr, *Nano Lett.* **2014**, 14, 1127.

[89] Z. Zhang, J. T. Yates Jr, *Chem. Rev.* **2012**, 112, 5520.

[90] S. Li, Q. Zhao, D. Meng, D. Wang, T. Xie, *J. Mater. Chem. A* **2016**, 4, 16661.

[91] J. Xie, J. Chen, C. M. Li, *Int. J. Hydrog. Energy* **2017**, 42, 7158.

[92] L. Li, C. Liu, Y. Qiu, N. Mitsuzak, Z. Chen, *Int. J. Hydrog. Energy* **2017**, 42, 19654.

[93] M. P. Cardona, M. Li, W. Li, J. McCall, D. Wang, Y. Li, C. Yang, *Mater. Today Energy* **2018**, 8, 8.

[94] X. F. Yang, A. Wang, B. Qiao, J. Li, J. Liu, T. Zhang, *Acc. Chem. Res.* **2013**, 46, 1740.

[95] H. Fei, J. Dong, D. Chen, T. Hu, X. Duan, I. Shakir, Y. Huang, X. Duan, *Chem. Soc. Rev.* **2019**, 48, 5207.

[96] C. Zhu, S. Fu, Q. Shi, D. Du, Y. Lin, *Angew. Chem. Int. Ed.* **2017**, 56, 13944.

[97] H. Fei, J. Dong, Y. Feng, C. S. Allen, C. Wan, B. Volosskiy, M. Li, Z. Zhao, Y. Wang, H. Sun, P. An, W. Chen, Z. Guo, C. Lee, D. Chen, I. Shakir, M. Liu, T. Hu, Y. Li, A. I. Kirkland, X. Duan, Y. Huang, *Nat. Catal.* **2018**, 1, 63.

[98] L. Bai, C.-S. Hsu, D. T. Alexander, H. M. Chen, X. Hu, *J. Am. Chem. Soc.* **2019**, 141, 14190.

[99] Y. Hou, M. Qiu, T. Zhang, J. Ma, S. Liu, X. Zhuang, C. Yuan, X. Feng, *Adv. Mater.* **2017**, 29, 1604480.

[100] H. Lan, Y. Xia, K. Feng, A. Wei, Z. Kang, J. Zhong, *Appl. Catal. B* **2019**, 258, 117962.

Chapter 2 Ultrathin cobalt-manganese nanosheets: an efficient platform for enhanced photoelectrochemical water oxidation with electron-donating effect

2.1 Introduction

Photoelectrochemical (PEC) water splitting is a promising approach providing a sustainable and environmental route for direct conversion of solar energy to hydrogen, which has been considered to play a vital role in coping with energy shortage and environmental pollution.[1-3] Because of the sluggish kinetics of four-electron processes for oxygen evolution reaction (OER), construction of efficient photoanodes is significantly challenging for solar-driven PEC water splitting.[4, 5] α-Fe_2O_3 is one of the most promising photoanode materials due to its abundance, nontoxicity, superior stability, and moderate bandgap (~2.1 eV). However, the performance of α-Fe_2O_3 is significantlly restricted by its intrinsically poor conductivity, short hole diffusion length (2~4 nm) and limited photo-carrier lifetime.[6, 7] Thus, great efforts have been devoted to promoting those properties of α-Fe_2O_3 films, such as morphology controlling,[8-10] element doping[11-13] and heterojunction construction.[14-16] These strategies are expected to shorten the migration distance of charge carriers to the catalytic sites and reduce charge recombination in the bulk of α-Fe_2O_3 films. In this case, more photo-generated holes will be able to migrate to the catalytic surface. Afterwards, theses holes will inject into the electrolyte and eventually participate in the reaction. However, the hole injection process proceeds along with serious surface recombination due to the presence of surface trapped sites and complicated OER mechanism.[17] Therefore, enhancing the surface hole injection efficiency should be strived for to rule over the PEC water oxidation process.

Notably, loading oxygen evolution catalysts (OECs) has been regarded as a particularly effective approach to enhance the surface reaction kinetics of α-Fe_2O_3 films.[18-20] The introduction of OECs is mainly meant to provide surface reaction sites with lower overpotentials for holes transfer at the interface of photoelectrode/electrolyte. In addition, OECs can also act as selective trapping sites for photogenerated electrons/holes, thus suppressing the surface charge recombination.[21, 22] The employed OECs in PEC system usually originate from superior electrocatalysts, among which lots of transition metal-based OECs with low cost have been proved to have the ability of achieving low

overpotentials for electrochemical OER.[23] Because of complicated processes and intermediates involved in OER, it is usually difficult for any single metal-based OECs to achieve comprehensive enhancement for PEC water splitting. Therefore, it is believed that bimetallic compounds, which are adjustable with different metal sites, are promising OECs for PEC water oxidation owing to their abundant active sites and versatility in composition.[17, 24-27] In this regard, it is significantly important to investigate the actual functions of different metal sites in the compounds and obtain deep understanding on the explicit mechanism of this type of OECs for PEC water oxidation. By this way, it is possible to open new avenue and provide guidance for designing high-efficiency OECs with multi-metallic sites for PEC water splitting.

Herein, a delicate OEC/α-Fe_2O_3 architecture is constructed through uniform decoration of ultrathin Co-Mn nanosheets. It was discovered that incorporation of Mn site in the nanosheets could create electron donation to Co site and facilitate the activation of OH group, which drastically boosted the intrinsic catalytic activities for PEC water oxidation. As a result, the optimized photoanode exhibited an excellent photocurrent density of 2.09 mA cm^{-2} at 1.23 V vs. RHE under AM 1.5 G illumination (twice that of bare α-Fe_2O_3), as well as remarkable stability for over 10 h. The Co-Mn nanosheets could also tune the charge behaviors with significantly enhanced surface charge transfer efficiency and charge separation efficiency. Furthermore, this deposition method could also be applied in composites with other metals, which is believed to be a versatile and promising strategy to decorate photoanode with various metallic composites. These findings also provide an insight into the activation of PEC water oxidation through electron withdrawing/donating induced by bimetallic site in the composites.

2.2 Experimental section

2.2.1 Materials preparation

Preparation of α-Fe_2O_3 films: α-Fe_2O_3 films were prepared according to the previous report.[11] Briefly, 0.15 M of $FeCl_3$ and 1 M $NaNO_3$ were dissolved in 40 ml water with the pH adjusted to 1.50 by HCl. The aqueous solution was transferred to a Teflon-lined stainless steel autoclave. Then the fluorine-doped tin oxide (FTO) glasses, which were ultrasonically cleaned with ethanol, acetone and deionized water sequentially for 1h to remove the organic contamination and dust, were immersed and placed with the conductive side facing to the wall of the autoclave. The autoclave was then put into the

oven and heated at 95 ^{o}C for 4 h. A uniform layer of FeOOH (yellow color) was deposited on the FTO glasses. The substrates were washed with deionized water to remove the residual FeOOH and subsequently calcinated at 550 °C for 2 h and 800 °C for additional 20 min.

Deposition of Co-Mn nanosheets on the α-Fe_2O_3 films: The Co-Mn nanosheets was electrodeposited from a 2 mM solution with $Co(NO_3)_2$ and $Mn(NO_3)_2$ by applying a cathodic current density of 1 mA cm^{-2}. The deposition durations were varied to 15, 30, 60, 90 and 120s for obtaining the optimized deposition time and investigating the growth kinetics of Co-Mn nanosheets. In order to obtain the optimized ratio of Co and Mn, different Co/Mn ratios of deposited composites were investigated by varying the Co/Mn ratios in the precursor solution. After electrodeposition, the as-obtained samples were thoroughly cleaned with deionized water for several times and dried at 40 ^{o}C for 6 h. Other hybrid materials such as Ni-Mn composite and Fe-Mn composite were prepared by the same procedure as that used for the synthesis of Co-Mn nanosheets except different metal precursors.

2.2.2 Material characterization

In our investigation, X-ray diffraction (XRD) patterns were measured on an X-ray diffractometer (X'pert powder, PANalytical B.V.) with Copper-Kα radiation under 40 kV and 30 mA. Optical absorption properties of the photoelectrodes were measured over an ultraviolet–visible (UV–vis) spectrophotometer (UV-2700, Shimadzu). The morphologies of the films were characterized by scanning electron microscopy (SEM) (S-4800, Hitachi) and transmission electron microscopy (TEM) (FEI Tecnai G2 F30), coupled with energy dispersive spectrometer (EDS) to determine elementary composition. X-ray photoelectron spectroscopy (XPS) (PHI Quantera SXM, ULVAC-PHI) experiments were performed in a Theta probe using monochromated Mg Kα x-rays at hν = 1486.6 eV. Peak positions were internally referenced to the C 1s peak at 284.6 eV.

2.2.3 Photoelectrochemical measurement

The PEC characterization was carried out using three-electrode cell system, in which a piece of pure platinum and an Ag/AgCl (3 M KCl) electrode as counter and reference electrodes, respectively. 1M NaOH aqueous solution was used as electrolyte (pH=13.6). The available electrode area immersed in the electrolyte solution was fixed to 1.0×1.0 cm^2. AM 1.5 G solar simulation (WXS-80C-3 AM 1.5 G) with a light intensity of 100

mW cm^{-2} was utilized as the light sources. Photocurrent–potential (*J*–*V*) curves were obtained using linear sweep voltammogram in a voltage window of 0.6 ~ 1.6 V vs. RHE with a scan rate of 20 mV s^{-1} on an electrochemical workstation (ALS/CH model 650A) and the light was chopped manually at regular intervals. Electrochemical impedance spectroscopy (EIS) test was performed at a DC bias of 1.23 V vs. RHE under AM 1.5 G illumination (frequency range: 0.1 ~ 100000 Hz). Mott–Schottky curves were obtained from 0.2 to 1.0 V vs. RHE in the dark at a frequency of 1000 Hz. All the potentials in the PEC performance vs. Ag/AgCl could be converted to the RHE scale using the equation below.

$$E_{RHE} = E_{Ag/AgCl} + 0.059 \times pH + E^0_{Ag/AgCl} \quad (1)$$

Where E_{RHE} is the converted potential vs. RHE. $E_{Ag/AgCl}$ represents the experimental result vs. Ag/AgCl and $E^0_{Ag/AgCl}$ is 0.197 V at ambient temperature of 25 °C.

Applied bias photon-to-current efficiency (ABPE) was calculated using the equation below.

$$ABPE\ (\%) = \frac{J \times (1.23 - V_b)}{P_{light}} \times 100\% \quad (2)$$

where J refers to the photocurrent density (mA cm^{-2}) obtained from the electrochemical workstation. V_b represents the applied bias vs. RHE (V), and P_{light} is the total light intensity of AM 1.5 G (100 mW cm^{-2}).

Incident photon to electron conversion efficiency (IPCE) was measured using a motorized monochromator (M10; Jasco Corp.), which was calculated using the following equation.

$$IPCE\ (\%) = \frac{J \times 1240}{\lambda \times P_{light}} \times 100\% \quad (3)$$

where J is the photocurrent density (mA cm^{-2}) obtained from the electrochemical workstation. λ and P_{light} refer to the incident light wavelength (nm) and the power density obtained at a specific wavelength (mW cm^{-2}), respectively.

According to the Mott–Schottky curves, the flat-band potential (E_{fb}) values were obtained from the intercept of the x-axis and the donor concentration (N_d) can be calculated from the following equations.

$$N_d = \frac{2}{e\varepsilon\varepsilon_0} \times \left[\frac{d\left[\frac{1}{C^2}\right]}{dV_s} \right]^{-1} \quad (4)$$

Where C denotes the space charge region's capacitance, e is electron charge and equal to 1.6×10^{-19} C, ε≈80 represents the dielectric constant of α-Fe_2O_3, the vacuum permittivity of ε_0 is 8.854×10^{-14} F/cm and V is the applied potential on the photoanode.

The water oxidation photocurrent density could be calculated by the following formula,

$$J_{PEC} = J_{abs} \times \eta_{sep} \times \eta_{inj} \quad (5)$$

J_{abs} is the photocurrent density when the absorbed photon completely converting into current. As a hole scavenger, Na_2SO_3 can effectively trap the holes that arrived to the surface, without influencing the charge separation on the electrode (η_{inj} assumed to be 100%). Therefore, the charge separation efficiency in the bulk (η_{sep}) and surface charge injection efficiency (η_{inj}) could be deduced with following equations.

$$\eta_{\mathrm{sep}} = \frac{J^{Na_2SO_3}}{J_{abs}} \quad (6)$$

$$\eta_{\mathrm{inj}} = \frac{J^{H_2O}}{J^{Na_2SO_3}} \quad (7)$$

Where J^{Na2SO3} and J^{H2O} are photocurrent densities obtained in 1 M NaOH electrolyte with and without 1 M Na_2SO_3, respectively. The J_{abs} was calculated by the overlapped areas between UV–vis absorption spectrum and AM 1.5G solar spectrum according to the following equation:

$$J_{abs} = \int \frac{\lambda}{1240} \cdot \varphi\mathrm{AM\ 1.5G}(\lambda) \cdot \mathrm{LHE}\ \mathrm{d}\lambda \quad (8)$$

$$\mathrm{LHE} = 1 - 10^{-A(\lambda)} \quad (9)$$

Where λ is the wavelength (nm), φAM 1.5G(λ) provides the simulated solar spectral irradiance (W m^{-2} nm^{-1}), LHE is the light harvesting efficiency, A(λ) is the absorbance at wavelength λ.

The experiment of gas evolution for water splitting was carried out in a completely sealed quartz reactor. The electrode with an area of 1 cm^2 was immersed in the electrolyte in a three-electrode configuration. Prior to the reaction and sealing processes, the electrolyte was purged with argon gas. The generated H_2 and O_2 were analysed with a thermal conductivity detector (TCD) gas chromatograph (Shimadzu GC-8AIT, argon carrier). Similarly, AM 1.5 G solar simulation (WXS-80C-3 AM 1.5 G) with a light intensity of 100 mW cm^{-2} was utilized as the light sources directly without adding any light filter.

2.3 Results and discussion

2.3.1 The optimization of Co-Mn nanosheets

The synthetic approach of α-Fe_2O_3 films and fabrication processes of Co-Mn nanosheets are depicted in Figure 2.1a. Firstly, a yellow layer of FeOOH nanorods (Figure 2.1b) was fabricated on a conducting glass substrate using a hydrothermal method. The FeOOH transformed to α-Fe_2O_3 via calcination process with film's color changing from yellow to red. Then, Co-Mn nanosheets were deposited on the surface of α-Fe_2O_3 (Co-Mn-α-Fe_2O_3) with a facile and quick electrodeposition method. The optimized electrodeposition time is 30 s and Co/Mn ratio in the precursor solution is 0.5:0.5 (confirmed by morphology and photocurrent densities in Figure S5~S8). Hereafter, all the characterizations and discussion of Co-Mn-α-Fe_2O_3 films are based on these two optimized parameters, unless stated otherwise.

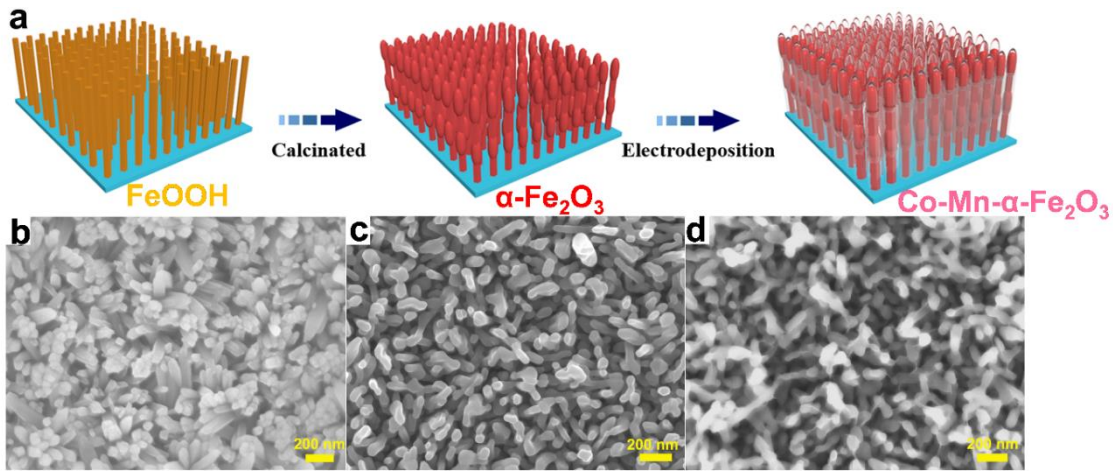

Figure 2.1 a) Scheme of fabrication processes of α-Fe_2O_3 films and electrodeposition procedures of ultrathin Co-Mn nanosheets; top-view SEM images of b) FeOOH, c) α-Fe_2O_3, d) Co-Mn-α-Fe_2O_3.

To optimize the Co-Mn nanosheets, contrast experiments with different time and varied Co-Mn ratio were carried out to investigate the morphological evolution of modified films. It can be observed that inconspicuous change in morphology (with few nanosheets coated on α-Fe_2O_3) is observed with electrodeposition time of 15 s (Figure 2.2a). With electrodeposition time increasing to 60 s, nanosheets on the surface of α-Fe_2O_3 nanorods become somewhat obvious (Figure 2.2b). A much more intensive coating layer grows on the surface of α-Fe_2O_3 nanorods with electrodeposition time of 90 s (Figure 2.2c). When the reaction time increases to 120 s, the whole surface of α-Fe_2O_3

nanorods is densely covered by the overlayer of Co-Mn nanosheets (Figure 2.2d), which may hinder the light capture and the transport of photo-induced charge carries. In order to investigate the influence of Co and Mn on the morphology of the nanosheets, we further varied Co and Mn ratio in the precursor solution with optimized electrodeposition time of 30 s. Different morphologies of films electrodeposited with different Co-Mn ratios are shown in Figure 2.3. Element of Co is conducive to form nanosheets covered on the surface of α-Fe_2O_3 nanorods. The more ratio of Co added, the more obvious and thicker nanosheets formed. If only the Mn element exists, the nanosheets morphology would be hardly developed (Figure 2.3d). The result is consistent with HRTEM images, which presented that Co element formed the amorphous nanosheets of $Co(OH)_x$, while Mn element transformed to Mn_3O_4 nanocrystals during the electrodeposition.

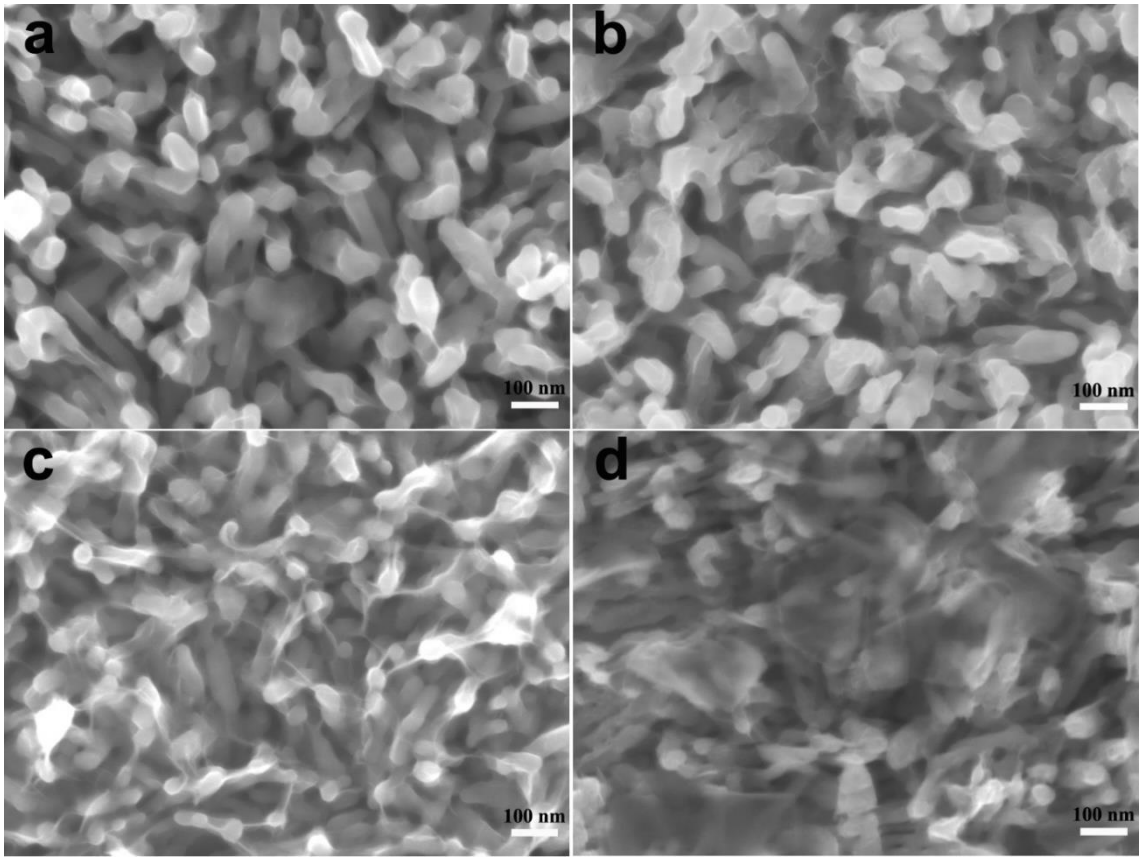

Figure 2.2 Time-dependent SEM images of the Co-Mn-α-Fe_2O_3 films obtained at electro-deposition of (a) 15 s, (b) 60 s, (c) 90 s, (d)120 s, respectively.

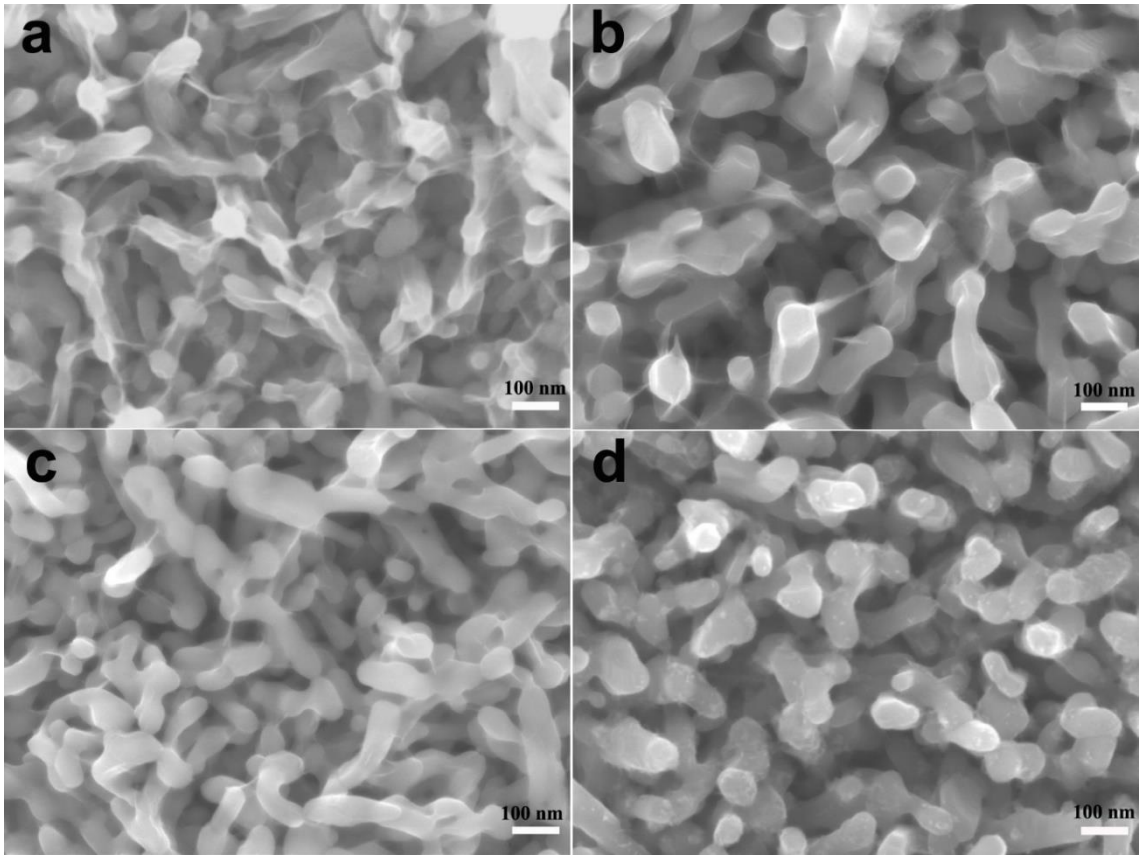

Figure 2.3 SEM images of films electrodeposited with different Co-Mn ratio: (a) Co-α-Fe_2O_3, (b) $Co_{0.75}$-$Mn_{0.25}$-α-Fe_2O_3, (c) $Co_{0.25}$-$Mn_{0.75}$-α-Fe_2O_3 and (d) Mn-α-Fe_2O_3.

By comparing visual activity (the photocurrent densities at 1.23 V vs. RHE obtained from *J–V* curves), optimized electrodeposition time and Co-Mn ratio in precursor solution could be acquired. As shown in Figure 2.4, the activities of Co-Mn-α-Fe_2O_3 photoanodes with different electrodeposition time were evaluated. It was revealed that Co-Mn-α-Fe_2O_3 photoanode with electrodeposition time of 30 s presents the highest photocurrent density. After then, the continue increase of electrodeposition time from 30 s would lead to a negative effect on photocurrent densities of the photoanodes, which may due to intensive covering of Co-Mn nanosheets over α-Fe_2O_3 nanorods (Figure 2.2). And the optimized Co-Mn ratio in precursor solution is 0.5:0.5 by comparing the photocurrent densities of different photoanodes (Figure 2.5 and Figure 2.13)

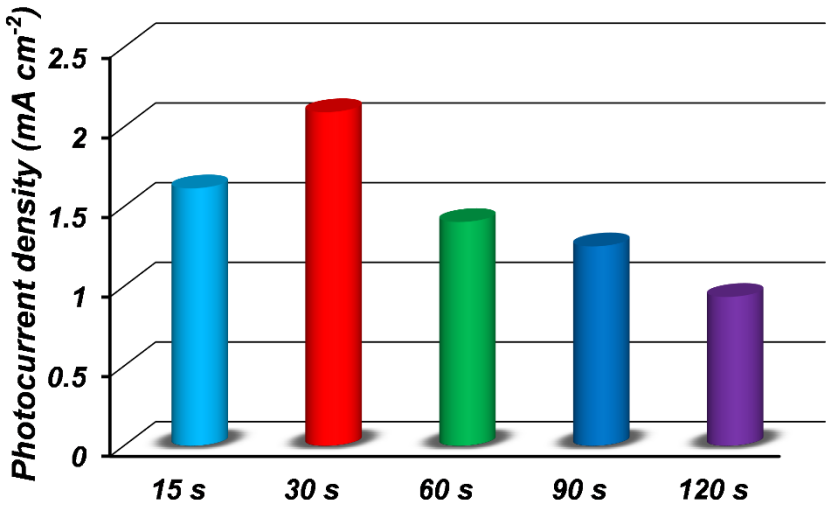

Figure 2.4 Photocurrent densities of Co-Mn-α-Fe_2O_3 films electrodeposited for 15 s, 30 s, 60 s, 90 s and 120 s at 1.23 V vs. RHE under AM 1.5 G illumination.

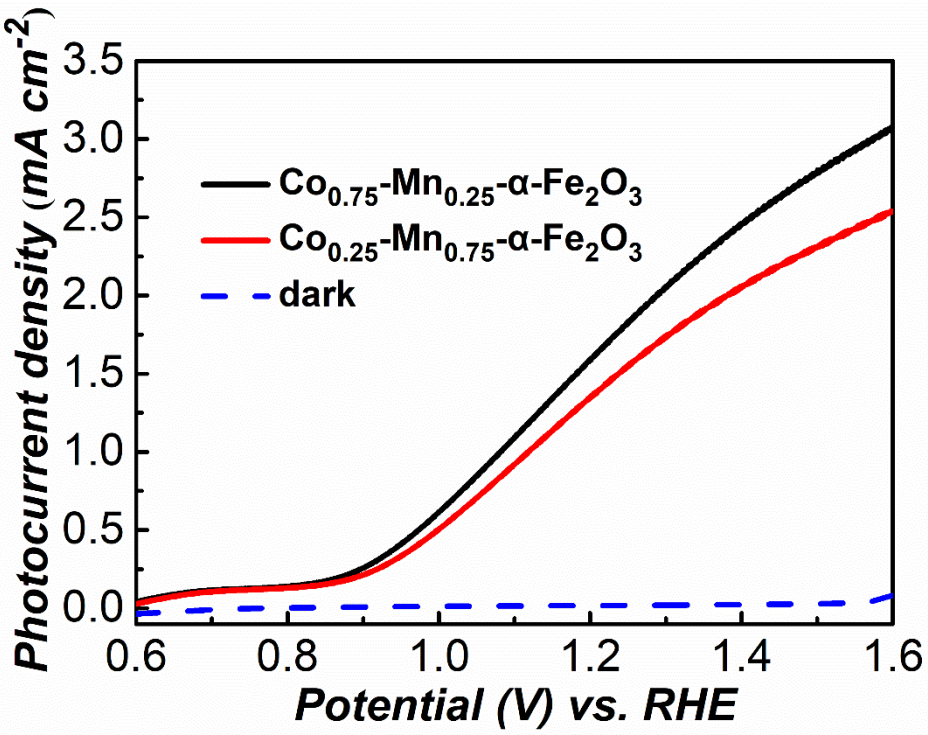

Figure 2.5 *J–V* curves of the $Co_{0.75}$-$Mn_{0.25}$-α-Fe_2O_3 and $Co_{0.25}$-$Mn_{0.75}$-α-Fe_2O_3.

2.3.2 Characterization of the modified films with Co-Mn nanosheets

The XRD patterns of α-Fe_2O_3 and Co-Mn-α-Fe_2O_3 films in Figure 2.6a display similar diffraction peaks ascribed to α-Fe_2O_3 and SnO_2 (from FTO substrate). It is notable that only distinct peaks of α-Fe_2O_3 at 35.6° and 63.9° could be observed (well indexed to the α-Fe_2O_3 crystal structure of PDF # 33-0664), presumably owing to its relatively small

size and low loading amount compared with the SnO_2. There is no peak ascribed to Co-Mn nanosheets in XRD results, which may be too thin to be detected. Figure 2.6b shows UV–vis spectra of α-Fe_2O_3 and Co-Mn-α-Fe_2O_3 films. Bare α-Fe_2O_3 exhibits a light absorption edge of ~ 580 nm with a band gap energy of 2.09 eV (Tauc plots in Figure 2.7), which conforms well with the reported values.[28] After being decorated with Co-Mn nanosheets, the absorption intensity and bandgap remain almost unchanged, indicating ultrathin Co-Mn nanosheets have negligible influence on light adsorption of α-Fe_2O_3. Therefore, XRD and UV–vis results manifest that the structure and optical absorption of α-Fe_2O_3 film would not be affected by the decoration of Co-Mn nanosheets.

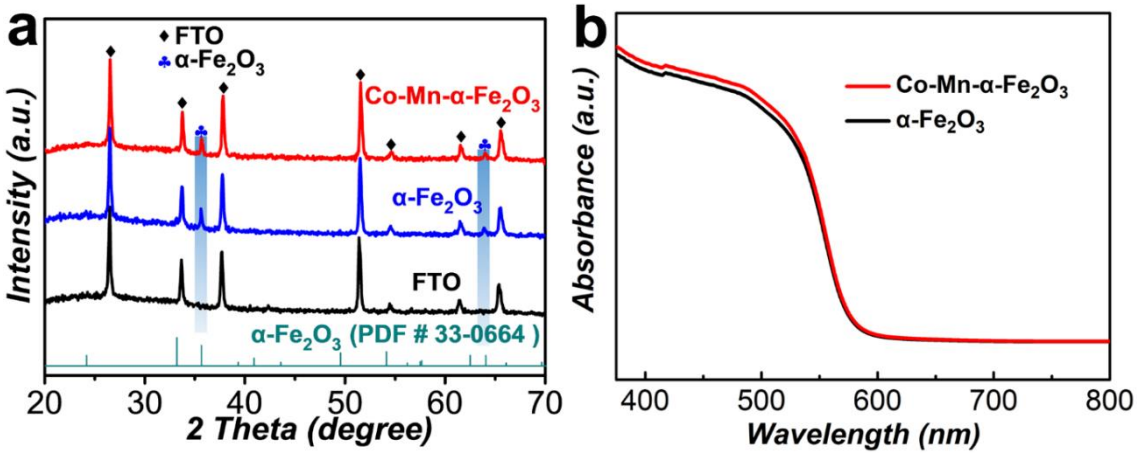

Figure 2.6 a) XRD patterns of Co-Mn-α-Fe_2O_3, α-Fe_2O_3 and FTO, b) UV–visible diffuse reflection spectra of Co-Mn-α-Fe_2O_3 and α-Fe_2O_3.

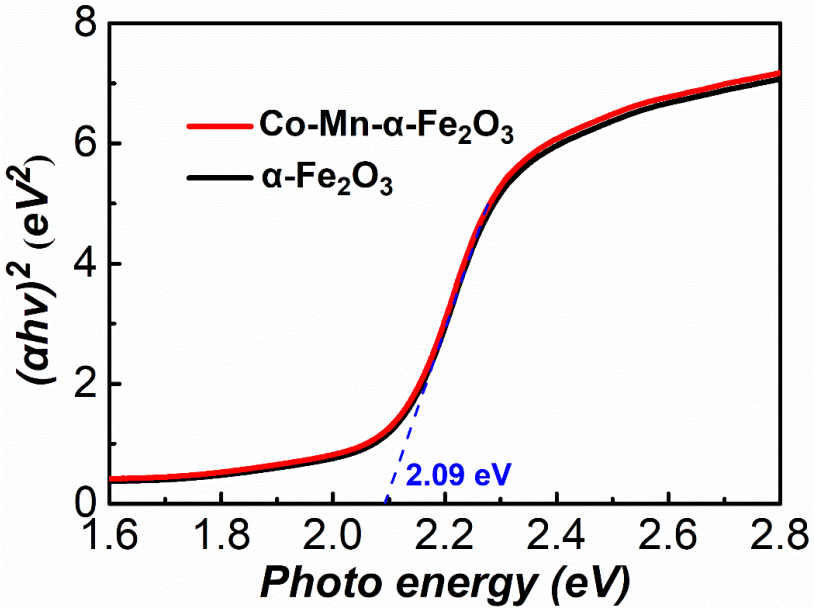

Figure 2.7 Tauc plots of Co-Mn-α-Fe_2O_3 and α-Fe_2O_3.

The obtained α-Fe_2O_3 film displays a one-dimensional wormlike structure of nanorods array (Figure 2.1c). The thickness of the film is approximately 370 nm as identified by cross-section SEM image (Figure 2.8). Compared with pure α-Fe_2O_3 film, an ultrathin layer is fully covered on the surface of α-Fe_2O_3 after integration of Co-Mn nanosheets (images with larger magnification are presented in Figure 2.9). TEM image in Figure 2.10a further confirms that Co-Mn nanosheets are compactly coated on well crystalized α-Fe_2O_3 nanorods and the layer thickness is only several nanometers. High-resolution TEM (HRTEM) images show that deposited Co-Mn nanosheets consist of amorphous layers and ultrasmall nanocrystals (Figure 2.10b). According to Yan's results with similar method, the amorphous layers are $Co(OH)_x$ and the ultrasmall nanocrystals are Mn_3O_4.[29] The nanocrystalline Mn_3O_4 are embedded in the $Co(OH)_x$ matrix by forming solid interparticle contact between these two phases, which can be described as a kind of mosaic structure. The lattice fringes with spacing of 0.204, 0.248 and 0.309 nm correspond to (220), (211) and (112) crystal planes, unveiling again that the nanocrystals are tetragonal Mn_3O_4.[30] EDS elemental mapping images illustrate that Co and Mn elements are relatively uniformly distributed along with Fe and O elements (Figure 2c~2g), further verifying the homogeneous coating of Co-Mn nanosheets on the surface of α-Fe_2O_3.

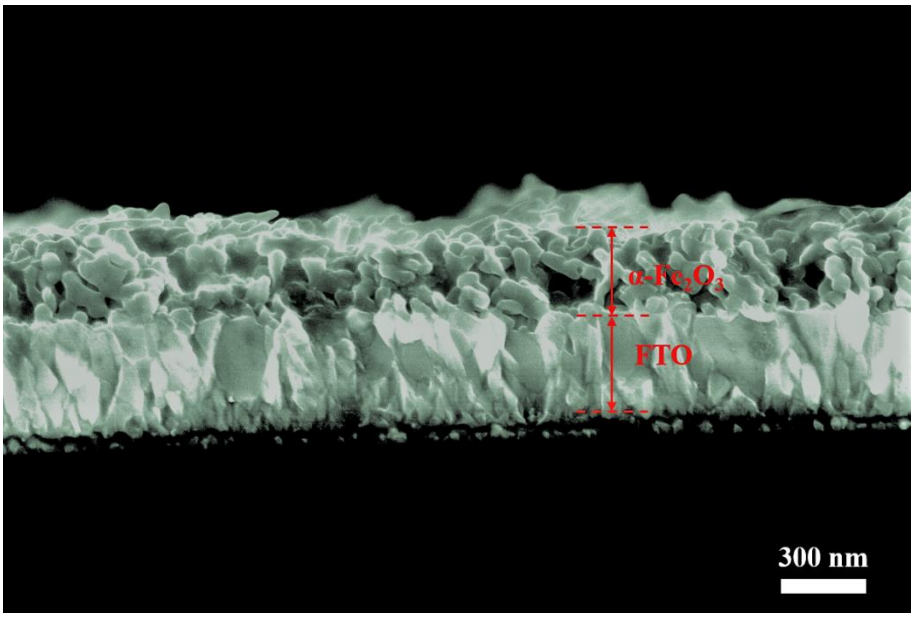

Figure 2.8 Cross-section SEM image of α-Fe_2O_3 nanorods.

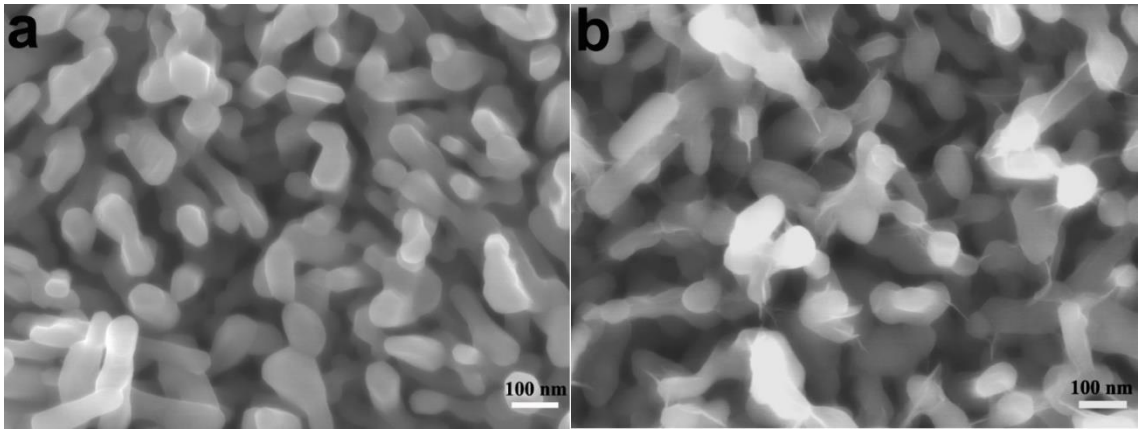

Figure 2.9 Top-view SEM images with larger magnification of a) α-Fe_2O_3 and b) Co-Mn-α-Fe_2O_3.

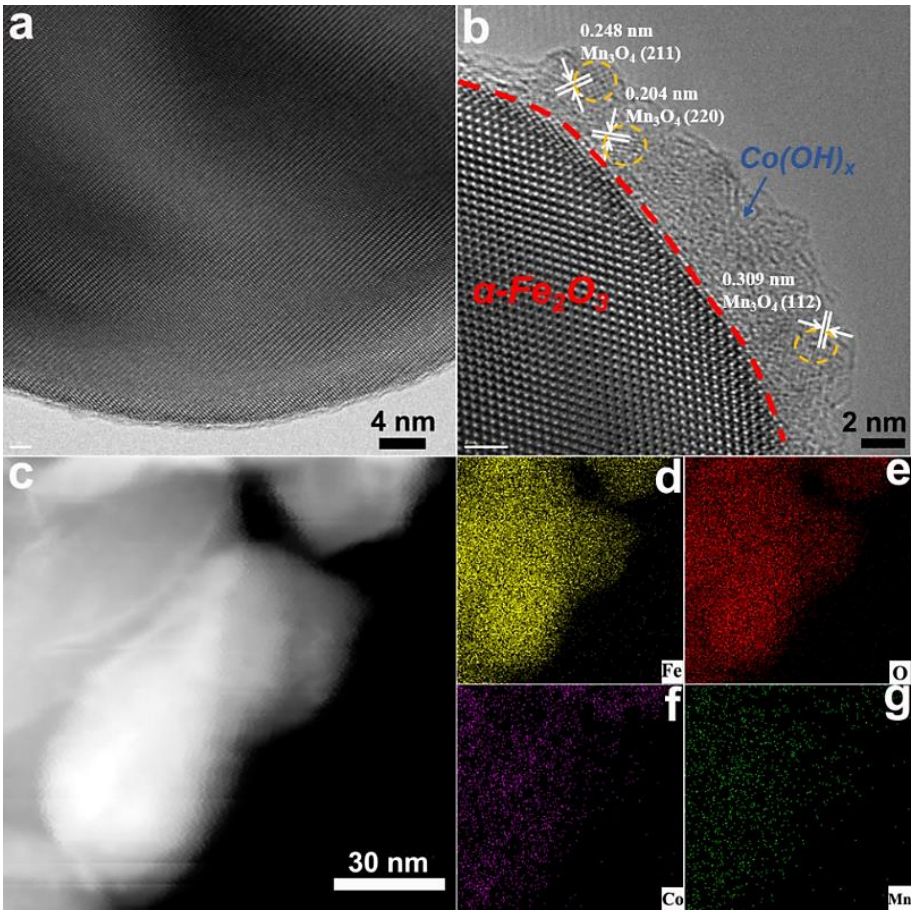

Figure 2.10 a) TEM image, b) HRTEM image, c-g) EDS elemental mapping images of Co-Mn-α-Fe_2O_3 refer to the signals of Fe, O, Co and Mn, respectively.

The chemical states and elemental composition of Co-Mn-α-Fe_2O_3 film were further characterized by X-ray photoelectron spectroscopy (XPS). The high resolution XPS spectrum of Fe 2p (Figure 2.12a) is composed of two major peaks located at 710.5 eV

and 724.1 eV (corresponding to Fe $2p_{1/2}$ and Fe $2p_{3/2}$), as well as a satellite peak (denoted as "Sat") at 718.5 eV, which confirms the existence of Fe^{3+}.[31] Additionally, the Fe 2p peaks are shifted to lower binding energy after the coating of Co-Mn nanosheets (Figure 2.11a), revealing that electrons can be transferred from Co-Mn nanosheets to α-Fe_2O_3. This phenomenon confirms that Co-Mn nanosheets could facilitate charge transfer on the photoanode and thus reduce charge recombination. The O 1s spectrum (Figure 2.12b) can be fitted into two peaks, which are assigned to the lattice oxygen (O_L) and hydroxyl groups bonded with metal cations (O_H), respectively.[32] The Co 2p spectrum (Figure 2.11b) also shows two main peaks at around 780.2 eV and 796.1 eV (corresponding to Co $2p_{3/2}$ and Co $2p_{1/2}$), with two shake-up satellite peaks (about 786.0 eV and 802.8 eV). The two main peaks can be deconvolved into four peaks, corresponding to Co (III) and Co (II).[17, 33] The fitting results indicate that the content of Co (III) is relatively higher than Co (II) in the composite, which is favorable for the superior catalytic activity.[17] Additionally, satellite peak located at 786.0 eV can be attributed to the Co-hydroxyl groups, which is consistent with the XPS result of O 1s at 531.3 eV.[34] The formation of Co-hydroxyl groups would yield positive effects on the OER performance, since it might induce structural flexibility along with optimized coordination states.[35] Similarly, the Mn 2p spectrum (Figure 2.11c) is also composed of two main peaks (could be fitted to Mn (II) and Mn (III), respectively), which is consistent with the TEM results.[30] In order to investigate the electronic structure modulation between Co and Mn, the Co 2p spectra of Co-Mn-α-Fe_2O_3 and Co-α-Fe_2O_3 are compared in Figure 2.11d. The composition and configuration of these two spectra are similar. However, an obvious negative shift (0.57 eV) can be observed, indicating the electron donation from Mn site to Co site. This strong electronic interaction between Co and Mn would make Co site more readily to accept holes, which might facilitate the generation of intermediates and hence accelerate the O_2 production. The electron donation would also induce Mn_3O_4 to become more Lewis acidic, whereby the activation of OH group through Lewis acid-base interaction could occur.[36]

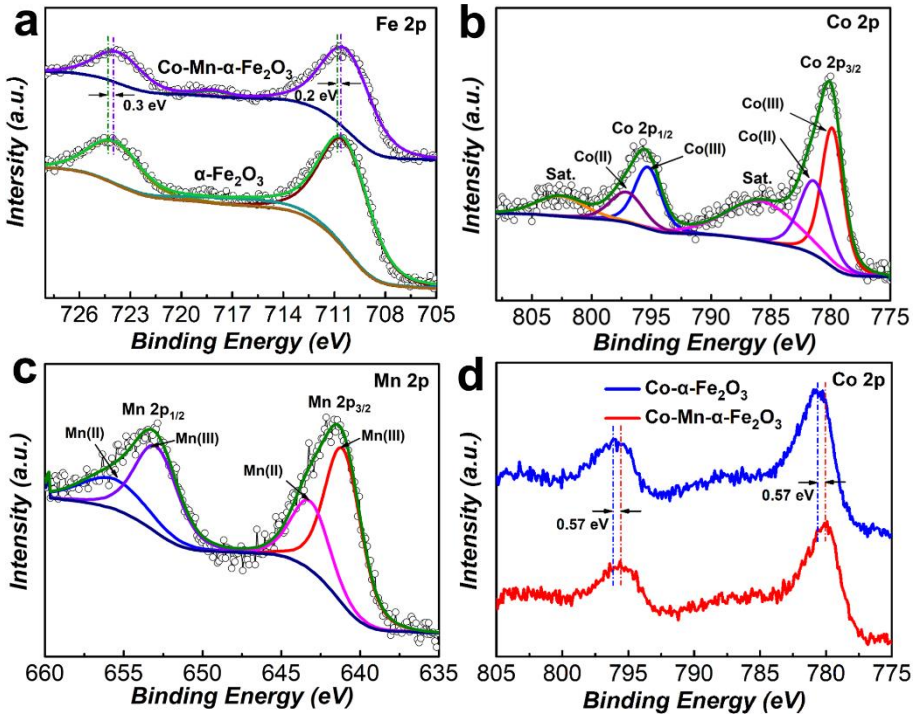

Figure 2.11 a) Fe 2p XPS spectra of α-Fe_2O_3 and Co-Mn-α-Fe_2O_3, b) Co 2p and c) Mn 2p XPS spectra of Co-Mn-α-Fe_2O_3, d) Co 2p XPS spectra of Co-α-Fe_2O_3 and Co-Mn-α-Fe_2O_3.

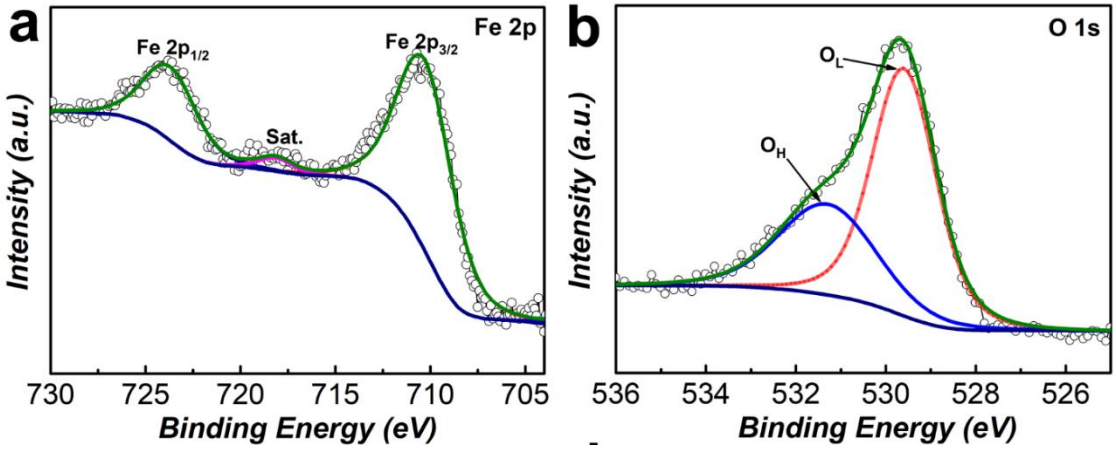

Figure 2.12 a) Fe 2p and b) O 1s XPS spectra of Co-Mn-α-Fe_2O_3.

2.3.3 PEC performance characterization

The PEC performance of different photoanodes were evaluated by measuring the photocurrent density versus applied potential (*J*–*V*) curves under AM 1.5 G irradiation. As displayed in Figure 2.13a, a photocurrent density of 2.09 mA cm^{-2} at 1.23 V vs. RHE is achieved for Co-Mn-α-Fe_2O_3 photoanode, about 1.6 times higher than that of bare α-Fe_2O_3 photoanode (0.83 mA cm^{-2}). In addition, the onset potential shows a great cathodic

shift compared with pristine α-Fe_2O_3 photoanode, indicating a lower overpotential for water oxidation as a result of decoration of Co-Mn nanosheets. The enhanced photocurrent density and lower onset potential of Co-Mn-α-Fe_2O_3 photoanode could be attributed to the compact contact between ultrathin Co-Mn nanosheets and oriented α-Fe_2O_3 nanorods. Such intimate interaction was expected to facilitate the charge separation at the photoelectrode/electrolyte interface, which would promote the oxygen evolution kinetics of the photoanode.[25] Additionally, the photocurrent density at 1.23 V vs. RHE of Co-Mn-α-Fe_2O_3 photoanode is also much higher than Mn-α-Fe_2O_3 (1.17 mA cm^{-2}), Co-α-Fe_2O_3 (1.56 mA cm^{-2}) and other photoanodes with different Co/Mn ratios (Figure 2.5) under the same condition. This phenomenon elucidates that OECs with single element can hardly realize the acceleration of all processes for PEC water oxidation simultaneously. Moreover, suitable Co/Mn ratio is significantly important to achieve remarkable performance for the reaction.

In order to explain the importance of appropriate Co/Mn ratio and further illustrate the electron-withdrawing/donating effect between Co and Mn sites, Co 2p spectra of $Co_{0.75}$-$Mn_{0.25}$-α-Fe_2O_3 (the ratio of Co and Mn in precursor solution is 0.75:0.25) and $Co_{0.25}$-$Mn_{0.75}$-α-Fe_2O_3 (the ratio of Co and Mn in precursor solution is 0.25:0.75) are compared with Co-α-Fe_2O_3 (Figure 2.14). Similar with the result of Co-Mn-α-Fe_2O_3, obvious negative shifts of 0.32 eV and 0.74 eV can be observed for $Co_{0.75}$-$Mn_{0.25}$-α-Fe_2O_3 and $Co_{0.25}$-$Mn_{0.75}$-α-Fe_2O_3, respectively. The shift of Co 2p spectra become larger with the increasing of Mn ratio, verifying the stronger electron-donating effect from Mn site to Co site. However, the $Co_{0.25}$-$Mn_{0.75}$-α-Fe_2O_3 only showed moderate photocurrent density although with the strongest interaction between Co and Mn sites. The presumed reason could be attributed to the low concentration of Co, suggesting that the active sites might be not enough. The XPS results of $Co_{0.75}$-$Mn_{0.25}$-α-Fe_2O_3 and $Co_{0.25}$-$Mn_{0.75}$-α-Fe_2O_3, combined with the results in Figure 2.11d, unravel the importance of electron-donating effect for the activity. Generally, the formation of the absorbed OOH species during OER is considered as the rate limiting step for further processes.[37] Furthermore, the interaction between absorbed OOH species and 3d orbital of transition metal sites determines the OER activities of transition metal-based catalysts.[24, 38] In this regard, the Mn sites would low the energy of Co atoms and enable the Co sites to gain more electrons, thus inducing the electron-donating effect. The increase of electron density in 3d orbital of Co sites was

previously reported to favor the generation of absorbed OOH species, which is beneficial for facilitating the OER processes.[39, 40]

The photoconversion efficiencies of different photoanodes were evaluated by the applied bias photon-to-current conversion efficiency (ABPE), calculated from the $J-V$ curves. As shown in Figure 2.13b, the ABPE of α-Fe_2O_3 photoanode presents a peak of only 0.08% at 1.04 V vs. RHE, while the ABPE peaks of Mn-α-Fe_2O_3 and Co-α-Fe_2O_3 photoanodes reach 0.12% (at 1.02 V vs. RHE) and 0.19% (at 0.99 V vs. RHE), respectively. In contrast, Co-Mn nanosheets can further promote the maximum ABPE to as high as 0.25% at a lower potential of 0.98V vs. RHE, which is nearly threefold higher than that of bare α-Fe_2O_3 photoanode. In order to further verify the catalytic effect of Co-Mn nanosheets, the incident photo-to-electron conversion efficiency (IPCE) spectra are displayed as a function of wavelength from 360 to 600 nm in Figure 2.13c. An obvious enhancement can be observed at the whole range of spectrum after modification with the OECs. It is demonstrated that Co-Mn-α-Fe_2O_3 photoanode achieves the maximum IPCE value of 39.1% at 360 nm, about 3.7 times higher than that of bare α-Fe_2O_3 photoanode (10.6% at 360 nm). The enhanced IPCE of Co-Mn-α-Fe_2O_3 photoanode is also consistent with the result of $J-V$ curves, both of which are comparable with recent reported results of α-Fe_2O_3 based photoanodes coupled with different OECs (Table 2.1). Notably, the trends of IPCE with wavelengths for all photoanodes are similar (with an onset wavelength of about 600 nm, which are also in accordance with the UV−vis spectra), but the IPCE values exhibit significant improvement after decoration with Co-Mn nanosheets. Considering the same semiconductor properties of α-Fe_2O_3, the only difference between these photoanodes is the decoration of different OECs. Accordingly, the enhanced performance is not related to the light absorption, but reduced electron trapping sites at the surface and better charge carrier extraction efficiency by the formation of interface between Co-Mn nanosheets and α-Fe_2O_3 nanorods (will be disscussed in more detail later).[41]

To examine the photo-response of different photoanodes over time, current-time curves were measured at 1.23 V vs. RHE under chopped illumination (Figure 2.13d). The Co-Mn-α-Fe_2O_3 photoanode showed a quick and steady current response, with a highest stable photocurrent density of 2.07 mA cm^{-2}, which is nearly same as the $J-V$ curve data. It is notable that bare α-Fe_2O_3 photoanode presented a small spike once the light was turned on. This phenomenon might be attributed to the slow OER kinetics compared with

the rapid hole consumption to the surface trapping states, inducing an electron flux associated with recombination. To obtained steady photocurrents, the prevalent strategy is to eliminate those surface trapping sites for holes accumulation by introducing a passivation layer.[42-44] After being decorated with Co-Mn nanosheets, a uniform layer could be formed on the surface of α-Fe_2O_3 nanorods. In this case, the photoanode exhibited quick current response to the chopped light and the photocurrent could be reproduced via several cycles, which could be ascribed to the enhanced charge utilization efficiency and passivated surface trapping sites.

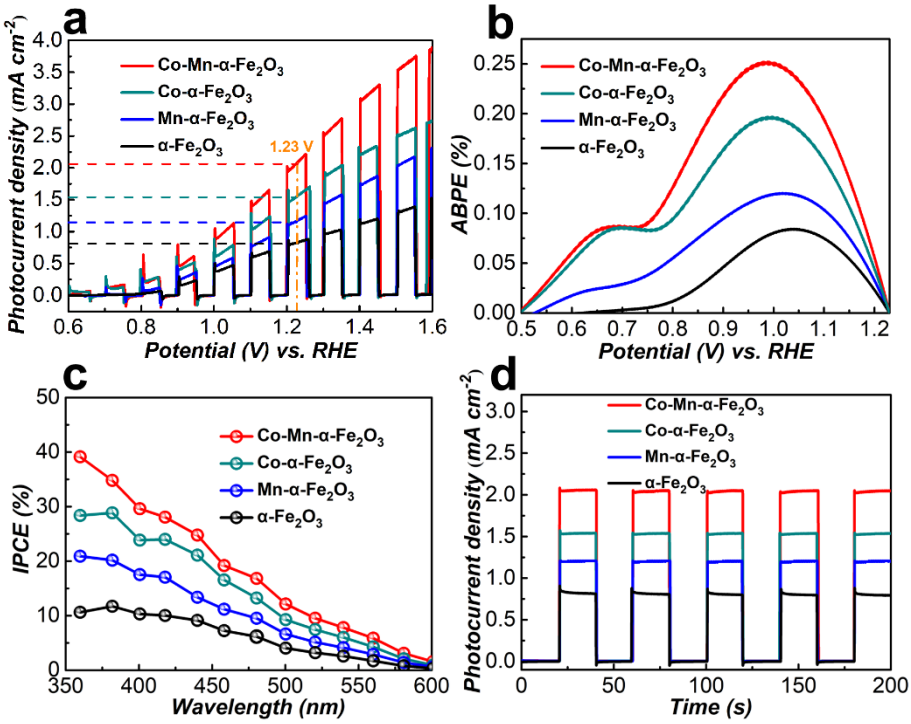

Figure 2.13 a) *J*–*V* curves, b) ABPE curves, c) IPCE curves and d) current–time curves of pristine α-Fe_2O_3, Mn-α-Fe_2O_3 (decorated with Mn compound), Co-α-Fe_2O_3 (decorated with Co compound) and Co-Mn-α-Fe_2O_3 photoanodes. The IPCE and current–time curves were measured at 1.23 V vs. RHE under AM 1.5 G illumination.

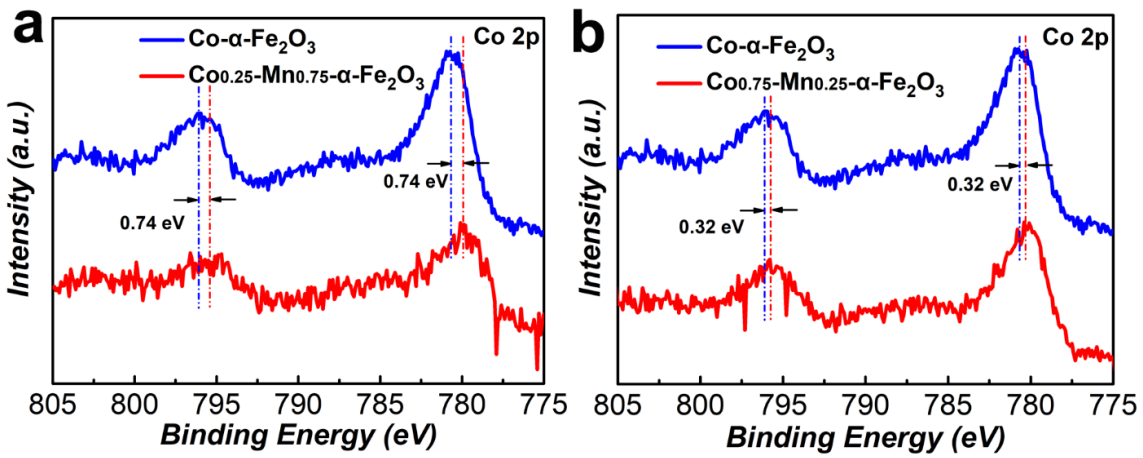

Figure 2.14 Co 2p XPS spectra of (a) Co-α- Fe_2O_3 and $Co_{0.25}$-$Mn_{0.75}$-α-Fe_2O_3, (b) Co-α-Fe_2O_3 and $Co_{0.75}$-$Mn_{0.25}$-α-Fe_2O_3.

Long-term stability test was carried out at 1.23 V vs. RHE under AM 1.5 G illumination to probe the durability of the photoelectrodes under constant working condition. As shown in Figure 2.15a, Co-Mn-α-Fe_2O_3 photoanode demonstrates an impressive stability over 10 h consecutive illumination, still retaining approximately 97 % of the initial photocurrent density. The H_2 on the Pt electrode and the O_2 on the Co-Mn-α-Fe_2O_3 photoanode are 363.6 and 179.6 μmol cm^{-2} after 10 h of consecutive light illumination, respectively, corresponding to the ≈2:1 ratio of the water splitting reaction (Figure 2.15b). In addition, a high Faradaic efficiency of 95.8% is calculated based on the amount of the generated oxygen and the holes, indicating that nearly all the photogenerated holes are used for water oxidation. Furthermore, SEM images of Co-Mn-α-Fe_2O_3 photoanode after stability test confirm that the morphology of Co-Mn nanosheets is maintained (Figure 2.16), indicating that Co-Mn nanosheets are stable as OEC under photooxidation environment. Moreover, the fitting XPS result of Co 2p for Co-Mn-α-Fe_2O_3 photoanode after OER shows that the main peaks are similar compared to the result before OER (Figure 2.17), with only slightly increased content of Co (III) after stability test. The results after stability test further highlight the pivotal role of Co-Mn nanosheets in preventing photo-corrosion and prompting PEC performance of photoanode.

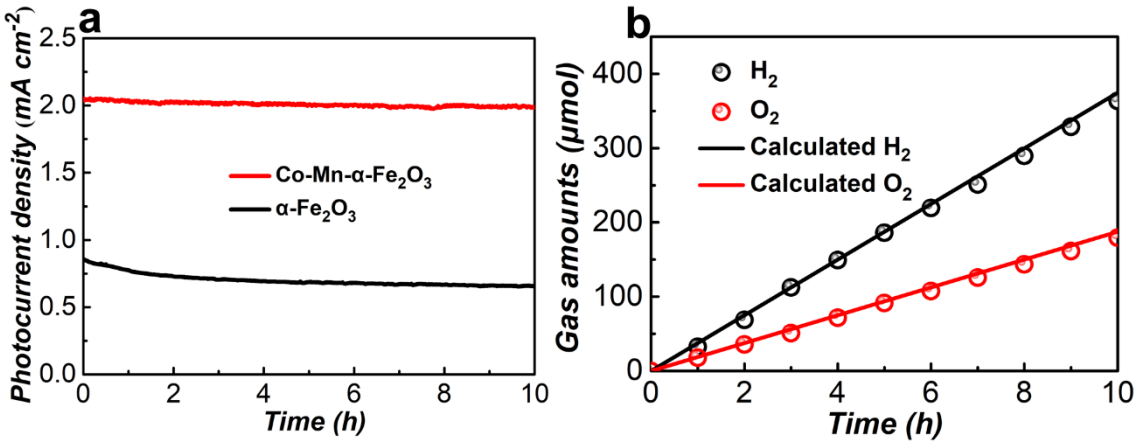

Figure 2.15 a) Stability test of α-Fe_2O_3 and Co-Mn-α-Fe_2O_3 photoanodes for 10 h; b) Gas evolution curves for Co-Mn-α-Fe_2O_3 photoanode under AM 1.5 G illumination at 1.23 V vs. RHE.

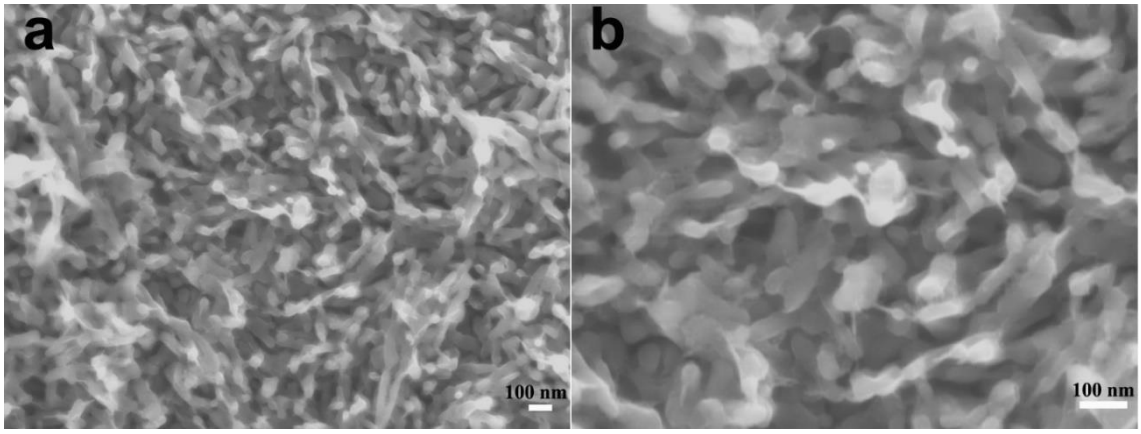

Figure 2.16 SEM images of the Co-Mn-α-Fe_2O_3 films after stability test with different magnification.

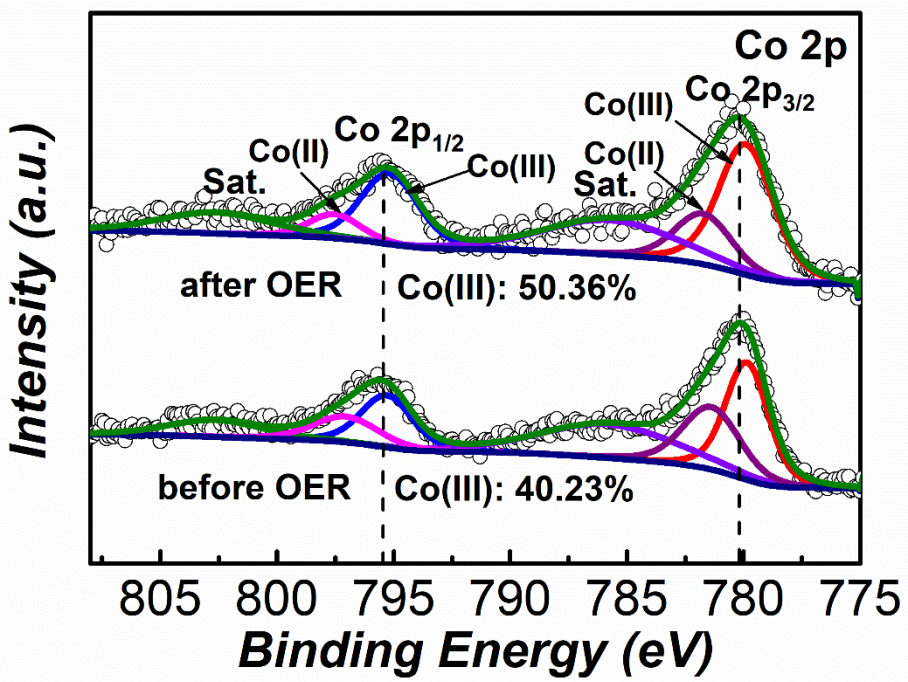

Figure 2.17 Co 2p XPS spectra of Co-Mn-α-Fe_2O_3 before and after stability test.

Table 2.1 Comparison of our photoanode to other α-Fe_2O_3-based photoanodes in recent years.

Photoanodes	Onset Potential (V) vs. RHE	Current Density at 1.23 V vs. RHE (mA cm^{-2})	Stability	IPCE Value (%)
NiO-P-α-Fe_2O_3[50]	0.69	2.08	~5% decay after 10 h	38.6 at 1.23V (350 nm)
Zr-α-Fe_2O_3 NT[51]	~0.89	1.50	No decay after 5 h	25.7 at 1.23V (370 nm)
Rh-F-Fe_2TiO_5/ α-Fe_2O_3[52]	0.63	2.12	N.A.	37 at 1.25V (370 nm)
carbon coated α-Fe_2O_3[53]	0.77	2.00	N.A.	N.A.
Co-Pi-α-Fe_2O_3[54]	~0.8	1.28	N.A.	N.A.
IrO_2/RuO_2-α-Fe_2O_3[55]	0.48	1.52	No decay after 72 h	54 at 1.25V (330 nm)
α-Fe_2O_3/ FeOOH/Au[56]	0.6	3.2	N.A.	80 at 1.23 V (390 nm)
Co/E-I-Sn-α-Fe_2O_3[57]	~0.6	2.2	~4% decay after 10 h	27 at 1.23V (330 nm)
Au-embedded α-Fe_2O_3[58]	0.8	1.025	No decay after 1.5 h	16 at 1.23V (410 nm)

P:α-Fe_2O_3/CoPi[59]	0.58	2.0	11% decay after 5 h	28 at 1.23V (360 nm)
α-Fe_2O_3/CoAl LDH[60]	0.58	2.0	No decay after 2 h	N.A.
α-Fe_2O_3/FeOOH[61]	~0.8	0.85	4.4% decay after 70 h	20.2 at 1.23 V (400 nm)
α-Fe_2O_3/FeOOH[62]	0.65	1.21	~3% decay after 2.5 h	N.A.
Co-Mn-α-Fe_2O_3	**0.6**	**2.09**	**~ 3% decay after 10 h**	**39.1 at 1.23 V (360 nm)**

2.3.4 Research on catalytic mechanism

To understand the underlying mechanism of Co-Mn nanosheets for enhancing PEC performance of α-Fe_2O_3 films, charge transfer behaviors of the photoanodes were investigated by electrochemical measurements. Due to the low activation energy and kinetically facile photo-oxidation of SO_3^{2-} species, *J*−*V* curves of the photoanodes were measured with Na_2SO_3 as hole scavenger (Figure 2.18a).[28] Then, the surface charge injection efficiency (η_{inj}) and charge separation efficiency (η_{sep}) were calculated according to the equations in experimental section and the J_{abs} in Figure 2.18b. As shown in Figure 2.19a and Figure 2.19b, the η_{inj} and η_{sep} values of Co-Mn-α-Fe_2O_3 photoanode are both much higher than that of pure α-Fe_2O_3 photoanode, while Mn-α-Fe_2O_3 and Co-α-Fe_2O_3 photoanodes only exhibit moderate values. These results are consistent with the PEC performance test, demonstrating that the positive outcomes could not only be ascribed to the improved water oxidation kinetics, but also the reduced surface charge recombination due to the electron-donating effect within Co-Mn nanosheets.

To gain more insight into the impacts of Co-Mn nanosheets modification to charge transfer and separation processes, Mott–Schottky analysis was conducted (Figure 2.19c). It is clearly presented that all photoanodes exhibit positive slopes, manifesting n-type semiconductor feature. The flat-band potentials display a gradually cathodic shift from bare α-Fe_2O_3 to Co-Mn-α-Fe_2O_3 photoanode and the slopes of Mott–Schottky curves show an evident decrease after OECs loading. The values of carrier density (N_d), which derives from the slope of Mott-Schottky curves, promote from 1.34×10^{20} cm^{-3} to 5.41×10^{20} cm^{-3} (Table 2.2). The enhancement of N_d could promote band bending at the interface of electrode/electrolyte, facilitating the processes of charge transfer.[45] In this case, the results of Mott–Schottky analysis are consistent with PEC Na_2SO_3 oxidation

test, verifying more effective processes of charge separation and holes injection with decoration of Co-Mn nanosheets.

To visualize the charge transfer processes at the interface of electrode/electrolyte, electrochemical impedance spectroscopy (EIS) was measured at 1.23 V vs. RHE under illumination. As demonstrated in Figure 2.19d, all the Nyquist plots of four photoanodes show two obvious semicircles. The small semicircle in high-frequency range is usually regarded as charge transfer process in the bulk of semiconductor, while the large semicircle of low-frequency region is deemed as charge transfer behavior at electrode/electrolyte interface. Both of the semicircles are smaller for the OECs loaded photoanodes, indicating a faster surface water oxidation process benefited by efficient hole extraction and oxidization catalytic capability.[46] In order to investigate the EIS data more thoroughly, a typical equivalent circuit model inserted in Figure 5d is proposed and the fitted results are presented with solid lines. In this case, R_s indicates the series resistance, representing the resistivity of electrolyte between working and reference electrodes, R_{bulk} in high frequency represents resistance in the semiconductor, R_{ct} in low frequency defines as charge transfer resistance across the interface of photoanode/electrolyte and CPE is the constant phase element.[28, 46] The values of all these items are displayed in Table 2.3, in which R_s for all photoanodes are almost same, suggesting similar working condition of these photoanodes. Furthermore, the values of R_{bulk} for photoanodes of Mn-α-Fe_2O_3 (60.77 Ω), Co-α-Fe_2O_3 (38.41 Ω) and Co-Mn-α-Fe_2O_3 (28.19 Ω) are all lower than that of pristine α-Fe_2O_3 (103.7 Ω), demonstrating enhanced conductivity ascribing to the incorporation of OECs. The improved charge transfer in the bulk might be attributed to the facilitated charge separation, indicating the OECs have additional effects on promoting the PEC water oxidation in addition to the surface catalytic effect.[17] A significant decrease can be observed in R_{ct} from 564.9 Ω to 299.7 Ω after the decoration of Co-Mn nanosheets, proposing that the photogenerated charge carriers could be injected into electrolyte more easily on Co-Mn-α-Fe_2O_3 photoanode.

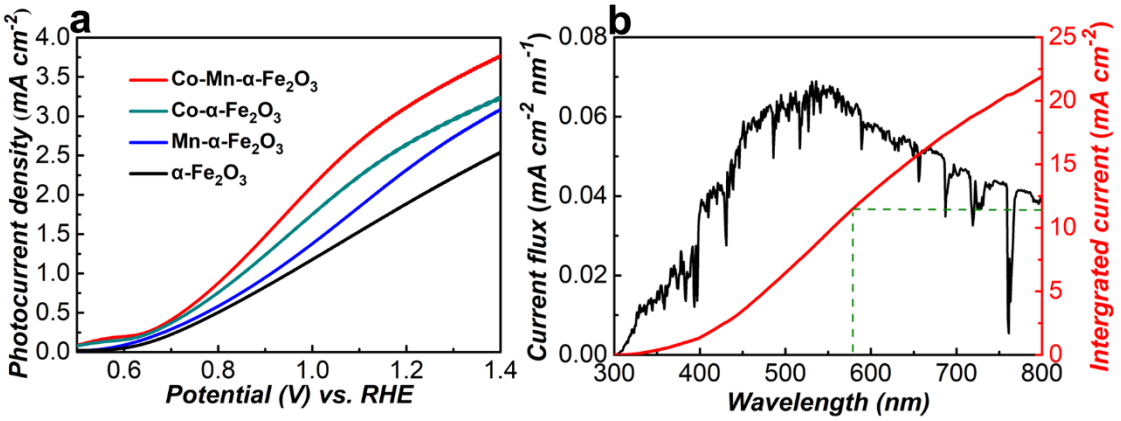

Figure 2.18 a) *J–V* curves of pristine α-Fe_2O_3, Mn-α-Fe_2O_3, Co-α-Fe_2O_3 and Co-Mn-α-Fe_2O_3 photoanodes with Na_2SO_3 as the hole scavenger; b) The calculated current density flux and integrated current density (J_{abs}) of Co-Mn-α-Fe_2O_3 photoanode.

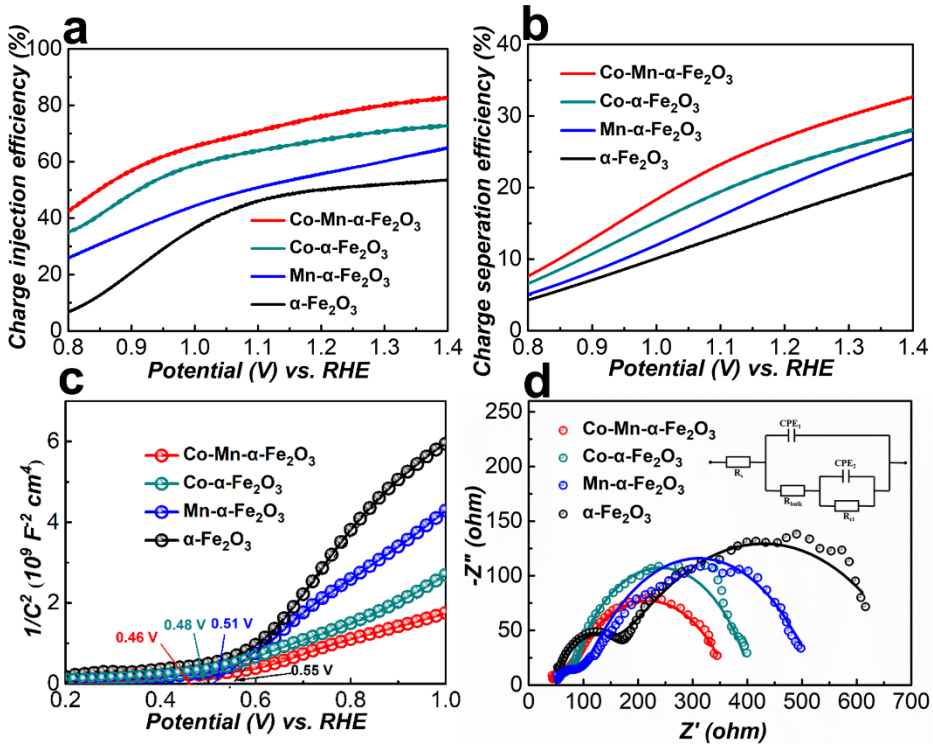

Figure 2.19 a) Charge injection efficiencies on the surface, b) charge separation efficiencies in the bulk, c) Mott–Schottky plots and d) EIS plots and fitting-figures (solid lines) of pristine α-Fe_2O_3, Mn-α-Fe_2O_3, Co-α-Fe_2O_3 and Co-Mn-α-Fe_2O_3 photoanodes.

Table 2.2 E_{fb} values and carrier densities obtained from Mott-Schottky plots for pristine α-Fe_2O_3, Mn-α-Fe_2O_3, Co-α-Fe_2O_3 and Co-Mn-α-Fe_2O_3 photoanodes.

Photoanode	E_{fb} (V) vs. RHE	Carrier Density (cm^{-3})
α-Fe_2O_3	0.55	1.34×10^{20}
Mn-α-Fe_2O_3	0.51	2.01×10^{20}
Co-α-Fe_2O_3	0.48	3.40×10^{20}
Co-Mn-α-Fe_2O_3	0.46	5.41×10^{20}

Table 2.3 EIS results of different photoanodes calculated by the equivalent circuit model.

Photoanode	R_s (Ω)	R_{bulk} (Ω)	R_{ct} (Ω)
α-Fe_2O_3	49.78	103.7	564.9
Mn-α-Fe_2O_3	49.91	60.77	414.9
Co-α-Fe_2O_3	47.87	38.41	323.2
Co-Mn-α-Fe_2O_3	41.39	28.19	299.7

Based on above discussion, the proposed electron transfer paths for Co-Mn-α-Fe_2O_3 photoanode are schematically illustrated in Figure 2.20. Under illumination, α-Fe_2O_3 can generate electrons and holes. Then the photo-generated electrons will migrate to FTO substrate, while the holes transfer to the surface driven by electric filed. The surface-reaching holes are inclined to accumulate and recombine with the electrons due to sluggish kinetics of water oxidation and intrinsic properties of α-Fe_2O_3. However, with the modification of Co-Mn nanosheets, photo-generated holes will migrate to the OEC layer and the recombination of charge carriers will be restricted. Co ions act as active sites to receive holes from semiconductor and then be oxidized to various high-value states.[47] The oxidation state of Co ions with high values (Co^{3+} or Co^{4+}) will then deliver the positive charge to the coordinated intermediate species to generate O_2 and recover to the initial states.[48] The electrons can migrate from Mn site to Co site via the intimate interface, indicating that chemical states of Co will become lower (the Co^{2+} and Co^{3+} will be changed to $Co^{2-\sigma}$ and $Co^{3-\sigma}$). Consequently, the active sites of Co are inclined to accept the holes more easily, which is consistent with the high surface charge injection efficiency. The greater number of electrons in Co sites could also facilitate the generation of absorbed OOH intermediates and thus accelerate the O_2 production.[40, 49]

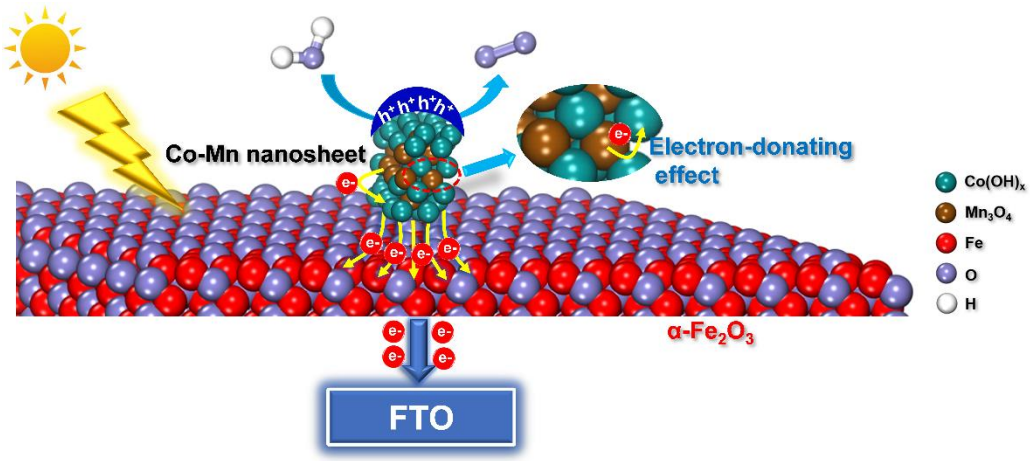

Figure 2.20 Schematic electron transfer paths presumedly occur in Co-Mn-α-Fe_2O_3 photoanode under AM 1.5 G illumination responsible for the PEC water oxidation.

Since Co-Mn nanosheets could achieve superior OER activity, we further investigated whether other composites (such as Ni-Mn composite and Fe-Mn composite) had similar enhancement effects on α-Fe_2O_3. As shown in Figure 2.21, the morphologies of Ni-Mn-α-Fe_2O_3 and Fe-Mn-α-Fe_2O_3 are similar with Co-Mn-α-Fe_2O_3, with a thin layer coating on the surface of α-Fe_2O_3 nanorods. *J*–*V* curves presented in Figure 2.22 demonstrate that Ni-Mn composite and Fe-Mn composite could also enhance the OER performance of α-Fe_2O_3 films, suggesting the versatility of our strategy.

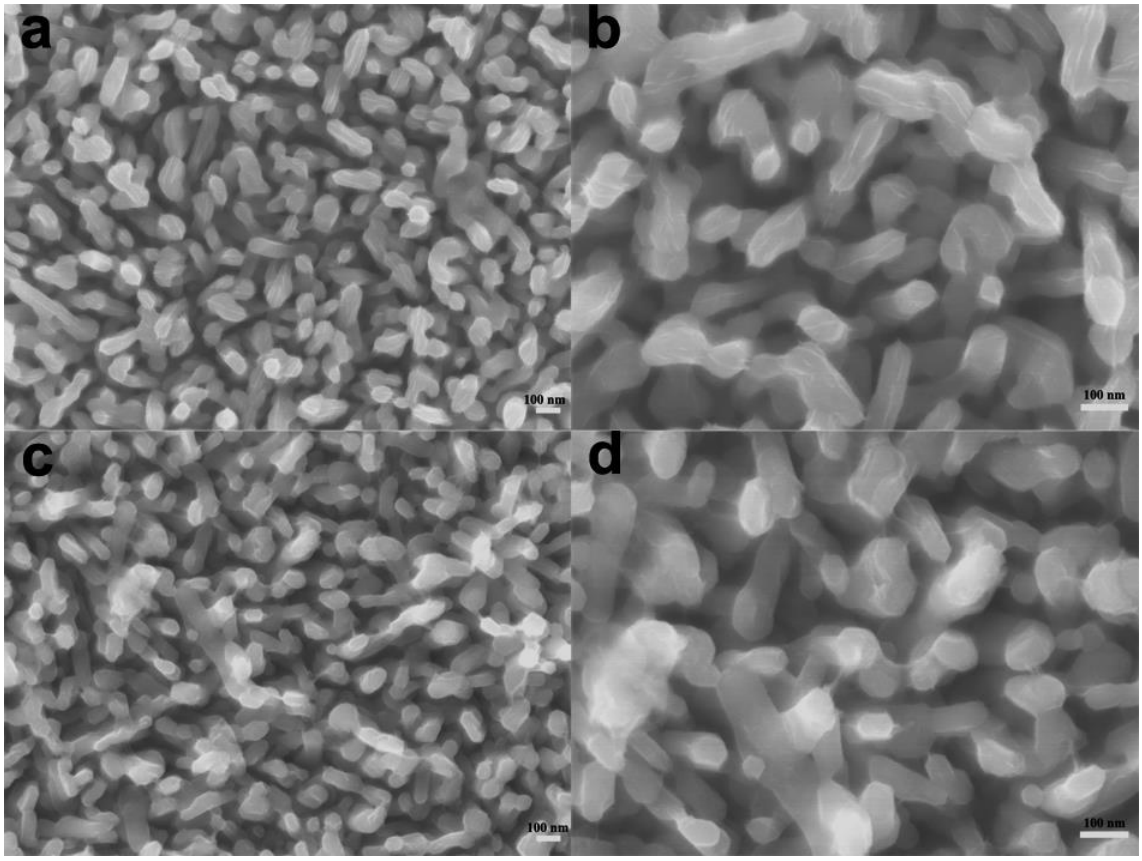

Figure 2.21 SEM images of (a, b) Ni-Mn-α-Fe_2O_3 and (c, d) Fe-Mn-α-Fe_2O_3 films.

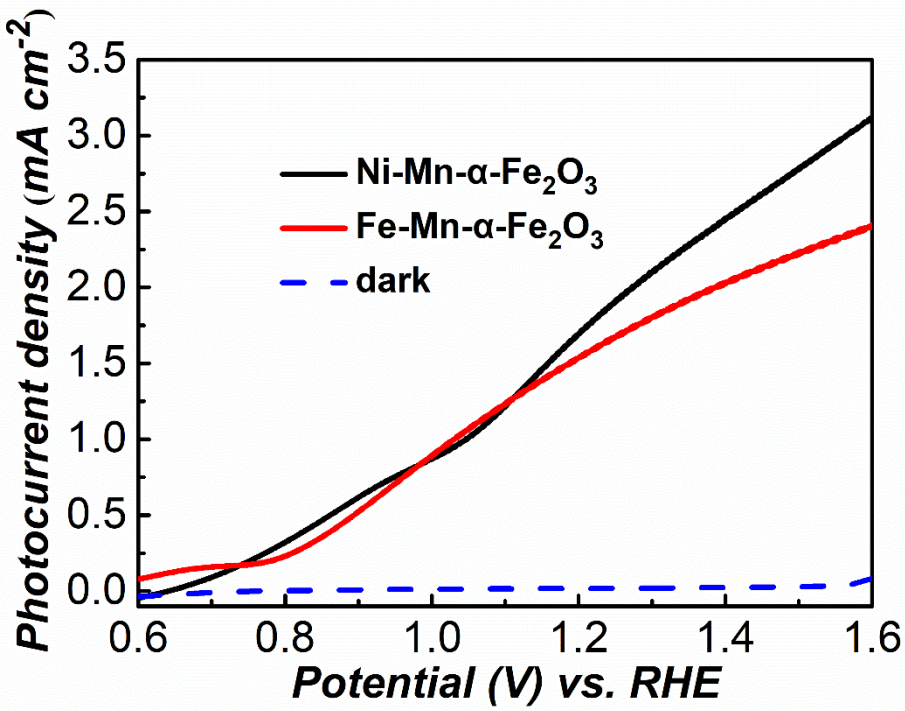

Figure 2.22 *J–V* curves of Ni-Mn-α-Fe_2O_3 and Fe-Mn-α-Fe_2O_3 films.

2.4 Conclusions

In conclusion, we have constructed ultrathin Co-Mn nanosheets as OEC for α-Fe_2O_3 films and investigated the electron-withdrawing/donating effect between $Co(OH)_x$ and Mn_3O_4 to enhance the activity of photoanodes for PEC water oxidation. This approach helps in attaining an advantageous OEC/semiconductor interface to reduce recombination of photogenerated charge carries and enhance their transfer efficiency. Compared with bare α-Fe_2O_3 photoanode, the optimized photoanode exhibits a remarkable photocurrent density of 2.09 mA cm^{-2} at 1.23 V vs. RHE under AM 1.5 G illumination and an impressive cathodic shift (~ 200 mV) of onset potential. Furthermore, Co-Mn nanosheets can also significantly enhance the ABPE values of α-Fe_2O_3 even at a lower potential and provide a remarkable resistance against photo-corrosion with an excellent stability for over 10 h. Detailed mechanism investigation unveils the pivotal role of electron-donation effect from Mn_3O_4 to $Co(OH)_x$ resulting in efficient charge injection processes and thus dramatically enhanced PEC water oxidation performance. Our work provides deep understanding on the electron-withdrawing/donating effect for catalytic materials with multi-metallic sites, which possesses huge potentials in solving the current dilemma for large-scale applications of PEC water splitting.

References

[1] M. G. Walter, E. L. Warren, J. R. McKone, S. W. Boettcher, Q. Mi, E. A. Santori, N. S. Lewis, *Chem. Rev.* **2010**, *110*, 6446.

[2] M. Grätzel, *Nature* **2001**, *414*, 338.

[3] T. Hisatomi, J. Kubota, K. Domen, *Chem. Soc. Rev.* **2014**, *43*, 7520.

[4] S. Kment, F. Riboni, S. Pausova, L. Wang, L. Wang, H. Han, Z. Hubicka, J. Krysa, P. Schmuki, R. Zboril, *Chem. Soc. Rev.* **2017**, *46*, 3716.

[5] J. R. Swierk, T. E. Mallouk, *Chem. Soc. Rev.* **2013**, *42*, 2357.

[6] K. Sivula, F. Le Formal, M. Grätzel, *ChemSusChem* **2011**, *4*, 432.

[7] Y. Lin, G. Yuan, S. Sheehan, S. Zhou, D. Wang, *Energy Environ. Sci.* **2011**, *4*, 4862.

[8] A. Kay, I. Cesar, M. Grätzel, *J. Am. Chem. Soc.* **2006**, *128*, 15714.

[9] P. Peerakiatkhajohn, J. H. Yun, H. Chen, M. Lyu, T. Butburee, L. Wang, *Adv. Mater.* **2016**, *28*, 6405.

[10] Z. Luo, T. Wang, J. Zhang, C. Li, H. Li, J. Gong, *Angew. Chem. Int. Ed.* **2017**, *56*, 12878.

[11] Y. Ling, G. Wang, D. A. Wheeler, J. Z. Zhang, Y. Li, *Nano Lett.* **2011**, *11*, 2119.

[12] I. Cesar, A. Kay, J. A. Gonzalez Martinez, M. Grätzel, *J. Am. Chem. Soc.* **2006**, *128*, 4582.

[13] N. Mirbagheri, D. Wang, C. Peng, J. Wang, Q. Huang, C. Fan, E. E. Ferapontova, *ACS Catal.* **2014**, *4*, 2006.

[14] M. T. Mayer, Y. Lin, G. Yuan, D. Wang, *Acc. Chem. Res.* **2013**, *46*, 1558.

[15] Q. Liu, J. He, T. Yao, Z. Sun, W. Cheng, S. He, Y. Xie, Y. Peng, H. Cheng, Y. Sun, *Nat. Commun.* **2014**, *5*, 5122.

[16] L. Wang, N. T. Nguyen, X. Huang, P. Schmuki, Y. Bi, *Adv. Funct. Mater.* **2017**, *27*, 1703527.

[17] Y. F. Xu, X. D. Wang, H. Y. Chen, D. B. Kuang, C. Y. Su, *Adv. Funct. Mater.* **2016**, *26*, 4414.

[18] D. K. Zhong, M. Cornuz, K. Sivula, M. Grätzel, D. R. Gamelin, *Energy Environ. Sci.* **2011**, *4*, 1759.

[19] Q. Yu, X. Meng, T. Wang, P. Li, J. Ye, *Adv. Funct. Mater.* **2015**, *25*, 2686.

[20] C. G. Morales-Guio, M. T. Mayer, A. Yella, S. D. Tilley, M. Grätzel, X. Hu, *J. Am. Chem. Soc.* **2015**, *137*, 9927.

[21] J. Yang, D. Wang, H. Han, C. Li, *Acc. Chem. Res.* **2013**, *46*, 1900.

[22] Q. Rui, L. Wang, Y. Zhang, C. Feng, B. Zhang, S. Fu, H. Guo, H. Hu, Y. Bi, *J. Mater. Chem. A* **2018**, *6*, 7021.

[23] C. Ding, J. Shi, Z. Wang, C. Li, *ACS Catal.* **2016**, *7*, 675.

[24] M. P. Suryawanshi, U. V. Ghorpade, S. W. Shin, U. P. Suryawanshi, H. J. Shim, S. H. Kang, J. H. Kim, *Small* **2018**, *14*, 1801226.

[25] W. Liu, H. Liu, L. Dang, H. Zhang, X. Wu, B. Yang, Z. Li, X. Zhang, L. Lei, S. Jin, *Adv. Funct. Mater.* **2017**, *27*, 1603904.

[26] G. Wang, B. Wang, C. Su, D. Li, L. Zhang, R. Chong, Z. Chang, *J. Catal.* **2018**, *359*, 287.

[27] J. S. Kim, B. Kim, H. Kim, K. Kang, *Adv. Energy Mater.* **2018**, *8*.

[28] F. Li, J. Li, J. Zhang, L. Gao, X. Long, Y. Hu, S. Li, J. Jin, J. Ma, *ChemSusChem* **2018**, *11*, 2156.

[29] Z. Yan, H. Sun, X. Chen, H. Liu, Y. Zhao, H. Li, W. Xie, F. Cheng, J. Chen, *Nat. Commun.* **2018**, *9*, 2373.

[30] N. Li, Y. Tian, J. Zhao, J. Zhang, J. Zhang, W. Zuo, Y. Ding, *Appl. Catal. B: Environ.* **2017**, *214*, 126.

[31] J. X. Feng, H. Xu, Y. T. Dong, S. H. Ye, Y. X. Tong, G. R. Li, *Angew. Chem. Int. Ed.* **2016**, *128*, 3758.

[32] S. Wang, T. He, J. H. Yun, Y. Hu, M. Xiao, A. Du, L. Wang, *Adv. Funct. Mater.* **2018**, *28*, 1802685.

[33] Y. Liang, H. Wang, J. Zhou, Y. Li, J. Wang, T. Regier, H. Dai, *J. Am. Chem. Soc.* **2012**, *134*, 3517.

[34] R. Nie, J. Shi, W. Du, W. Ning, Z. Hou, F.-S. Xiao, *J. Mater. Chem. A* **2013**, *1*, 9037.

[35] H. Kim, J. Park, I. Park, K. Jin, S. E. Jerng, S. H. Kim, K. T. Nam, K. Kang, *Nat. Commun.* **2015**, *6*, 8253.

[36] M.-R. Gao, Y.-F. Xu, J. Jiang, Y.-R. Zheng, S.-H. Yu, *J. Am. Chem. Soc.* **2012**, *134*, 2930.

[37] B. S. Yeo, A. T. Bell, *J. Am. Chem. Soc.* **2011**, *133*, 5587.

[38] A. Grimaud, K. J. May, C. E. Carlton, Y.-L. Lee, M. Risch, W. T. Hong, J. Zhou, Y. Shao-Horn, *Nat. Commun.* **2013**, *4*, 2439.

[39] S. Zhao, R. Jin, H. Abroshan, C. Zeng, H. Zhang, S. D. House, E. Gottlieb, H. J. Kim, J. C. Yang, R. Jin, *J. Am. Chem. Soc.* **2017**, *139*, 1077.

[40] T. Tang, W.-J. Jiang, S. Niu, N. Liu, H. Luo, Y.-Y. Chen, S.-F. Jin, F. Gao, L.-J. Wan, J.-S. Hu, *J. Am. Chem. Soc.* **2017**, *139*, 8320.

[41] E. Kecsenovity, B. z. Endrődi, P. t. S. Tóth, Y. Zou, R. A. Dryfe, K. Rajeshwar, C. Janáky, *J. Am. Chem. Soc.* **2017**, *139*, 6682.

[42] J. Zhang, R. García-Rodríguez, P. Cameron, S. Eslava, *Energy Environ. Sci.* **2018**, *11*, 2972.

[43] X. Cheng, S. Cao, Y. Huan, Z. Bai, M. Li, H. Wu, R. Zhang, W. Peng, Z. Ji, X. Yan, *Energy Technol.* **2019**, *7*, 1800899.

[44] K. Zhang, B. Jin, C. Park, Y. Cho, X. Song, X. Shi, S. Zhang, W. Kim, H. Zeng, J. H. Park, *Nat. Commun.* **2019**, *10*, 2001.

[45] F. A. Laskowski, M. R. Nellist, J. Qiu, S. W. Boettcher, *J. Am. Chem. Soc.* **2019**, *141*, 1394.

[46] G. Liu, P. Li, G. Zhao, X. Wang, J. Kong, H. Liu, H. Zhang, K. Chang, X. Meng, T. Kako, *J. Am. Chem. Soc.* **2016**, *138*, 9128.

[47] D. K. Zhong, D. R. Gamelin, *J. Am. Chem. Soc.* **2010**, *132*, 4202.

[48] A. Indra, P. W. Menezes, N. R. Sahraie, A. Bergmann, C. Das, M. Tallarida, D. Schmeißer, P. Strasser, M. Driess, *J. Am. Chem. Soc.* **2014**, *136*, 17530.

[49] D. Zhao, Y. Pi, Q. Shao, Y. Feng, Y. Zhang, X. Huang, *ACS Nano* **2018**, *12*, 6245.

[50] F. Li, J. Li, J. Zhang, L. Gao, X. Long, Y. Hu, S. Li, J. Jin, J. Ma, *ChemSusChem* **2018**, *11*, 2156.

[51] C. Li, A. Li, Z. Luo, J. Zhang, X. Chang, Z. Huang, T. Wang, J. Gong, *Angew. Chem. Int. Ed.* **2017**, *56*, 4150.

[52] J. Deng, X. Lv, K. Nie, X. Lv, X. Sun, J. Zhong, *ACS Catal.* **2017**, *7*, 4062.

[53] T. H. Wang, C.-C. Chiang, Y.-L. Wu, C. Lin, Y.-J. Cheng, Y.-K. Hsieh, C.-F. Wang, C. Huang, *Appl.Catal. B: Environ.* **2017**, *207*, 1.

[54] J. Xiao, H. Huang, Q. Huang, L. Zhao, X. Li, X. Hou, H. Chen, Y. Li, *J. Catal.* **2017**, *350*, 48.

[55] P. Dias, L. Andrade, A. Mendes, *Nano Energy* **2017**, *38*, 218.

[56] L. Wang, H. Hu, N. T. Nguyen, Y. Zhang, P. Schmuki, Y. Bi, *Nano Energy* **2017**, *35*, 171.

[57] M. Li, Y. Yang, Y. Ling, W. Qiu, F. Wang, T. Liu, Y. Song, X. Liu, P. Fang, Y. Tong, *Nano Lett.* **2017**, *17*, 2490.

[58] P. S. Shinde, S. Y. Lee, J. Ryu, S. H. Choi, J. S. Jang, *Chem. Commun.* **2017**, *53*, 4278.

[59] Z. Luo, C. Li, S. Liu, T. Wang, J. Gong, *Chem. Sci.* **2017**, *8*, 91.

[60] R. Chong, B. Wang, C. Su, D. Li, L. Mao, Z. Chang, L. Zhang, *J. Mater. Chem. A* **2017**, *5*, 8583.

[61] Q. Yu, X. Meng, T. Wang, P. Li, J. Ye, *Adv. Funct. Mater.* **2015**, *25*, 2686.

[62] J. Y. Kim, D. H. Youn, K. Kang, J. S. Lee, *Angew. Chem. Int. Ed.* **2016**, *55*, 10854.

Chapter 3 A universal strategy boosting photoelectrochemical water oxidation by utilizing MXene nanosheets as hole transfer mediators

3.1 Introduction

PEC water splitting has been projected as a promising approach to meet the steadily growing demand for cleaner and renewable energy.[1-3] Due to the complex processes of four-electron transfer, the oxygen evolution reaction (OER) is more difficult than the two-electron hydrogen evolution reaction (HER).[4-5] Then the sluggish OER on the photoanode becomes the rate-limiting step that governs the reaction rate of the PEC water splitting.[6-7] Therefore, enhancing the water oxidation should be strived for to rule over the practical application of PEC water splitting.[8-9]

Notably, loading oxygen evolution catalysts (OECs), such as transition metal oxides and hydroxides, is one of the most effective strategy to enhance the surface reaction kinetics of photoanodes.[10-11] The function of OECs is providing reaction sites for the holes transferred to the interface of photoelectrode/electrolyte, namely suppressing the charge recombination on the surface and lowering the overpotentials for water oxidation.[12] However, even though with the introduction of OECs, the PEC water oxidation efficiency still remains challenging to reach the required level due to the inefficient charge transfer through the interface of semiconductor and OEC, which may be resulted from the mismatch of crystal lattice or energy band level between the semiconductor and OEC.[13-14] Thus the catalytic capability of OEC is strongly limited by the weak thermodynamic driving force rooted in the low charge transfer efficiency from the semiconductors.[15-16] This limitation signifies that the charge modulation should be optimized at the semiconductor/OEC interface, which can boost the separation of photogenerated charge by injecting the charge carriers into the OEC. Therefore, a ternary structure on the photoanodes with an interlayer introduced between the semiconductor and OEC was developed.[16-17] Until now, several kinds of interlayers, such as hole storage layers,[14] passivation layers[18] and metal layers,[19] have been designed to work cooperatively with the OECs and displayed great potential to achieve efficient PEC water oxidation. However, several important issues for this ternary structure still remain and need to be conquered: i) the enhanced activity in most reported cases is attributed to the

superposed effects of interlayers and OECs, rather than the facilitated charge transfer at the semiconductor/OEC interface; ii) the performance of the modified photoanodes is still moderate and novel interfacial charge mediators should be further developed; iii) a universal strategy that is applicable to various photoanodes is rarely reported and remains challenging. Therefore, exploiting a suitable interfacial mediator, which should also be adaptive with the semiconductor and the OECs in both the energy level and structural properties,[13] is significantly important to construct an efficient charge modulation system for PEC water oxidation.

As a novel two-dimensional (2D) structure materials, MXene has shown great potential in the fields of energy storage and catalysis, owing to the unique architecture with metallic electrical conductivity, high specific surface area and hydrophilic surface property.[20-21] Additionally, the tunable work function affected by the surface-functional groups can adjust the interfacial barrier height of the junctions, which can effectively accelerate the carrier extraction, combining with the high carrier mobility.[22-23] Therefore, employing MXene and its tailored integration with photoanodes is attractive and practical to enhance the PEC water oxidation. However, it is rarely reported to utilize MXene in the PEC water oxidation, not even functioning as the interfacial mediator. One possible reason could be that MXene flakes are readily oxidized in aqueous environments, leading to deteriorated electrical properties, which then limiting their applications involving exposure to an oxygen-containing aqueous environment and long-term operation.[24-25] Thus, an optimized structure of the photoanode should be designed to retard the oxidation process of MXene under the harsh PEC test condition.

In this study, hematite (α-Fe_2O_3) was chosen as a prototype owing to its low cost, suitable band structure but poor optoelectronic properties. Then a novel interfacial charge modulation system was designed with the insertion of ultrathin MXene nanosheets (MNs) as hole transfer mediators between α-Fe_2O_3 nanorods and conventional OEC layers (Co-Pi). The electrochemical analysis reveals a strong built-in electric field formed at the MNs/α-Fe_2O_3 Schottky junction with a larger extracted photovoltage, resulting in a reduced recombination during the charge separation and transfer process. After decorating with the thin layer of Co-Pi, photogenerated holes can be smoothly driven from the α-Fe_2O_3 to the Co-Pi sites, achieving an efficient water oxidation. As a result, the optimized Co-Pi/MNs/α-Fe_2O_3 photoanode delivers a photocurrent density of 3.20 mA cm^{-2} at 1.23 V vs. RHE, as well as an impressive cathodic onset potential shift of

~250 mV compared with the bare α-Fe_2O_3. The "sandwich" structure of Co-Pi/MNs/α-Fe_2O_3 can also protect the MNs from direct exposure to the electrolyte, hence achieving a remarkable stability for 20 h. Interestingly, this strategy can be also extended to other OECs (NiOOH and FeOOH) and semiconductors ($BiVO_4$, WO_3 and ZnO), which is believed to be a versatile and promising strategy to enhance the PEC water oxidation by interfacial charge modulation.

3.2 Experimental section

3.2.1 Materials preparation

Preparation of α-Fe_2O_3 films: α-Fe_2O_3 films were prepared according to the previous report.[6] Briefly, 0.15 M of $FeCl_3$ and 1 M $NaNO_3$ were dissolved in 40 ml water with the pH adjusted to 1.50 by HCl. The aqueous solution was transferred to a Teflon-lined stainless steel autoclave. Then the fluorine-doped tin oxide (FTO) glasses, which were ultrasonically cleaned with ethanol, acetone and deionized water sequentially for 1h to remove the organic contamination and dust, were immersed and placed with the conductive side facing to the wall of the autoclave. The autoclave was then put into the oven and heated at 95 ^oC for 4 h. A uniform layer of FeOOH (yellow color) was deposited on the FTO glasses. The substrates were washed with deionized water to remove the residual FeOOH and subsequently calcinated at 550 °C for 2 h and 800 °C for additional 20 min.

Synthesis of MXene nanosheets (MNs): Multilayer $Ti_3C_2T_x$ was prepared by selective etching the Al layer from MAX (Ti_3AlC_2).[12] Specifically, 1 g of Ti_3AlC_2 was added into 10 mL HF solution (40 wt%) and magnetically stirred for 18 h at room temperature (RT). Then the obtained solution was washed with deionized water repeatedly until the pH was above 6. To obtain few- and/or single-layer flakes, the obtained MXene ($Ti_3C_2T_x$) was delaminated in 20 mL tetramethylammonium hydroxide (TMAOH) for 18 h at RT. After diluted with deionized water, TMAOH-intercalated $Ti_3C_2T_x$ was separated by centrifugation at 5000 rpm for 3 min. The obtained precipitate was dispersed in deionized water with a weight ratio of $Ti_3C_2T_x$: water of 1:300. The suspension was sonicated under flowing nitrogen (N_2) for 2 h, and then centrifuged at 3000 rpm for 1 h to obtain the supernatant containing delaminated MXene flakes. Then the delaminated MXene flakes were downsized into small pieces of MNs with strong sonication treatment

Fabrication of MNs/α-Fe_2O_3 and Co-Pi/MNs/α-Fe_2O_3 photoelectrodes: The obtained MNs solution was decorated onto the surface of α-Fe_2O_3 films with spin-coating method. Then the MNs/α-Fe_2O_3 films were then annealed at 150 ^oC in tube furnace under argon atmosphere for 1h to reinforce the interaction between MNs and α-Fe_2O_3. Then the Co-Pi layers were photoelectrodeposited onto the MNs/α-Fe_2O_3 photoanode by a solution of 0.5 mM $Co(NO_3)_2 \cdot 6H_2O$ in 0.1 M potassium phosphate buffer (pH=6.9) at 0.2 V vs. Ag/AgCl for 100 s under AM 1.5G illumination.

3.2.2 Material characterization

In our investigation, X-ray diffraction (XRD) patterns were measured on an X-ray diffractometer (X'pert powder, PANalytical B.V.) with Copper-Kα radiation under 40 kV and 30 mA. Optical absorption properties of the photoelectrodes were measured over an ultraviolet–visible (UV–vis) spectrophotometer (UV-2700, Shimadzu). The morphologies of the films were characterized by scanning electron microscopy (SEM) (S-4800, Hitachi) and transmission electron microscopy (TEM) (FEI Tecnai G2 F30), coupled with energy dispersive spectrometer (EDS) to determine elementary composition. X-ray photoelectron spectroscopy (XPS) (PHI Quantera SXM, ULVAC-PHI) experiments were performed in a Theta probe using monochromated Mg Kα x-rays at hν = 1486.6 eV. Peak positions were internally referenced to the C 1s peak at 284.8 eV. Raman spectra were collected using a Horiba Jobin Yvon LabRAM system with a 532 nm excitation laser.

3.2.3 Photoelectrochemical measurement

The PEC characterization was carried out using three-electrode cell system, in which a piece of pure platinum and an Ag/AgCl (3 M KCl) electrode as counter and reference electrodes, respectively. 1M NaOH aqueous solution was used as electrolyte (pH=13.6). The available electrode area immersed in the electrolyte solution was fixed to 1.0×1.0 cm^2. AM 1.5 G solar simulation (WXS-80C-3 AM 1.5 G) with a light intensity of 100 mW cm^{-2} was utilized as the light sources. Photocurrent–potential (*J*–*V*) curves were obtained using linear sweep voltammogram in a voltage window of 0.6~1.6 V vs. RHE with a scan rate of 20 mV s^{-1} on an electrochemical workstation (ALS/CH model 650A) and the light was chopped manually at regular intervals. Electrochemical impedance spectroscopy (EIS) test was performed at a DC bias of 1.23 V vs. RHE under AM 1.5 G

illumination (frequency range: 0.1~100000 Hz). All the potentials in the PEC performance vs. Ag/AgCl could be converted to the RHE scale using the equation below.

$$E_{RHE}=E_{Ag/AgCl}+0.059\times pH+E^{0}_{Ag/AgCl} \quad (1)$$

Where E_{RHE} is the converted potential vs. RHE. $E_{Ag/AgCl}$ represents the experimental result vs. Ag/AgCl and $E^{0}_{Ag/AgCl}$ is 0.197 V at ambient temperature of 25 °C.

Applied bias photon-to-current efficiency (ABPE) was calculated using the equation below.

$$ABPE\ (\%) = \frac{J\times(1.23-V_b)}{P_{light}}\times 100\% \quad (2)$$

where J refers to the photocurrent density (mA cm^{-2}) obtained from the electrochemical workstation. V_b represents the applied bias vs. RHE (V), and P_{light} is the total light intensity of AM 1.5 G (100 mW cm^{-2}).

Incident photon to electron conversion efficiency (IPCE) was measured using a motorized monochromator (M10; Jasco Corp.), which was calculated using the following equation.

$$IPCE\ (\%) = \frac{J\times 1240}{\lambda\times P_{light}}\times 100\% \quad (3)$$

where J is the photocurrent density (mA cm^{-2}) obtained from the electrochemical workstation. λ and P_{light} refer to the incident light wavelength (nm) and the power density obtained at a specific wavelength (mW cm^{-2}), respectively.

For comparison of charge recombination rate at the photoanode/electrolyte junction, the carrier lifetime was quantified by:

$$\tau_n = \frac{\kappa_B T}{e}\left(\frac{dOCP}{dt}\right)^{-1} \quad (4)$$

where τ_n, κ_B, T, e, and dOCP/dt are the carrier lifetime, Boltzmann's constant, temperature (K), charge of single electron and derivative of the OCP transient decay, respectively.

The water oxidation photocurrent density could be calculated by the following formula,

$$J_{PEC} = J_{abs}\times\eta_{sep}\times\eta_{inj} \quad (5)$$

J_{abs} is the photocurrent density when the absorbed photon completely converting into current. As a hole scavenger, Na_2SO_3 can effectively trap the holes that arrived to the surface, without influencing the charge separation on the electrode (η_{inj} assumed to be

100%). Therefore, the charge separation efficiency in the bulk (η_{sep}) and surface charge injection efficiency (η_{inj}) could be deduced with following equations.

$$\eta_{\mathrm{sep}} = \frac{J^{Na_2SO_3}}{J_{abs}} \quad (6)$$

$$\eta_{\mathrm{inj}} = \frac{J^{H_2O}}{J^{Na_2SO_3}} \quad (7)$$

Where J^{Na2SO3} and J^{H2O} are photocurrent densities obtained in 1 M NaOH electrolyte with and without 1 M Na_2SO_3, respectively. The J_{abs} was calculated by the overlapped areas between UV–vis absorption spectrum and AM 1.5G solar spectrum according to the following equation:

$$J_{abs} = \int \frac{\lambda}{1240} \cdot \varphi\mathrm{AM\ 1.5G}(\lambda) \cdot \mathrm{LHE}\ \mathrm{d}\lambda \quad (8)$$

$$\mathrm{LHE} = 1 - 10^{-A(\lambda)} \quad (9)$$

Where λ is the wavelength (nm), φAM 1.5G(λ) provides the simulated solar spectral irradiance (W m^{-2} nm^{-1}), LHE is the light harvesting efficiency, A(λ) is the absorbance at wavelength λ.

The experiment of gas evolution for water splitting was carried out in a completely sealed quartz reactor. The electrode with an area of 1 cm^2 was immersed in the electrolyte in a three-electrode configuration. Prior to the reaction and sealing processes, the electrolyte was purged with argon gas. The generated H_2 and O_2 were analysed with a thermal conductivity detector (TCD) gas chromatograph (Shimadzu GC-8AIT, argon carrier). Similarly, AM 1.5 G solar simulation (WXS-80C-3 AM 1.5 G) with a light intensity of 100 mW cm^{-2} was utilized as the light sources directly without adding any light filter.

3.3 Results and discussion

3.3.1 Synthesis and characterization of MXene nanosheets (MNs)

A schematic illustration for the synthesis of MXene nanosheets (MNs) and fabrication of MNs decorated α-Fe_2O_3 photoanode is shown in Figure 3.1. A common MAX phase of Ti_3AlC_2 (Figure 3.2a) was firstly etched by the HF, producing stacked MXene layers ($Ti_3C_2T_x$, T represents the functional groups of −O, −OH and −F on the surface) with accordion-like architecture (Figure 3.2b). Then the MXene flakes (Figure 3.2c) were successfully delaminated by centrifugation and sonication after the intercalation of TMA^+ ions into the stacked layers. The transformation from the phase of Ti_3AlC_2 to $Ti_3C_2T_x$ is

verified by the disappearance of the XRD peak at ~39° (the characteristic peak of Ti_3AlC_2) and the obvious shift of (002) and (004) peaks to the lower degrees (Figure 3.3).[26] In order to make it easier to integrated with the α-Fe_2O_3 nanorods, the delaminated MXene flakes were downsized into small pieces of MNs with strong sonication treatment. As shown in Figure 3.2d and Figure 3.4a, the scanning electron microscope (SEM) image and atomic force microscopy (AFM) image present a well-defined 2D structure of the ultrathin MNs, with a planar size of ~100 nm and an ultrathin thickness of ~3.5 nm. The formation of MNs was further confirmed by the XRD pattern in Figure 3.3, with a more negative shift of (002) shift compared with the stacked MXene layers and decreased intensity of the peaks due to the dimension change.[27] Meanwhile, a typical Tyndall effect can be observed in the colloid solution of MNs (Figure 3.4b), suggesting a homogeneous dispersion of MNs in the solvent.

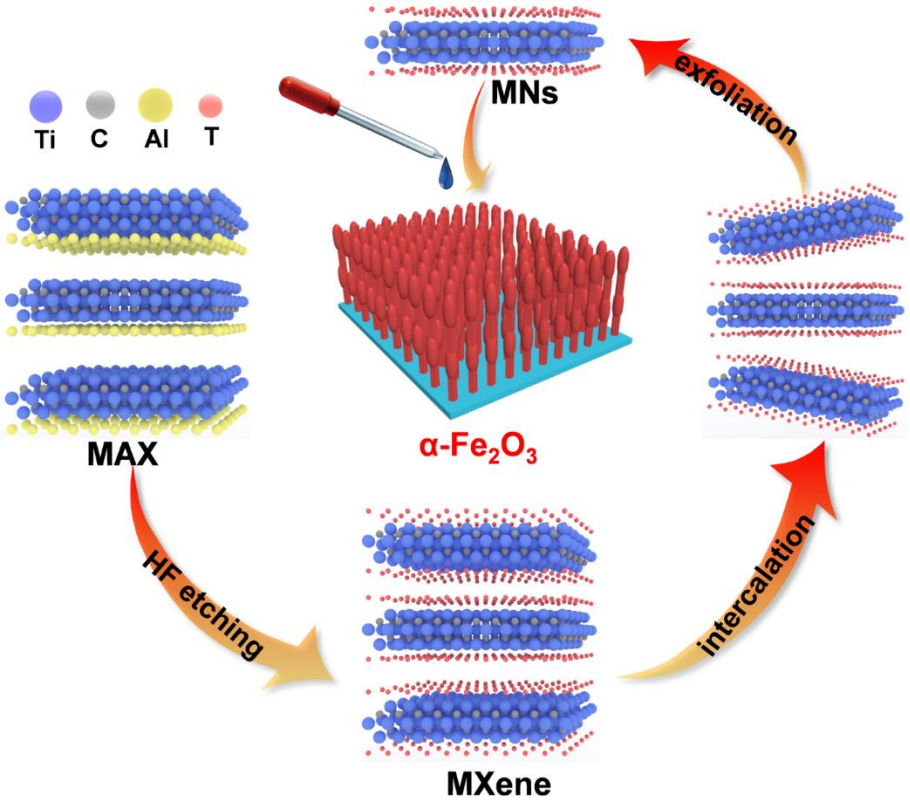

Figure 3.1 Schematic illustration of preparation process of MNs and fabrication of MNs/α-Fe_2O_3 photoanode.

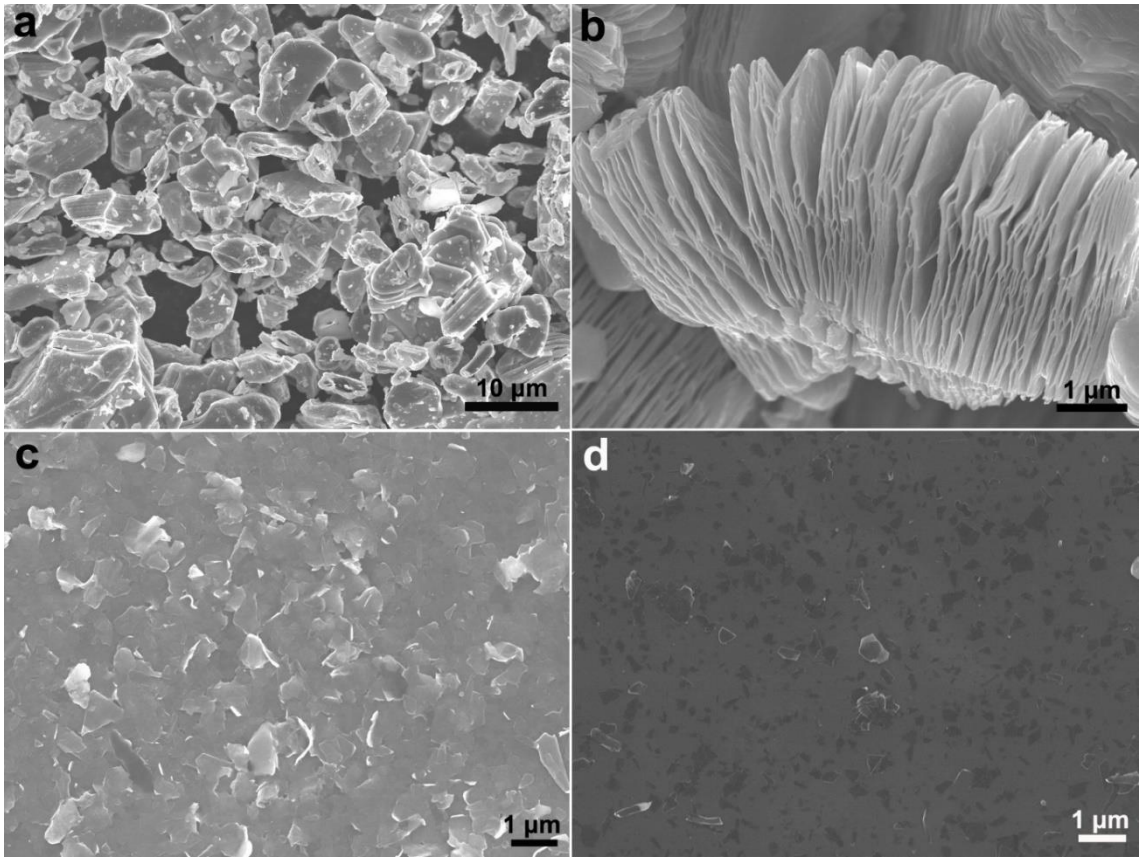

Figure 3.2 SEM images of a) Ti_3AlC_2 powder, b) stacked MXene layers, c) delaminated MXene flakes and d) downsized MXene nanosheets after strong sonication.

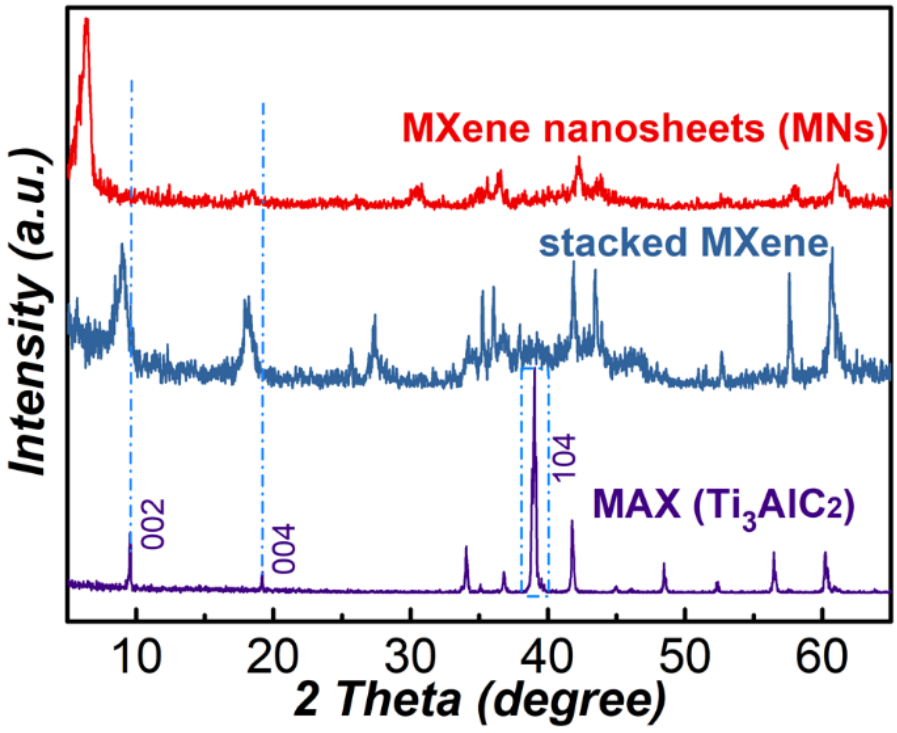

Figure 3.3 XRD patterns of Ti_3AlC_2 powder, stacked MXene layers after etching with HF

and MNs after strong sonication.

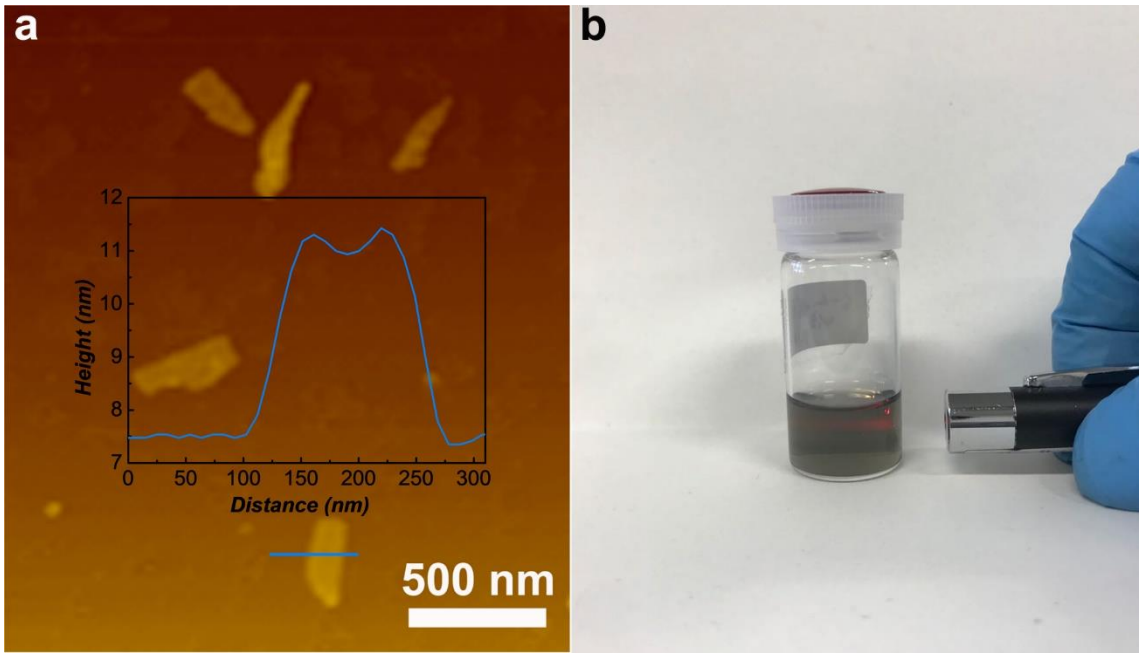

Figure 3.4 a) AFM image of ultrathin MNs. Inset of AFM image shows the height profile along the blue line. b) The digital photograph of MNs dispersed in ethanol. A significant Tyndall effect is found in the MNs colloid solution.

The surface properties and chemical components of the MNs were further evaluated by the Raman spectra and X-ray photoelectron spectroscopy (XPS) measurement. The characteristic peaks in the Raman spectrum of MNs confirm the formation of the Ti_3AlC_2 phrase and the coexistence of various surface terminated functional group (Figure 3.5).[26] The peaks at 207 and 749 cm^{-1} are assigned to the Ti-C and C-C vibrations ($A1_g$ symmetry) of the oxygen-terminated $Ti_3C_2O_2$, while the peak at 373 cm^{-1} is attributed to the O atoms E_g vibrations. The peak at 621 cm^{-1} comes mostly from E_g vibrations of the C atoms in the OH-terminated MXene. The above results illustrate that there are some surface terminations on the surface of MXene, such as -OH and -O. The MNs has broader Raman peaks which are probably due to the coexistence of various surface terminated functional groups that can have this effect on phonon dispersion of MXene.[20] Moreover, absence of peak at 144 cm^{-1} reveals that no titanium dioxide has been formed on the surface of MNs. The presence of abundant hydrophilic functionalities (–O, –OH) on MNs is further supported by the XPS spectra of O *1s* and Ti *2p* (Figure 3.6).[28] Thus, the abundant surface functionalities and homogeneous dispersion of ultrathin MNs could greatly favor their intimate coupling with other materials.

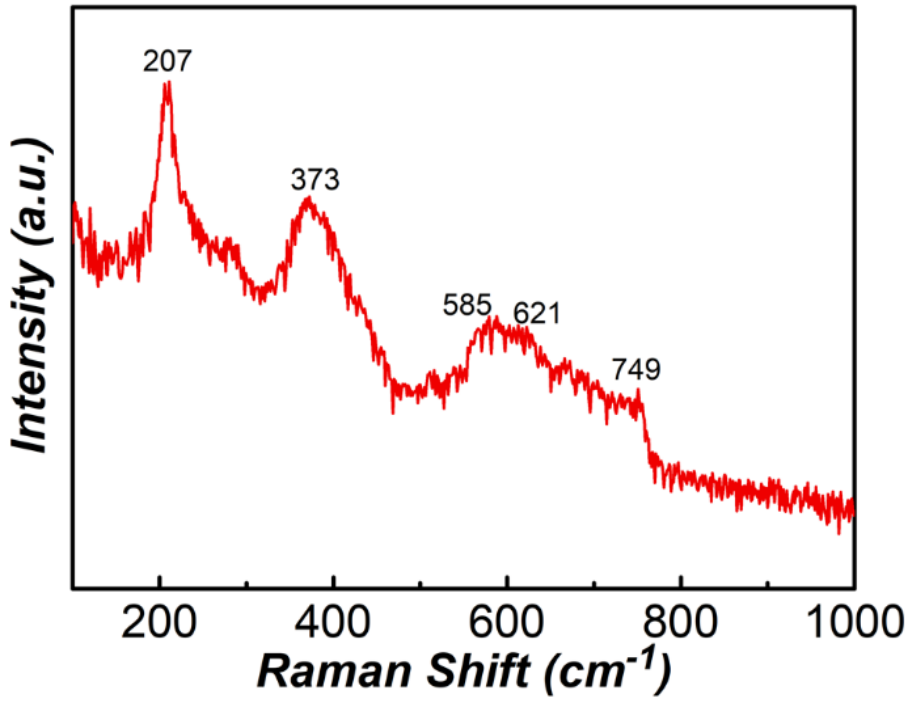

Figure 3.5 Raman spectrum of MNs after strong sonication.

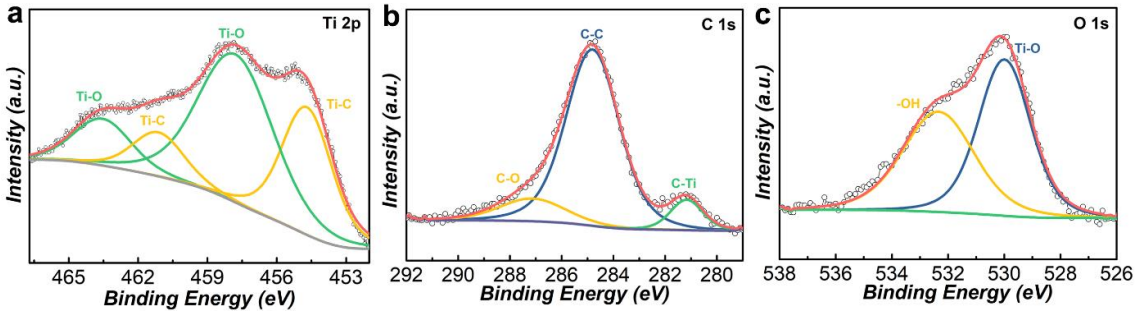

Figure 3.6 High-resolution XPS survey spectra of a) Ti *2p*, b) C *1s* and c) O *1s* in MNs.

3.3.2 Characterization of modified photoanodes

Then, the ultrathin MNs were deposited uniformly on the surface of α-Fe_2O_3 via spin-coating method, followed by annealing at 150 ^oC to reinforce the contact between MNs and α-Fe_2O_3. The XRD patterns of α-Fe_2O_3, MNs/α-Fe_2O_3 and Co-Pi/MNs/α-Fe_2O_3 films in Figure 3.8a present similar diffraction peaks assigned to α-Fe_2O_3 and SnO_2 (from FTO substrate). Distinct peaks of α-Fe_2O_3 at 35.6^o and 63.9^o can be observed, which are well coincided with the α-Fe_2O_3 crystal structure (PDF # 33-0664). There are no peaks ascribed to MNs and Co-Pi in XRD results of modified films, presumably owing to the low loading amount and ultrathin property. Figure 4.8b shows UV–vis spectra of α-Fe_2O_3, MNs/α-Fe_2O_3 and Co-Pi/MNs/α-Fe_2O_3 films. A light absorption edge of ~580 nm with a

bandgap energy of 2.09 eV (Tauc plots in Figure 3.9) is exhibited by bare α-Fe_2O_3, which consists well with the reported values.[10] After being modified with MNs and Co-Pi, the absorption intensity and bandgap of α-Fe_2O_3 remain almost unchanged. Therefore, it can be deduced that the MNs and Co-Pi have negligible effect on the structure and optical absorption property of α-Fe_2O_3 film. Compared with the bare α-Fe_2O_3, thin MNs are distributed on the surface of α-Fe_2O_3 nanorods from the SEM and TEM images (marked with red circles) in Figure 3.7a~3.7c, indicating intimate contact between α-Fe_2O_3 and MNs. A distinct interfacial structure with ultrathin MNs compactly clinging to the α-Fe_2O_3 nanorods is clearly observed from the high-resolution TEM (HRTEM) image in Figure 3.7d. The existence and distribution of Fe, O, Ti and C elements in the MNs/α-Fe_2O_3 are also confirmed by the TEM-EDS elemental mappings in Figure 3.7e.

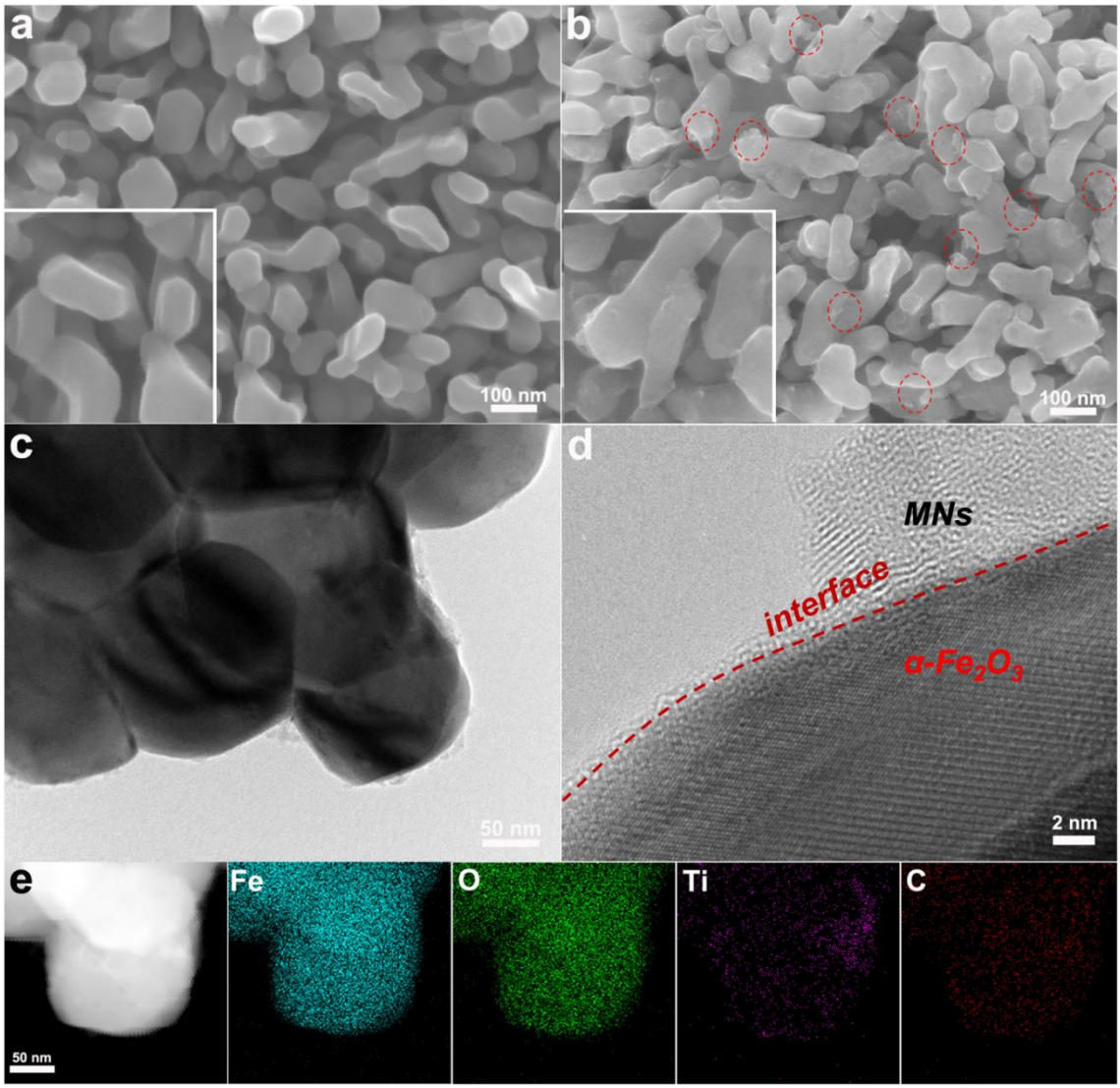

Figure 3.7 Top-view SEM images of a) α-Fe_2O_3 and b) MNs/α-Fe_2O_3 (inset is the magnified images); c) TEM image and d) HRTEM image of MNs/α-Fe_2O_3 and e) EDS

elemental mapping images of MNs/α-Fe_2O_3 refer to the signals of Fe, O, Ti and C, respectively.

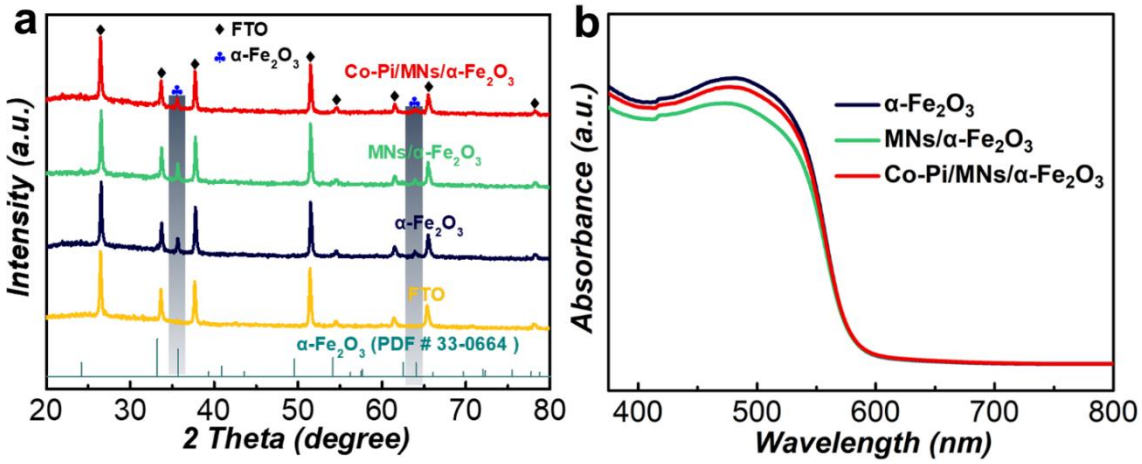

Figure 3.8 a) XRD patterns of Co-Pi/MNs/α-Fe_2O_3, MNs/α-Fe_2O_3, α-Fe_2O_3 and FTO and b) UV–visible diffuse reflection spectra of Co-Pi/MNs/α-Fe_2O_3, MNs/α-Fe_2O_3 and α-Fe_2O_3.

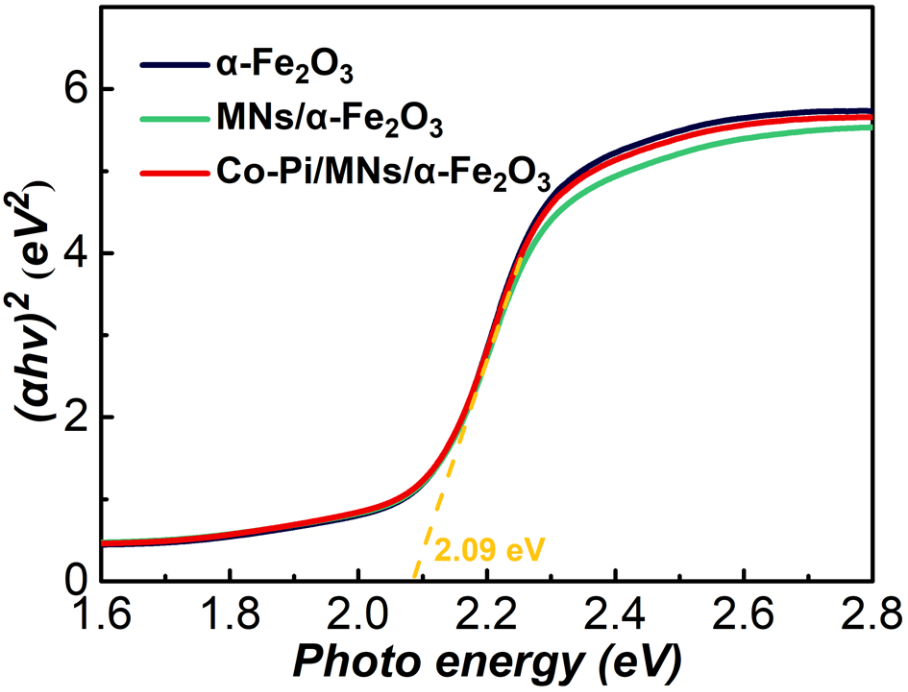

Figure 3.9 Tauc plots of α-Fe_2O_3, MNs/α-Fe_2O_3 and Co-Pi/MNs/α-Fe_2O_3.

Due to the difference in working functions, the intimate contact between the α-Fe_2O_3 and MNs (with the metallic property) make it easy to construct a heterostructure with a built-in electric field, which is beneficial for the charge transfer and separation in the

photoanode.[29-31] To gain insight into the electronic structures of the MNs/α-Fe_2O_3 junction, the band structure of α-Fe_2O_3 and the work function of MNs were investigated by ultraviolet photoelectron spectroscopy (UPS). As shown in Figure 3.10a, the secondary electron cut-off energy of α-Fe_2O_3 is 16.58 eV, then the work function of α-Fe_2O_3 is calculated to be 4.64 eV as the photon energy of exciting radiation is 21.22 eV. With the same calculation method, the work function of MNs could also be obtained to be 5.78 eV as the secondary electron cut-off energy of MNs is 15.44 eV. Then the energy band diagrams of α-Fe_2O_3 and MNs can be illustrated in Figure 3.10c. Since the work function of MNs is larger than that of the α-Fe_2O_3, their contact causes the electrons to flow from α-Fe_2O_3 to MNs, thereby forming a depletion layer at the interface between α-Fe_2O_3 and MNs. Such contact is termed as the Schottky contact, resulting in a built-in electric field pointing from α-Fe_2O_3 to MNs and band bending upwards due to the repulsion from the negatively charged layer located on the MNs side.[30] When the MNs/α-Fe_2O_3 heterostructure exposed to the illumination, the photogenerated carriers could be separated by the built-in electric field, with holes transporting to MNs and electrons flowing to the external circuit. The formation of the built-in electric field can also facilitate the enhancement of the photovoltage, thus lowering the overpotential for the desired reaction. The ultimate contact between α-Fe_2O_3 and MNs could also be verified by the XPS measurement. As shown in Figure 3.10e-3.10f, the Fe *2p* XPS spectrum of MNs/α-Fe_2O_3 exhibits a positive shift of ~0.4 eV compared with the pure α-Fe_2O_3. Accordingly, the binding energy of Ti *2p* XPS spectrum in MNs displays a negative shift of ~0.3 eV after integrated with α-Fe_2O_3. The electron donation/withdrawing behaviors illustrated by the XPS measurement verified the strong interaction between α-Fe_2O_3 and MNs.

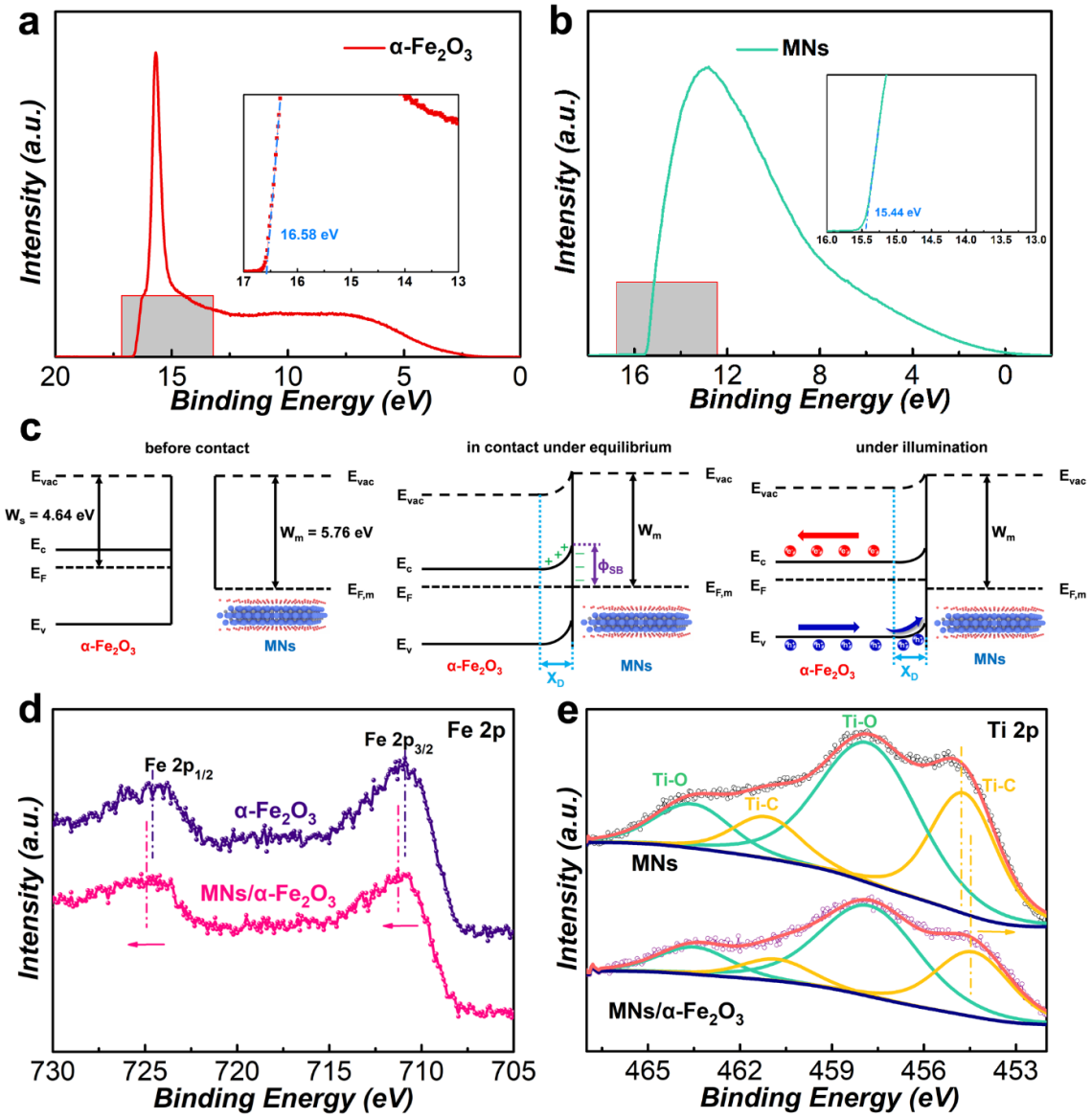

Figure 3.10 Electronic structure characterization. UPS spectra of a) α-Fe_2O_3 and b) MNs (insets are the magnified region). c) Energy band diagrams of MNs/α-Fe_2O_3 Schottky junction, where E_{vac} = vacuum energy; E_c = energy of conduction band minimum; E_v = energy of valence band maximum; $E_{F,m}$ = Fermi level of MNs; E_F = Fermi level of α-Fe_2O_3; W_m = work function of MNs; W_s = work function of α-Fe_2O_3; ϕ_{SB} = Schottky barrier at the interface. d) Fe *2p* and e) Ti *2p* XPS spectra of α-Fe_2O_3 and MNs/α-Fe_2O_3.

3.3.3 PEC performance of different photoanodes

The impact in the PEC performance by the Schottky contact between MNs and α-Fe_2O_3 was investigated by the electrochemical measurement under AM 1.5 G irradiation with a standard three-electrode system in 1 M NaOH solution. As shown in Figure 3.11a, a slight enhancement is observed with the presence of MNs on the α-Fe_2O_3 (from 0.84 mA cm^{-2}

to 1.02 mA cm^{-2} at 1.23 V vs. RHE), while the current densities in the dark are almost coincident under the same test condition (Figure 3.12). Interestingly, the onset potential of MNs/α-Fe_2O_3 is reduced to 0.75 V vs. RHE (Figure 3.13b), showing a cathodic shift of 70 mV compared with α-Fe_2O_3 (0.82 V vs. RHE). These results imply that the improvement of the catalytic activity may be attributed to the facilitated charge transfer, rather than the surface reaction kinetics. In order to display the effect of MNs more clearly for the PEC water oxidation, the Co-Pi layer, a traditional and well-defined OEC, was deposited on the MNs/α-Fe_2O_3 to enhance the reaction kinetics with more active sites.[21] Similar to the reported results, the Co-Pi layers are coated homogeneously on the α-Fe_2O_3 nanorods (Figure 3.14a), with a rougher surface compared with the pure α-Fe_2O_3.[33-34] For the Co-Pi/MNs/α-Fe_2O_3, the Co-Pi nanolayers are compactly attached on the surface of MNs/α-Fe_2O_3, with MNs buried between Co-Pi layers and α-Fe_2O_3 nanorods (Figure 3.14b). Due to the ultrathin properties of Co-Pi layers, the structure and optical absorption property of the α-Fe_2O_3 film are maintained according to the results of XRD patterns and UV–vis spectra in Figure 3.8-3.9. Remarkably, the Co-Pi/MNs/α-Fe_2O_3 achieves a photocurrent density of 2.54 mA cm^{-2} at 1.23 V vs. RHE, nearly 1.5 times higher than that of Co-Pi/α-Fe_2O_3 (1.68 mA cm^{-2}) and 3 times higher than that of the bare α-Fe_2O_3 (0.84 mA cm^{-2}). Moreover, a low onset potential of 0.57 V vs. RHE is obtained on Co-Pi/MNs/α-Fe_2O_3, presenting a large cathodic shift of ~250 mV compared with the bare α-Fe_2O_3. The *J*-*V* curves in the dark (Figure 3.12b) display that the water oxidation ability of Co-Pi/MNs/α-Fe_2O_3 has tremendous enhancement due to the decoration of Co-Pi layers, verifying the catalytic activity of Co-Pi as an OEC. However, an energy barrier would be induced owing to the interfacial resistance between the semiconductor and OEC according to the previous reports, which impeded the rapid hole transfer to the reaction sites.[35-36] Therefore, the insertion of MNs between α-Fe_2O_3 and Co-Pi could modulate the hole transfer behaviors due to the formation of built-in electric field and high hole mobility of MNs, hence significantly enhancing the PEC performance.

The applied bias photon-to-current conversion efficiency (ABPE) was used to evaluated the conversion efficiencies of photoanodes without the contribution of bias voltage. As shown in Figure 3.11b, a maximum ABPE of 0.33 % is achieved at 0.97 V vs. RHE by Co-Pi/MNs/α-Fe_2O_3, up to 4.7 times compared with the pure α-Fe_2O_3. In addition, the phenomenon of the lower applied bias (at the maximum ABPE value) by the formation of MNs/α-Fe_2O_3 and co-catalyst (Co-Pi) modification is consistent with the

shifts of corresponding onset potentials (Fig. 3.13b), further verifying the facilitated charge transfer behavior.[37] A significant enhancement of IPCE is observed on the Co-Pi/MNs/α-Fe_2O_3 over the entire wavelength range (360-600 nm), with a maximum IPCE value of 38.2% at 360 nm (3.8 times higher than the bare α-Fe_2O_3). As obtained from the UV-vis spectra, the light absorption capability was almost unchanged after the decoration of MNs and Co-Pi. Thus, the enhanced IPCE can be attributed to the improved charge separation and reduced electron trapping sites at the surface. A sensitive photocurrent response (almost no spike appeared when the light on/off), with the highest steady photocurrent density of 2.52 mA cm^{-2}, is achieved by Co-Pi/MNs/α-Fe_2O_3 photoanode, indicating the efficient transfer of photogenerated holes for the water oxidation with reduced recombination[25] (will be discuss in details later). Encouragingly, the Co-Pi/MNs/α-Fe_2O_3 photoanode exhibits a remarkable photocurrent density of 3.20 mA cm^{-2} at 1.23 V vs. RHE under front illumination with the same experimental condition (Figure 4.15a), delivering a high ABPE of 0.49% at 0.93 V vs. RHE (Figure 3.15b). In addition, a high IPCE value of 56.1% at the wavelength of 360 nm and a sensitive photocurrent response of 3.17 mA cm^{-2} at 1.23 V vs. RHE are achieved (Figure 3.15c-3.15d). The above PEC performance of Co-Pi/MNs/α-Fe_2O_3 photoanode under front irradiation is superior or comparable to the recently reported α-Fe_2O_3-based photoanodes, as summarized in Table 3.1.

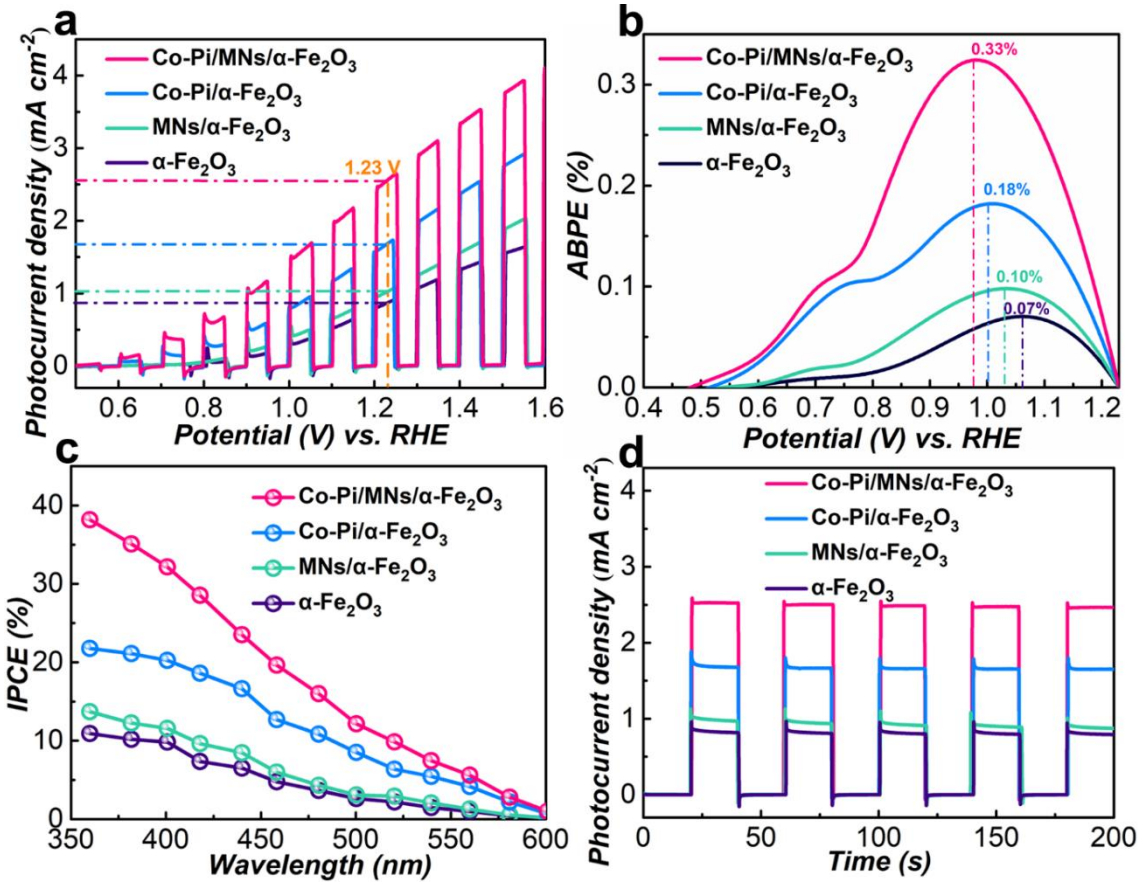

Figure 3.11 a) *J*–*V* curves, b) ABPE spectra, c) IPCE spectra and d) chopped current–time curves of bare α-Fe_2O_3, MNs/α-Fe_2O_3, Co-Pi/α-Fe_2O_3 and Co-Pi/MNs/α-Fe_2O_3 photoanodes. The measurements of IPCE spectra and current–time curves were conducted at 1.23 V vs. RHE under AM 1.5 G illumination.

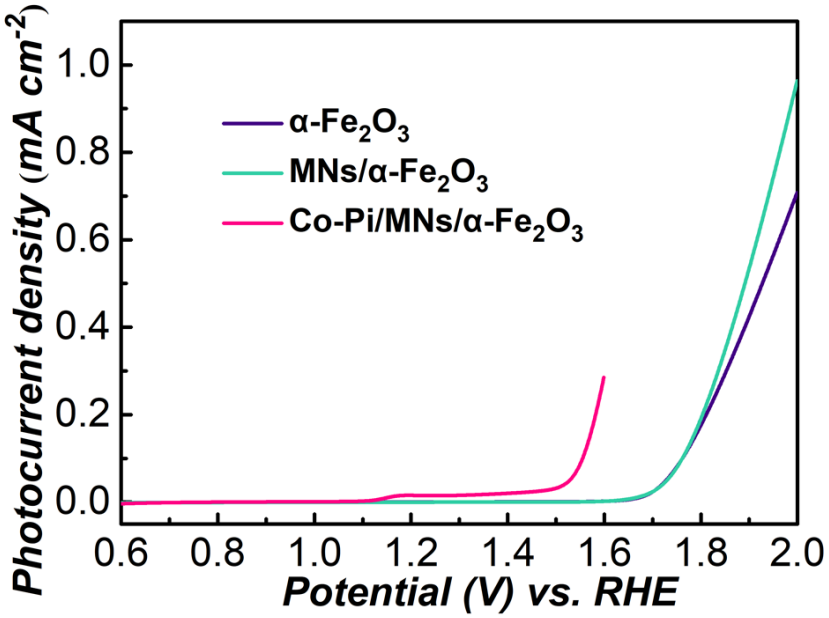

Figure 3.12 *J*–*V* curves (OER activity) of α-Fe_2O_3, MNs/α-Fe_2O_3 and Co-Pi/MNs/α-

Fe_2O_3 under dark condition in 1 M NaOH electrolyte.

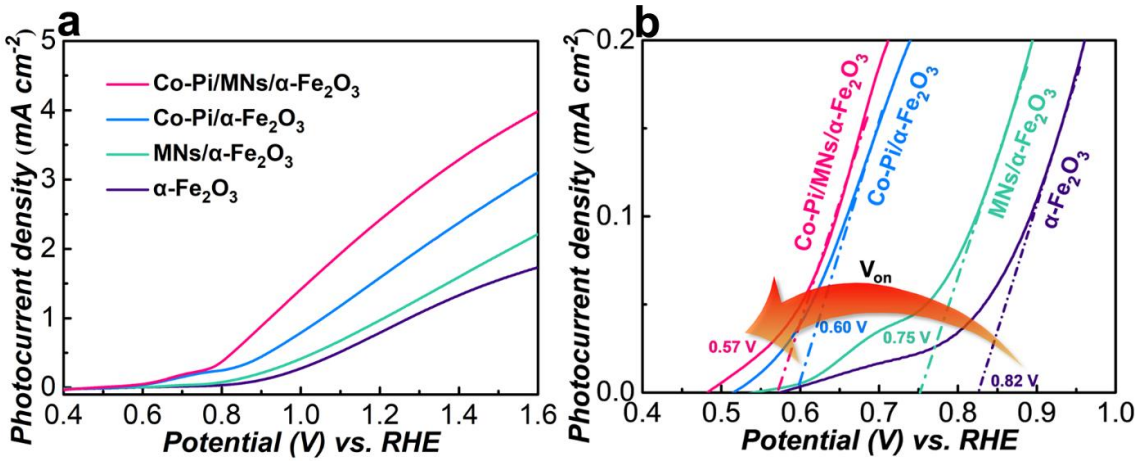

Figure 3.13 a) *J–V* curves and b) extracted onset potentials (V_{on}) by extrapolation-interception method of pristine α-Fe_2O_3, MNs/α-Fe_2O_3 and Co-Pi/MNs/α-Fe_2O_3.

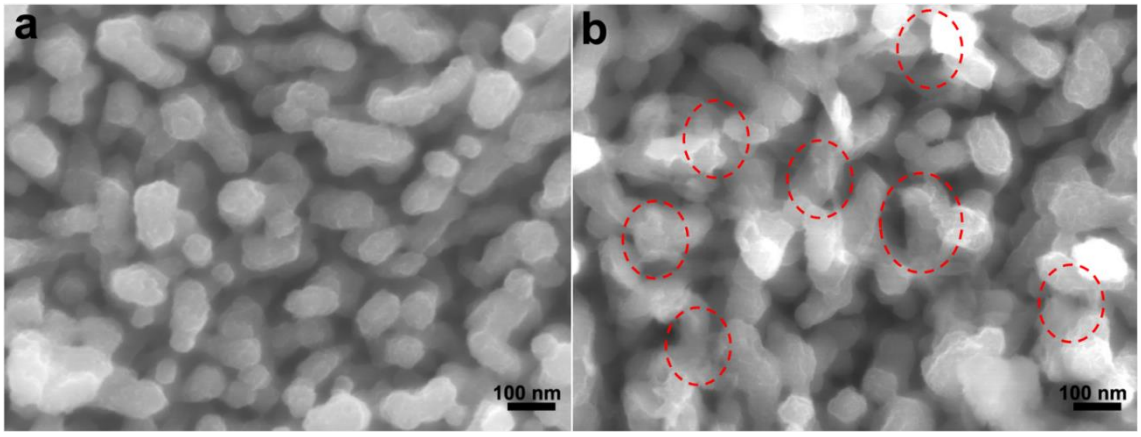

Figure 3.14 Top-view SEM images of a) Co-Pi/α-Fe_2O_3 and b) Co-Pi/MNs/α-Fe_2O_3.

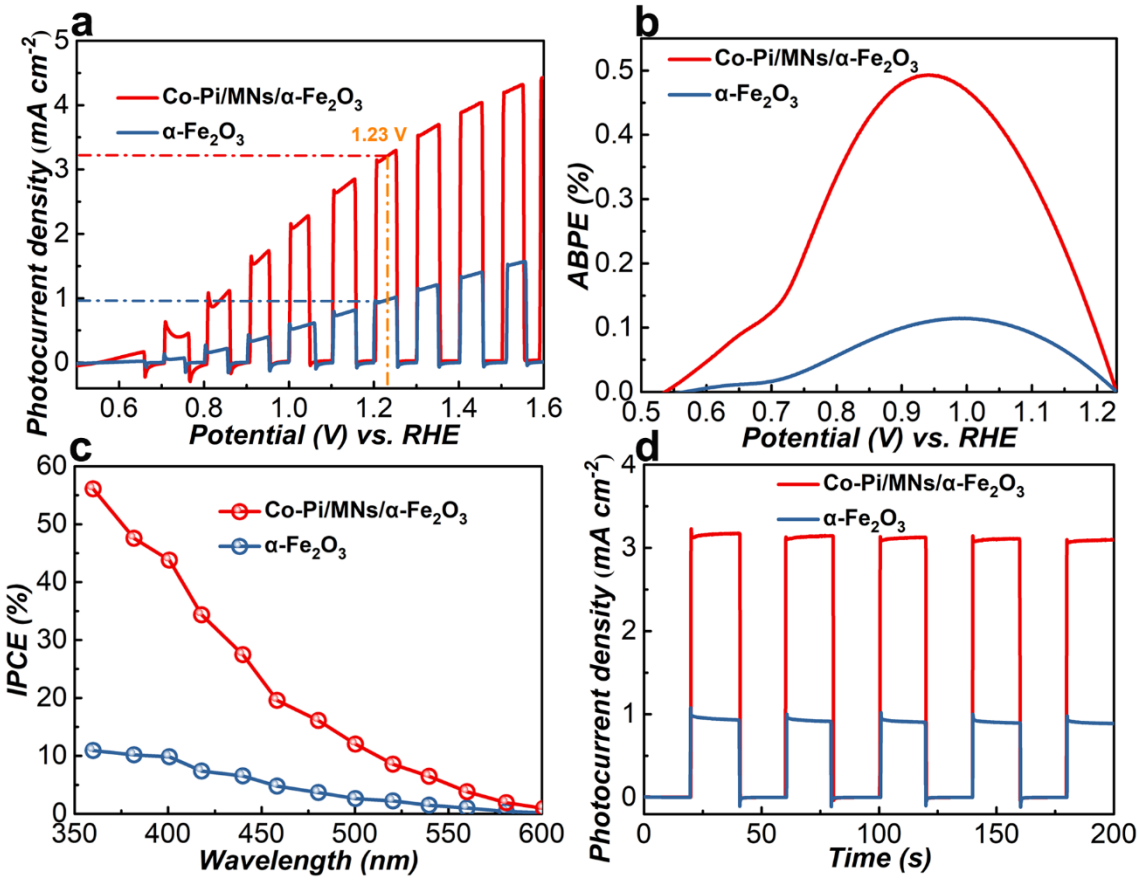

Figure 3.15 Performance of α-Fe_2O_3 and Co-Pi/MNs/α-Fe_2O_3 under front illumination. a) Chopped *J*–*V* curves, b) ABPE spectra, c) IPCE spectra and d) chopped current–time curves.

Table 3.1 Comparison of our photoanode to other similar α-Fe_2O_3-based photoanodes.

Photoanodes	Onset Potential (V) vs. RHE	Current Density at 1.23 V vs. RHE (mA cm^{-2})	Stability	Illumination Direction
Ti−Fe_2O_3/Ni(OH)$_2$/IrO_2[44]	0.73	~1.60	N.A.	N.A.
Co-Pi/Co_3O_4/Ti:Fe_2O_3[45]	0.64	2.70	N.A.	Front
Fe_2O_3/Fe_2TiO_5/FeNiOOH[46]	0.95	2.20	No decay after 2 h	Front
Co-Pi/Ti-(SiO_x/np-Fe_2O_3)[47]	0.80	3.19	No obvious decay after 2 h	Front
α-Fe_2O_3/Al_2O_3/$CuCoO_x$[48]	0.70	2.23	N.A.	Back

Co-Pi/Ag/Fe_2O_3[49]	N.A.	4.68	No obvious decay after 5 h	Front
Ti,Sn:Fe_2O_3/B:Fe_2O_3/FeOOH[50]	0.84	2.35	No obvious decay after 18 h	Front
Nb,Sn:Fe_2O_3@$FeNbO_4$/$NiFeO_x$[51]	0.71	2.71	No obvious decay after 20 h	N.A.
Fe_2O_3/Al_2O_3/$CoFeO_x$[52]	0.80	2.50	No obvious decay after 15 h	Front
α-Fe_2O_3/Au/TiO_2[53]	N.A.	1.05	No obvious decay after 12 h	Back
CDots/Co_3O_4–Fe_2O_3[54]	N.A.	1.48	No decay after 2 h	N.A.
Co-Pi/MNs/α-Fe_2O_3 (this work)	**0.57**	**2.54**	**~ 10% decay after 20 h**	**Back**
Co-Pi/MNs/α-Fe_2O_3 (this work)	**0.55**	**3.20**	**N.A.**	**Front**

3.3.4 Research on the catalytic mechanism

In order to understand the underlying mechanism of the enhanced PEC performance by the presence of MNs, kinetics of photocarriers in different photoanodes were investigated. As mentioned in the electronic structure characterization of MNs and α-Fe_2O_3, a built-in electric field can be created by the MNs/α-Fe_2O_3 junction. In order to visualize and verify the existence of built-in electric field at the MNs/α-Fe_2O_3 junction and its effects on the photogenerated charge behaviors, the measurement of open-circuit potential (OCP) decay profile was performed. The ΔOCP ($OCP_{dark} – OCP_{light)}$ represents the amount of band bending under illumination with respect to that in the dark condition, while an enlarged band bending at the photoanode/electrolyte interface represents the enhanced electron-hole separation.[39-40] As shown in Figure 3.16a, compared with the pristine α-Fe_2O_3, the MNs/α-Fe_2O_3 presents a expedite OCP decay with the generation of a larger photovoltage, verifying the formation of the strong built-in electric field on the MNs/α-Fe_2O_3 that provide an additional driving force for the charge separation.[24] The enhanced photovoltage can be also verified by the extracted photovoltage in Figure 3.17, which presents an enhancement of ~90 mV by the formation of MNs/α-Fe_2O_3 junction. The OCP decay is further enhanced by loading Co-Pi on the MNs/α-Fe_2O_3, confirming

the effectiveness of cocatalyst modification.[38] To further illustrate the charge recombination rate at the photoanode/electrolyte junction, the charge carrier lifetime could be quantified according to the equation 4 in the experimental section. The carrier lifetimes of MNs/α-Fe_2O_3 and Co-Pi/MNs/α-Fe_2O_3 are much shorter than the bare α-Fe_2O_3 at the transient when illumination is stopped (Figure 3.18). The fast decay kinetics is indicative of the enhanced charge transfer efficiency within the photoanode.[38-39, 41] Therefore, the above results confirm the existence of strong built-in electric field and large photovoltage generated by the MNs/α-Fe_2O_3 junction, resulting in an effective charge separation under PEC water splitting condition.

In order to further understand how the charge transfer behaviors were affected by the presence of MNs, the charge separation efficiency in the bulk (η_{sep}) and surface charge injection efficiency (η_{inj}) were measured and quantified with the addition of Na_2SO_3 as a hole scavenger (Figure 3.19). As shown in Figure 3.16b, the presence of MNs can enhance the η_{sep} of α-Fe_2O_3 over the entire voltage region. According to the UV-vis spectra in Figure 3.8b, the light harvesting capability of α-Fe_2O_3 would not be altered by the MNs. Thus, the improved η_{sep} of MNs/α-Fe_2O_3 can be completed attributed to the hole extraction effect of MNs. Although the water oxidation ability of MNs/α-Fe_2O_3 is similar with the bare α-Fe_2O_3, it is interesting to find that the η_{inj} of MNs/α-Fe_2O_3 is still higher than the bare α-Fe_2O_3, especially at the lower potentials (Figure 3.16c). Similar enhancement can be also observed in the values of η_{inj} between Co-Pi/MNs/α-Fe_2O_3 and Co-Pi /α-Fe_2O_3. This phenomenon should be related to the built-in electric field formed at the MNs/α-Fe_2O_3 junction, which provides a supplemental driving force to separate charge carriers and reduce the charge recombination in the photoanode.

Then the electrochemical impedance spectroscopy (EIS) was performed to visualize the charge transfer processes of the photoanodes under illumination at 1.23 V vs. RHE. All the Nyquist plots in Figure 3.16d display the feature of two typical semicircles, which then can be fitted by the equivalent circuit of two-RC-unit, as inserted in Figure 3.16d and the corresponding fitting results are summarized in Table 3.2. The resistances in the semiconductor (R_{bulk}) for photoanodes of MNs/α-Fe_2O_3 (101.8 Ω) and Co-Pi/MNs/α-Fe_2O_3 (33.3 Ω) are both lower than the bare α-Fe_2O_3 (134.6 Ω), suggesting the enhanced charge exaction effect from the bulk of α-Fe_2O_3 due to the built-in electric field by the incorporation of MNs. Additionally, the charge transfer resistance at the photoanode/electrolyte interface (R_{ct}) presents a dramatical decrease, which varied from

369.2 Ω of pure α-Fe_2O_3 to 138.8 Ω of Co-Pi/MNs/α-Fe_2O_3, signifying the enhanced hole injection efficiency into electrolyte on Co-Pi/MNs/α-Fe_2O_3 photoanode.

The dynamics of the charge carries during the water oxidation was further elucidated by the photocurrent transient measurements generated by light chopping. According to the previous reports, the photogenerated holes would be easy to accumulated due to the sluggish reaction kinetic and poor charge transfer efficiency at the photoanode/electrolyte interface when the light was on, inducing a sharp anodic current spike.[42-43] The phenomenon of the transient photocurrent spike is obvious at the low potentials owing to the weak driving force and then drastically decreases at high potential as a larger proportion of holes have sufficient potential to oxidize water, which is visualized in the LSV curves under chopped light in Figure 3.11a. In order to investigate the hole accumulation of different photoanodes at the low potential, the photocurrents at different potentials (0.8-1.0 V) with respect to time of α-Fe_2O_3 and MNs/α-Fe_2O_3 were integrated in Figure 3.20a. The photocurrent transient spikes of MNs/α-Fe_2O_3 display an obvious decrease compared with the bare α-Fe_2O_3, which means that the MNs causes fewer holes to accumulate at the photoanode/electrolyte interface, indicating the enhanced charge transfer efficiency and reduced charge recombination due to the decoration of MNs. The similar phenomenon can be also observed in the chopped *J-V* curves of Co-Pi/α-Fe_2O_3 and Co-Pi/MNs/α-Fe_2O_3 photoanodes in potential ranging from 0.6 to 1.23 V vs. RHE (Figure 3.20b). These results further verified the strong capability of MNs to extract the holes from the semiconductor with the built-in electric field and perform hole transfer towards water oxidation due to the high hole mobility.

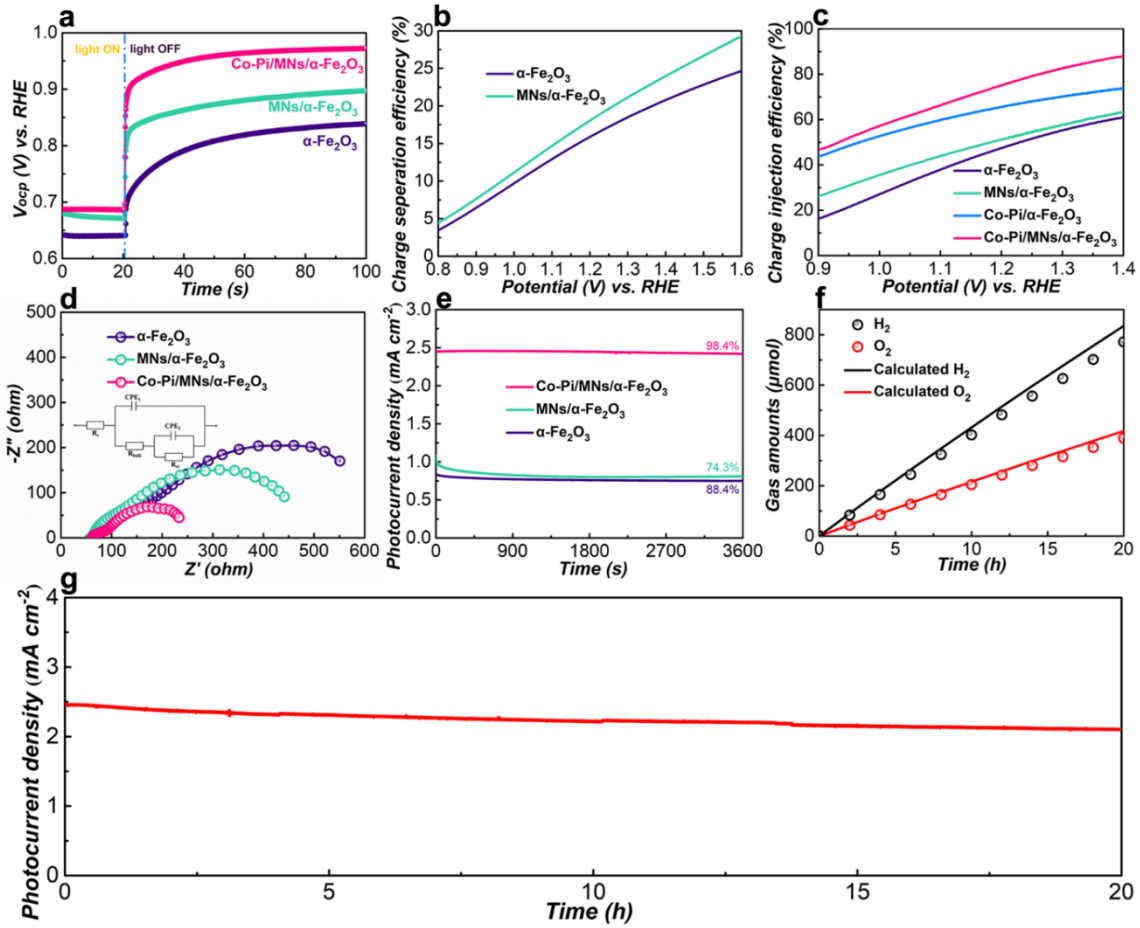

Figure 3.16 PEC performance and electrochemical characterization. a) OCP decay profiles of α-Fe_2O_3, MNs/α-Fe_2O_3 and Co-Pi/MNs/α-Fe_2O_3. b) Charge separation efficiencies of α-Fe_2O_3 and MNs/α-Fe_2O_3. c) Charge injection efficiencies of α-Fe_2O_3, MNs/α-Fe_2O_3, Co-Pi/α-Fe_2O_3 and Co-Pi/MNs/α-Fe_2O_3. d) EIS plots measured at 1.23 V vs. RHE under AM 1.5G illumination. e) Photocurrent density stability of α-Fe_2O_3, MNs/α-Fe_2O_3 and Co-Pi/MNs/α-Fe_2O_3 photoanodes at 1.23 V vs. RHE for 1 h. f) Gas evolution curves and g) long-term stability of Co-Pi/MNs/α-Fe_2O_3 photoanode at 1.23 V vs. RHE for 20 h.

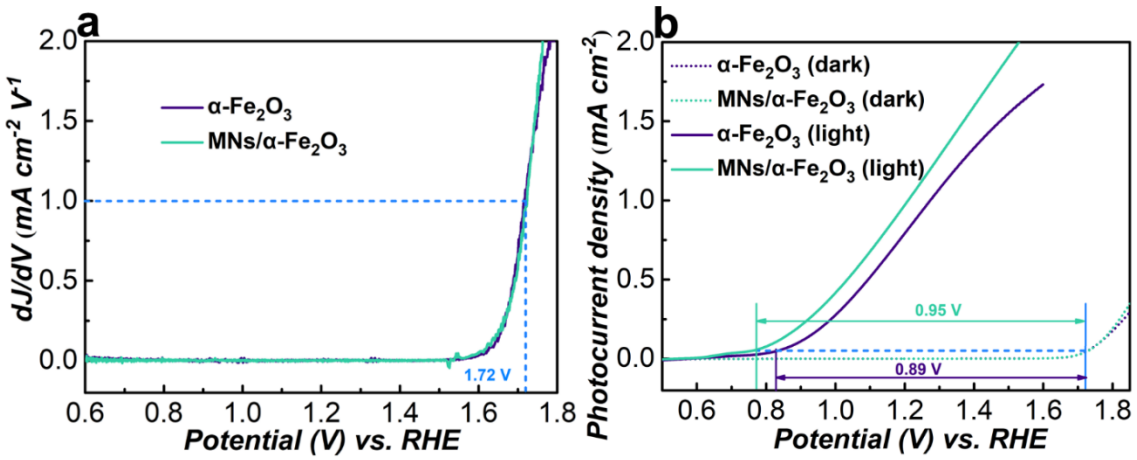

Figure 3.17. Extracted photovoltages. a) The first-order derivatives of the corresponding dark voltammogram. b) The extracted photovoltage value of pristine α-Fe_2O_3 and MNs/α-Fe_2O_3 by the corresponding potential shifts between the dark and the light current density.

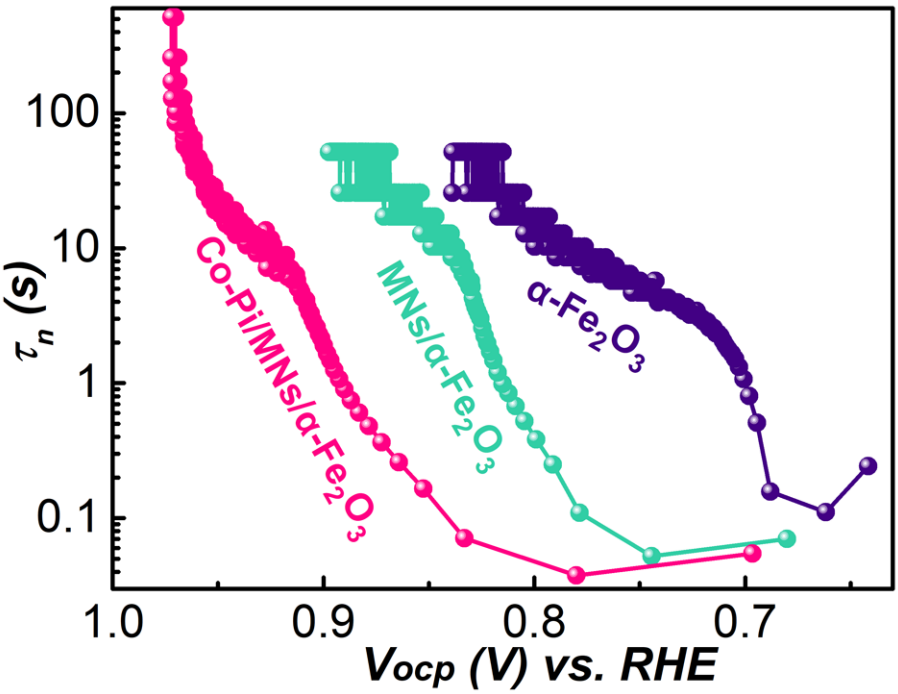

Figure 3.18 Potential-dependant carrier lifetimes derived from OCP decay profiles in the dark condition for α-Fe_2O_3, MNs/α-Fe_2O_3 and Co-Pi/MNs/α-Fe_2O_3 photoanodes.

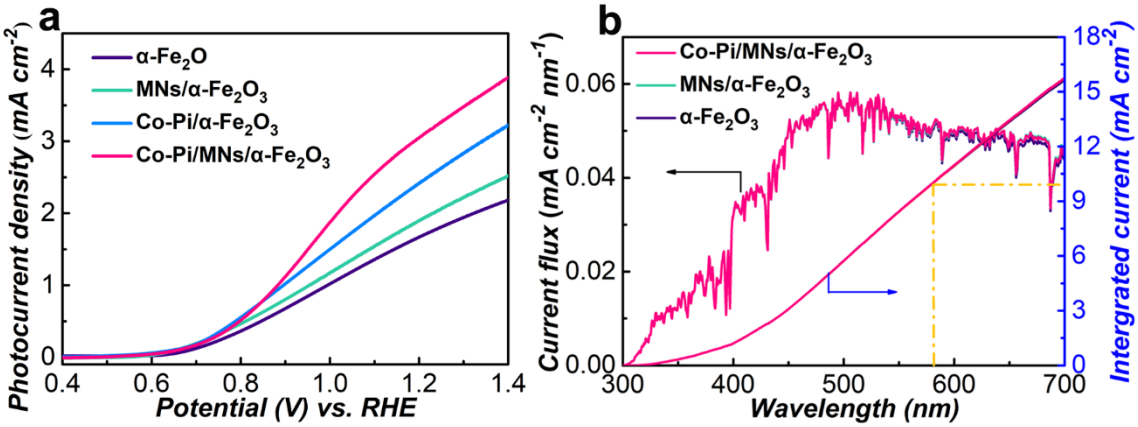

Figure 3.19 a) *J–V* curves of pristine α-Fe_2O_3, MNs/α-Fe_2O_3 and Co-Pi/MNs/α-Fe_2O_3 with Na_2SO_3 as the hole scavenger. b) The calculated current density flux and integrated current density (J_{abs}) of α-Fe_2O_3, MNs/α-Fe_2O_3 and Co-Pi/MNs/α-Fe_2O_3 photoanodes.

Table 3.2 EIS results of different photoanodes calculated by the equivalent circuit model.

Photoanode	R_s (Ω)	R_{bulk} (Ω)	R_{ct} (Ω)
α-Fe_2O_3	73.1	134.6	369.2
MNs/α-Fe_2O_3	63.1	101.8	282.8
Co-Pi/MNs/α-Fe_2O_3	65.0	33.3	138.8

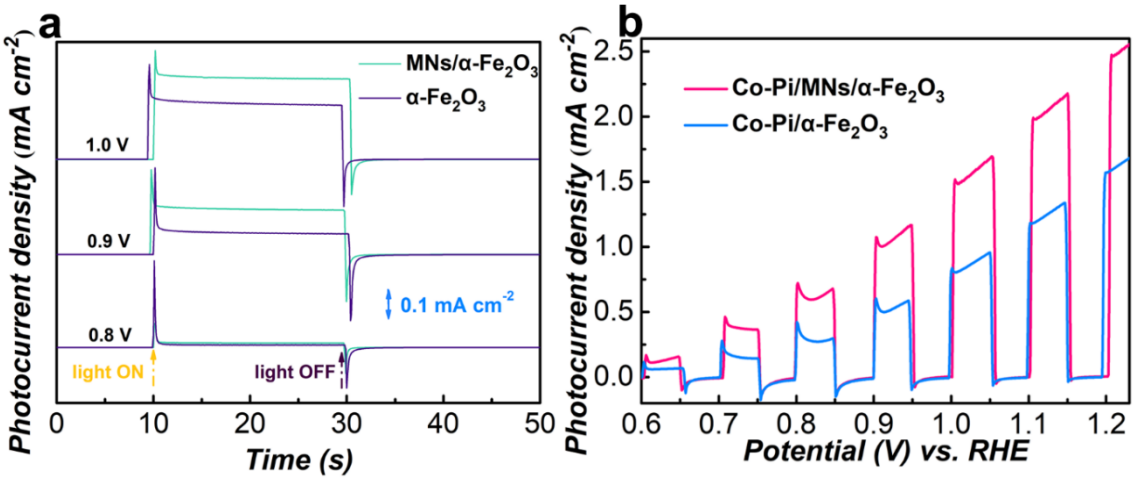

Figure 3.20. a) Transient photo-response shown by light chopping current densities (light on/light off) as a function of time. b) Chopped J-V curves of Co-Pi/α-Fe_2O_3 and Co-Pi/MNs/α-Fe_2O_3 photoanodes in potential ranging from 0.6 to 1.23 V vs. RHE

In addition, the MNs are readily oxidized under the experimental condition of PEC water oxidation. But with the optimized "sandwich" structure of Co-Pi/MNs/α-Fe_2O_3, the

MNs could be protected by the Co-Pi layer. Hence the properties of MNs can be almost maintained during the test, leading to an excellent stability of Co-Pi/MNs/α-Fe_2O_3 photoanode. As shown in Figure 3.16e, the Co-Pi/MNs/α-Fe_2O_3 photoanode exhibits a steady photocurrent density of 2.45 mA cm^{-2} at 1.23 V vs. RHE during the 1 h test. However, without the outmost Co-Pi layer, the steady-state photocurrent density of MNs/α-Fe_2O_3 gradually decays and soon the photocurrent density becomes quite close to the pure α-Fe_2O_3. This phenomenon can be attributed to the self-oxidation of MNs due to the oxygen-rich environment and anodic potential. As determined by the Ti *2p* XPS analysis in Figure 3.21, the Ti-C peaks on the MNs disappeared after 1 h testing when the MNs was directly exposed to the electrolyte, indicating the complete self-oxidation for MNs during the PEC water oxidation. However, the Co-Pi/MNs/α-Fe_2O_3 photoanode demonstrates an impressive stability over 20 h consecutive illumination under the same working condition, still retaining approximately 90 % of the initial photocurrent density (Figure 3.16g). The yields of evolved H_2 and O_2 are linear with respect to the irradiation time, with a stoichiometric ratio of ≈2:1 and a high Faradaic efficiency of 94.9% for OER (Figure 3.16f), indicating that nearly all the photogenerated holes are used for water oxidation. The morphology of the Co-Pi/MNs/α-Fe_2O_3 photoanode after stability test is well maintained according to the SEM image in Figure 3.22. Moreover, the fitting XPS result of Co-Pi/MNs/α-Fe_2O_3 before and after long-term stability test (Figure 3.23) manifests that the MNs were slightly oxidized during the test, which is much different from the MNs/α-Fe_2O_3 in Figure 3.21. Therefore, the above results further verify the protecting effect of the “sandwich” structure to impede the oxidation of MNs.

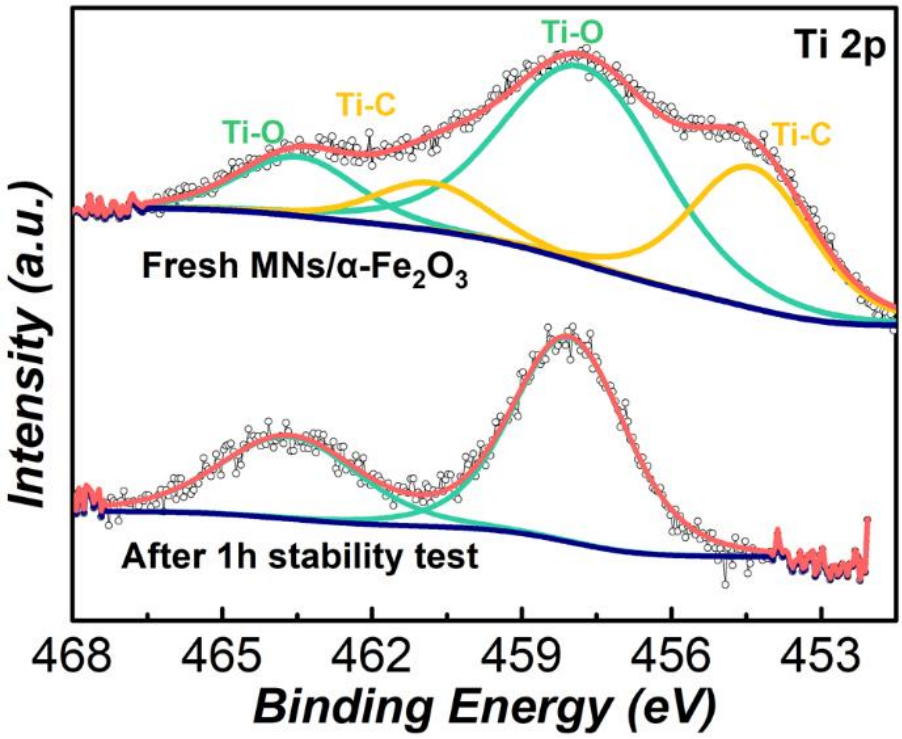

Figure 3.21 Ti *2p* XPS spectra of MNs/α-Fe_2O_3 before and after 1 h stability test. The Ti was completely oxidized when the MNs were directly exposed in the electrolyte, indicating that the MNs are not stable under the experimental condition during the PEC water oxidation. Then an optimized photoanode structure should be designed to retard the oxidation process of MNs.

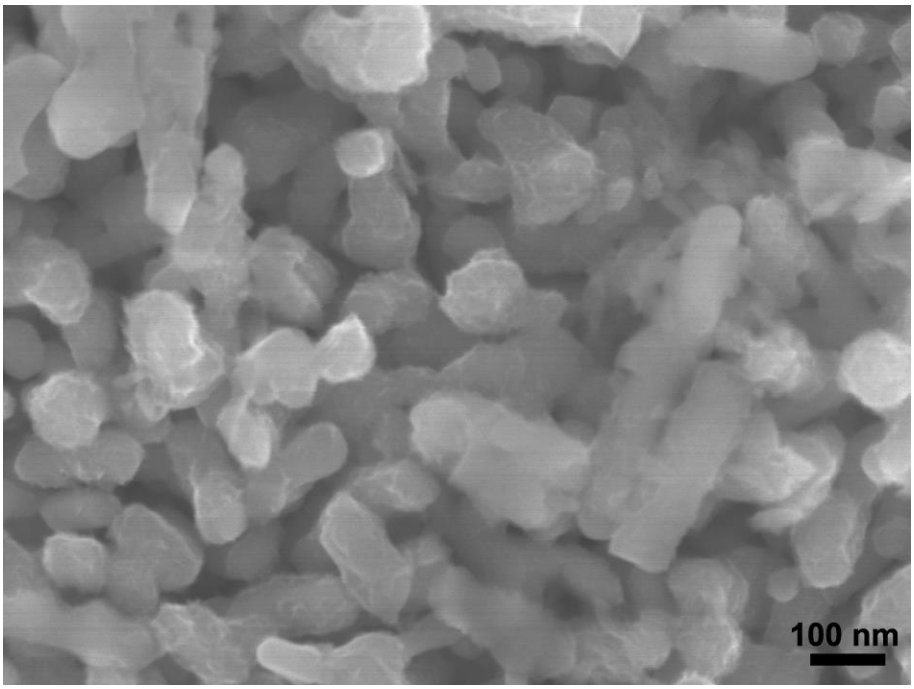

Figure 3.22 SEM images of the Co-Pi/MNs/α-Fe_2O_3 after long-term stability test.

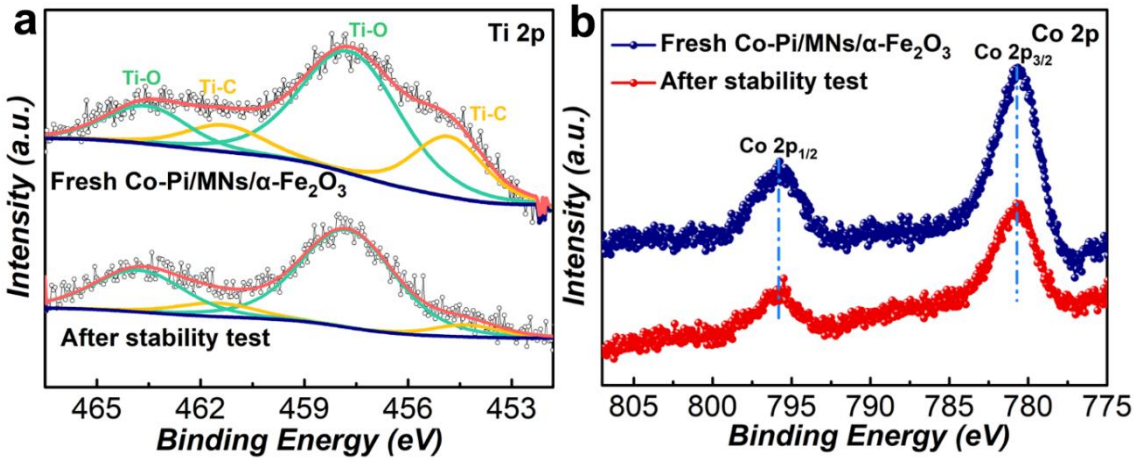

Figure 3.23 Comparison of XPS results of Co-Pi/MNs/α-Fe_2O_3 before and after long-term stability test: a) Ti *2p*, b) Co *2p*. The MNs would be partial oxidized after 20 h stability test, as evidenced by the decreased intensities Ti-C peaks. However, compared with the results in Figure 4.21, it can be concluded that the design of the "sandwich" structure of Co-Pi/MNs/α-Fe_2O_3 can protect MNs from direct exposure to the electrolyte and then maintain the function for the efficient PEC water oxidation. Nevertheless, the Co 2p spectra display no obvious change before and after long-term stability test (Figure 3.23b), indicating the Co-Pi is stable during the PEC testing.

We further found that the insertion of MNs as a hole transfer mediator between the OEC and semiconductor could be a versatile strategy for boosting the PEC performance. As a consequence, two other common-used OECs of NiOOH and FeOOH were respectively photo-electrodeposited on the MNs/α-Fe_2O_3 photoanode and the catalytic activities were evaluated by the *J-V* curves. As displayed in Figure 3.24, these two OECs with the same configuration as the Co-Pi/MNs/α-Fe_2O_3 demonstrate the similar enhancement, further verifying the impressive effect of the MNs for the PEC water oxidation. In addition, we also explored this strategy in different photoanode materials. As shown in Figure 3.25, the enhancement of the performance is evidenced by comparing the photocurrent densities of different photoanodes deposited with different surface modifiers. Similar improved trend can be observed on different photoanodes, further emphasizing the hole exaction effect of MNs. Therefore, the above results verified the university of this interfacial modulation strategy by utilizing MNs as a hole transfer mediator in PEC water oxidation. And this versatile method could be a promising approach for constructing effective PEC water splitting system.

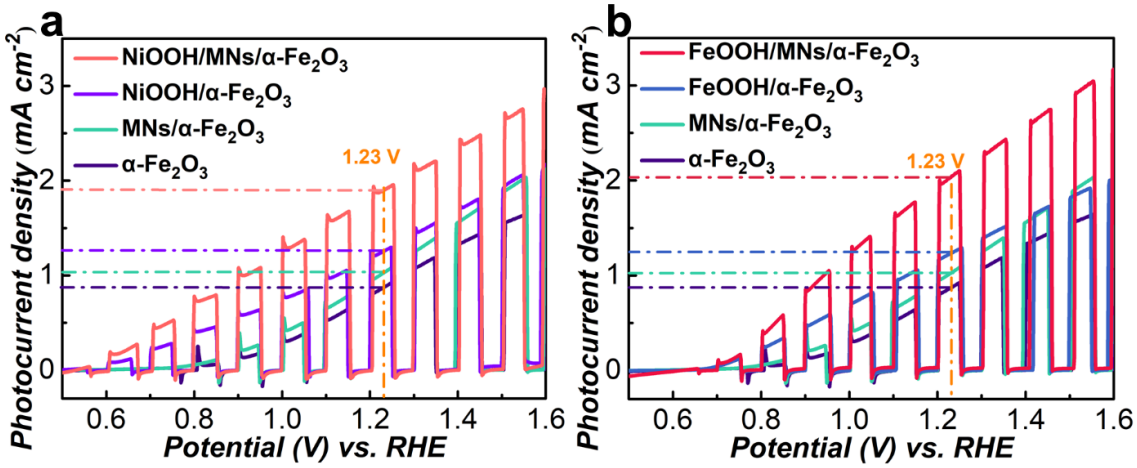

Figure 3.24 Chopped *J*–*V* curves of different OECs a) NiOOH and b) FeOOH with the same structure and modification strategy as Co-Pi/MNs/α-Fe_2O_3.

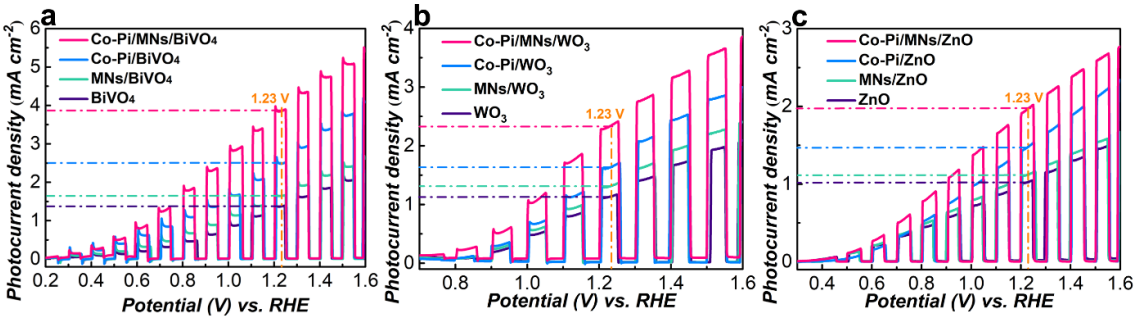

Figure 3.25 Chopped *J*–*V* curves of a) $BiVO_4$, b) WO_3 and c) ZnO with the same modification strategy as α-Fe_2O_3.

4.4 Conclusions

In this study, we have demonstrated that the insertion of MNs can serve as an excellent hole transfer mediator in a α-Fe_2O_3/OEC photoanode for PEC water oxidation. The introduction of the ultrathin MNs enables the formation of Schottky junction with α-Fe_2O_3, providing a strong built-in electric field with an additional driving force to suppress the charge recombination. Then the OECs can perform a much better catalytic activity due to the facilitated hole transfer from α-Fe_2O_3 to the OEC surface. As a result, the Co-Pi/MNs/α-Fe_2O_3 photoanode exhibits a 2-fold enhancement of photocurrent density from 0.84 to 2.54 mA cm^{-2} at 1.23 V vs. RHE and a cathodic shift of onset potential by ~250 mV from 0.82 to 0.57 V vs. RHE under AM 1.5 G illumination, comparing with the bare α-Fe_2O_3. A remarkable photocurrent density of 3.20 mA cm^{-2} at 1.23 V vs. RHE and a high ABPE of 0.49% are achieved on Co-Pi/MNs/α-Fe_2O_3 under front illumination, which is among the very best PEC performance for α-Fe_2O_3 based

photoanodes. Furthermore, the optimized burying of MNs by the OEC layer alleviated the self-oxidation, thereby prolonging the stability of Co-Pi/MNs/α-Fe_2O_3 for 20 h. Our work proposes a universal strategy for enhancing the charge transfer efficiency of the photoanodes by inserting a mediator between the semiconductor and OEC and highlights the potential for application of MNs in solar energy conversion devices.

References

[1] M. Grätzel, *Nature* **2001**, 414, 338.

[2] M. G. Walter, E. L. Warren, J. R. McKone, S. W. Boettcher, Q. Mi, E. A. Santori, N. S. Lewis, *Chem. Rev.* **2010**, 110, 6446.

[3] T. Hisatomi, J. Kubota, K. Domen, *Chem. Soc. Rev.* **2014**, 43, 7520.

[4] S. Wang, G. Liu, L. Wang, *Chem. Rev.* **2019**, 119, 5192.

[5] Y. He, T. Hamann, D. Wang, *Chem. Soc. Rev.* **2019**, 48, 2182.

[6] D. A. Wheeler, G. Wang, Y. Ling, Y. Li, J. Z. Zhang, *Energy Environ. Sci.* **2012**, 5, 6682.

[7] H. Kaneko, T. Minegishi, K. Domen, *Chem. Eur. J.* **2018**, 24, 5697.

[8] I. Roger, M. A. Shipman, M. D. Symes, *Nat. Rev. Chem.* **2017**, 1, 0003.

[9] J. H. Kim, D. Hansora, P. Sharma, J.-W. Jang, J. S. Lee, *Chem. Soc. Rev.* **2019**, 48, 1908.

[10] G. Yang, Y. Li, H. Pang, K. Chang, J. Ye, *Adv. Func. Mater.* **2019**, 29, 1904622.

[11] F. Lin, S. W. Boettcher, *Nat. Mater.* **2014**, 13, 81.

[12] Q. Yu, X. Meng, T. Wang, P. Li, J. Ye, *Adv. Func. Mater.* **2015**, 25, 2686.

[13] C. Ding, J. Shi, Z. Wang, C. Li, *ACS Catal.* **2017**, 7, 675.

[14] Z. Wang, G. Liu, C. Ding, Z. Chen, F. Zhang, J. Shi, C. Li, *J. Phys. Chem. C* **2015**, 119, 19607.

[15] C. Zachäus, F. F. Abdi, L. M. Peter, R. Van De Krol, *Chem. Sci.* **2017**, 8, 3712.

[16] K. Zhang, B. Jin, C. Park, Y. Cho, X. Song, X. Shi, S. Zhang, W. Kim, H. Zeng, J. H. Park, *Nat. Commun.* **2019**, 10, 1.

[17] X. Ning, B. Lu, Z. Zhang, P. Du, H. Ren, D. Shan, J. Chen, Y. Gao, X. Lu, *Angew. Chem. Int. Ed.* **2019**, 58, 16800.

[18] H. J. Ahn, K. Y. Yoon, M. J. Kwak, J. H. Jang, *Angew. Chem. Int. Ed.* **2016**, 128, 10076.

[19] S. Li, Q. Zhao, D. Meng, D. Wang, T. Xie, *J. Mater. Chem. A* **2016**, 4, 16661.

[20] M. Naguib, M. Kurtoglu, V. Presser, J. Lu, J. Niu, M. Heon, L. Hultman, Y. Gogotsi, M. W. Barsoum, *Adv. Mater.* **2011**, 23, 4248.

[21] B. Anasori, M. R. Lukatskaya, Y. Gogotsi, *Nat. Rev. Mater.* **2017**, 2, 1.

[22] Z. Kang, Y. Ma, X. Tan, M. Zhu, Z. Zheng, N. Liu, L. Li, Z. Zou, X. Jiang, T. Zhai, *Adv. Electron. Mater.* **2017**, 3, 1700165.

[23] H. C. Fu, V. Ramalingam, H. Kim, C. H. Lin, X. Fang, H. N. Alshareef, J. H. He, *Adv. Energy Mater.* **2019**, 9, 1900180.

[24] Y. Lee, S. J. Kim, Y.-J. Kim, Y. Lim, Y. Chae, B.-J. Lee, Y.-T. Kim, H. Han, Y. Gogotsi, C. W. Ahn, *J. Mater. Chem. A* **2020**, 8, 573.

[25] T. Habib, X. Zhao, S. A. Shah, Y. Chen, W. Sun, H. An, J. L. Lutkenhaus, M. Radovic, M. J. Green, *npj 2D Mater. Appl.* **2019**, 3, 1.

[26] T. Y. Ma, J. L. Cao, M. Jaroniec, S. Z. Qiao, *Angew. Chem. Int. Ed.* **2016**, 128, 1150.

[27] J. Ran, G. Gao, F.-T. Li, T.-Y. Ma, A. Du, S.-Z. Qiao, *Nat. Commun.* **2017**, 8, 1.

[28] X. Liang, A. Garsuch, L. F. Nazar, *Angew. Chem. Int. Ed.* **2015**, 127, 3979.

[29] C. Jiang, S. J. Moniz, A. Wang, T. Zhang, J. Tang, *Chem. Soc. Rev.* **2017**, 46, 4645.

[30] Z. Zhang, J. T. Yates Jr, *Chem. Rev.* **2012**, 112, 5520.

[31] I. A. Digdaya, G. W. Adhyaksa, B. J. Trześniewski, E. C. Garnett, W. A. Smith, *Nat. Commun.* **2017**, 8, 1.

[32] D. K. Zhong, D. R. Gamelin, *J. Am. Chem. Soc.* **2010**, 132, 4202.

[33] D. K. Zhong, M. Cornuz, K. Sivula, M. Grätzel, D. R. Gamelin, *Energy Environ. Sci.* **2011**, 4, 1759.

[34] P. Peerakiatkhajohn, J. H. Yun, H. Chen, M. Lyu, T. Butburee, L. Wang, *Adv. Mater.* **2016**, 28, 6405.

[35] X. Chang, T. Wang, P. Zhang, J. Zhang, A. Li, J. Gong, *J. Am. Chem. Soc.* **2015**, 137, 8356.

[36] T. W. Kim, K.-S. Choi, *Science* **2014**, 343, 990.

[37] H. Zhang, D. Li, W. J. Byun, X. Wang, T. J. Shin, H. Y. Jeong, H. Han, C. Li, J. S. Lee, *Nat. Commun.* **2020**, 11, 1.

[38] S. S. Yi, B. R. Wulan, J. M. Yan, Q. Jiang, *Adv. Func. Mater.* **2019**, 29, 1801902.

[39] M. Zhong, T. Hisatomi, Y. Kuang, J. Zhao, M. Liu, A. Iwase, Q. Jia, H. Nishiyama, T. Minegishi, M. Nakabayashi, *J. Am. Chem. Soc.* **2015**, 137, 5053.

[40] C. Du, X. Yang, M. T. Mayer, H. Hoyt, J. Xie, G. McMahon, G. Bischoping, D. Wang, *Angew. Chem. Int. Ed.* **2013**, 125, 12924.

[41] Y. Lin, Y. Xu, M. T. Mayer, Z. I. Simpson, G. McMahon, S. Zhou, D. Wang, *J. Am. Chem. Soc.* **2012**, 134, 5508.

[42] F. Le Formal, N. Tetreault, M. Cornuz, T. Moehl, M. Grätzel, K. Sivula, *Chem. Sci* **2011**, 2, 737.

[43] B. Klahr, S. Gimenez, F. Fabregat-Santiago, J. Bisquert, T. W. Hamann, *J. Am. Chem. Soc.* **2012**, 134, 16693.

[44] Z. Wang, G. Liu, C. Ding, Z. Chen, F. Zhang, J. Shi, C. Li, *J. Phys. Chem. C* **2015**, 119, 19607.

[45] S. S. Yi, B. R. Wulan, J. M. Yan, Q. Jiang, *Adv. Func. Mater.* **2019**, 29, 1801902.

[46] P. Tang, H. Xie, C. Ros, L. Han, M. Biset-Peiró, Y. He, W. Kramer, A. P. Rodríguez, E. Saucedo, J. R. Galán-Mascarós, *Energy Environ. Sci.* **2017**, 10, 2124.

[47] H. J. Ahn, K. Y. Yoon, M. J. Kwak, J. H. Jang, *Angew. Chem. Int. Ed.* **2016**, 128, 10076.

[48] S. Zhang, Z. Liu, D. Chen, W. Yan, *Appl. Catal. B* **2020**, 119197.

[49] P. Peerakiatkhajohn, J. H. Yun, H. Chen, M. Lyu, T. Butburee, L. Wang, *Adv. Mater.* **2016**, 28, 6405.

[50] H.-J. Ahn, K.-Y. Yoon, M.-J. Kwak, J. Park, J.-H. Jang, *ACS Catal.* **2018**, 8, 11932.

[51] H. Zhang, Y. K. Kim, H. Y. Jeong, J. S. Lee, *ACS Catal.* **2018**, 9, 1289.

[52] L. Liardet, J. E. Katz, J. Luo, M. Grätzel, X. Hu, *J. Mater. Chem. A* **2019**, 7, 6012.

[53] Y. Fu, C.-L. Dong, W. Zhou, Y.-R. Lu, Y.-C. Huang, Y. Liu, P. Guo, L. Zhao, W.-C. Chou, S. Shen, *Appl. Catal. B* **2020**, 260, 118206.

[54] P. Zhang, T. Wang, X. Chang, L. Zhang, J. Gong, *Angew. Chem. Int. Ed.* **2016**, 128, 5945.

Chapter 4 Constructing chemical interaction between hematite and carbon nanosheets with single active sites for efficient photoelectrochemical water oxidation

4.1 Introduction

Photoelectrochemical (PEC) water splitting is a renewable and efficient approach for the conversion of solar energy into clean hydrogen fuel.[1-4] The PEC systems generally require the semiconductor materials to absorb incident light photons and produce photogenerated electron-hole pairs to drive the water splitting reaction, possibly with the assistance of a bias voltage.[5-7] During this process, the half-reaction of oxygen evolution reaction (OER) becomes the rate-determining step due to the large kinetic energy barrier induced by the four-electron processes and complicated intermediate species.[8-10] As such, searching for an effective photoanode to drive the OER with high efficiency is indispensable. Hematite (α-Fe_2O_3) has attracted considerable attentions in recent years as a representative photoanode material due to the suitable bandgap for visible light absorption and low cost with earth-abundant elemental composition.[11] However, the occurrence of bulk/surface charge recombination owing to the poor charge transport property and short hole diffusion length of α-Fe_2O_3 still leave much room for performance improvement to the expectation.[12] Consequently, extensive efforts have been devoted to overcoming these limitations, including morphology designing,[13] heteroatom doping[14] and structural tuning.[15-16] Among these strategies, surface modification with oxygen evolution catalysts (OECs) is a feasible and efficient route to enhance the PEC performance by accelerating the surface reaction kinetics.[17-18]

To date, most of the OECs are based on the metal compounds, such as the metal oxides,[19] metal hydroxides,[17, 20] etc., which usually have rather low atom utilization efficiency owing to the limited surface sites accessible to the reactants.[21-22] Thus, great research potential still exists to expose more active sites by downsizing the OECs to clusters or even single atoms.[23] Recently, single-atom catalysts have been developed for several kinds of catalytic reactions because of the unique electronic properties.[24-25] The atomically dispersed active metal sites, particularly when implanted on the ultrathin support, can achieve maximum atom efficiency and extraordinary catalytic properties.[26]

However, such kind of promising catalysts are rarely reported in the field of PEC water oxidation.[27-28]

In addition, the introduction of OECs in PEC system are mainly emphasized to facilitate surface water oxidation reaction kinetics and passivate surface defects for reduced charge recombination.[29] Nevertheless, the effect of interfacial interaction at the junction of semiconductor and OECs, which plays a crucial role for the charge transfer to the active sites on OECs, are often ignored but should be profoundly investigated, especially when the OECs are loaded with direct-deposition method. The interaction between two different components can be divided into the physical adsorption and chemical coupling.[30] The physical adsorption, such as the Van-der-Waals force, usually leads to a weak interaction; while the chemical coupling can result in a much stronger interaction and a modulated electronic structure.[31] Therefore, construction of chemical coupling between semiconductor and OEC is highly desirable to improve the catalytic activity with a strong and compact interfacial interaction.[32] Furthermore, clarifying the exact effect of this chemical interaction at the interface in heterostructures is fairly necessary for developing efficient PEC water splitting systems.

In this work, we demonstrate a robust catalyst of single-nickel sites anchored on ultrathin carbon nanosheets (Ni-NC) and construct a strong chemical interaction between α-Fe_2O_3 and Ni-NC through facile calcination treatment. The chemical coupling facilitates the interfacial charge transfer, while the Ni single sites provide sufficient active sites for the water oxidation reaction. As expected, the optimized photoanode delivers a photocurrent density of 1.85 mA cm^{-2} at 1.23 V vs. RHE and an excellent stability for over 15 h. This work provides an inspiration to activate the PEC water oxidation through constructing chemical interactions between semiconductor and OEC and highlights the effective application of single-atom catalysts in photoelectrocatalysis.

4.2 Experimental section

4.2.1 Material preparation

Preparation of α-Fe_2O_3 films: The α-Fe_2O_3 films were prepared with the modified method in previous reports.[19] Briefly, a 40 ml aqueous solution containing $FeCl_3$ (0.15 M) and $NaNO_3$ (1 M) was transferred to a Teflon-lined stainless steel autoclave. The fluorine-doped tin oxide (FTO) glasses were ultrasonically cleaned with acetone, ethanol and deionized water sequentially for 1h and then immersed into the solution with the

conductive side facing to the wall of the autoclave. The autoclave was maintained at 95 ^{o}C for 4 h. After cooling down to the room temperature, the substrates with a uniform yellow layer were washed with deionized water for several times. Finally, the target films were obtained by calcinating at 550 °C for 2 h and 800 °C for additional 20 min in air atmosphere.

Synthesis of ultrathin N-rich carbon nanosheets with Ni single sites (Ni-NC): In a typical synthesis, a supramolecular precursor of Ni/Zn was firstly prepared with a wet-chemical method. A mixture of melamine (10 mmol), $Zn(OAc)_2$ (9.9 mmol) and $NiCl_2 \cdot 6H_2O$ (0.1 mmol) was added to 10 mL ethanol and 90 mL methanol under stirring. The dispersed solution was then transferred to an oil bath and refluxed at 70 ^{o}C for 3 h. After centrifuging and washing with ethanol at least for three times, the obtained product then dried at 70 ^{o}C under vacuum. Afterwards, the above precursor was calcinated at 650 ^{o}C for 1h and then increased to 950 ^{o}C and retained for 3 h with a ramping rate of 3 ^{o}C/min in tube furnace under a flowing argon atmosphere. Subsequently, the obtained black powder was treated with diluted HCl to remove the unstable metal species and was further downsized into ultrathin nanosheets by ball milling treatment, which was denoted as Ni-NC as the final sample. The ball milling treatment was conducted at 400 rpm in a planetary ball mill (Fritsch, P-7) for 15 h, using distilled water as the solvent. For NC, only 10 mmol $Zn(OAc)_2$ was used to prepare the precursor, the other procedures were similar with the Ni-NC.

Deposition of Ni-NC on α-Fe_2O_3 films: The obtained Ni-NC powder was suspended in ethanol and then spin-coated onto the surface of α-Fe_2O_3 films with 1000 rpm for 30 s. The samples were then annealed at 200, 300 and 400 ^{o}C in tube furnace under argon atmosphere for 2h, respectively. The corresponding samples were marked as α-Fe_2O_3-Ni-NC-200, α-Fe_2O_3-Ni-NC-300 and α-Fe_2O_3-Ni-NC-400, respectively. For comparison, the samples loaded with NC were denominated as α-Fe_2O_3-NC and α-Fe_2O_3-NC-300; the pure α-Fe_2O_3 only underwent with annealing process of 300 ^{o}C was signed as α-Fe_2O_3-300; and the α-Fe_2O_3-Ni-NC annealed at 300 ^{o}C in the air was marked as α-Fe_2O_3-Ni-NC-300-air.

4.2.2 Material characterization

X-ray diffraction (XRD) patterns were recorded on an X-ray diffractometer (X'pert powder, PANalytical B.V.) with Cu Kα radiation under 40 kV and 30 mA. Raman spectra

of the samples were characterized on the NRS-1000 Raman spectroscopy (Jasco Corp. Japan). The morphologies of the samples were characterized by scanning electron microscopy (SEM) (S-4800, Hitachi) and transmission electron microscopy (TEM) (FEI Tecnai G2 F30), coupled with energy dispersive spectrometer (EDS) to determine elementary composition. The high-angle annular dark-field scanning TEM (HAADF-STEM) characterizations were performed on a JEOL ARM-200F field-emission transmission electron microscope. The extended X-ray absorption fine structure spectra (EXAFS) and the X-ray absorption near-edge structure (XANES) spectra were performed at 1W1B station in Beijing Synchrotron Radiation Facility (BSRF). The surface morphology and thickness of the samples were measured by atomic force microscopy (AFM) (Nanocute H, Japan). Optical absorption properties were measured over an ultraviolet–visible (UV–vis) spectrophotometer (UV-2700, Shimadzu). Detailed chemical compositions were analysed by X-ray photoelectron spectroscopy (XPS) (PHI Quantera SXM, ULVAC-PHI) with a Theta probe using monochromated Mg Kα x-rays at hν = 1486.6 eV. All binding energies were referenced to the C *1s* peak (284.8 eV). The in-situ Fourier transform infrared spectroscopy (FT-IR) measurements were conducted on a JASCO FTIR-6300 spectrometer under argon with a home-built chamber. PL spectra were recorded on a JASCO FP-6500 spectrofluorometer. The fluorescence decay curve was measured using a compact fluorescence lifetime spectrometer (Quantaurus-Tau, C11367) with a nano-LED lamp, excited at 400 nm.

4.2.3 Photoelectrochemical measurements

The data of PEC performance was obtained on an electrochemical workstation (ALS/CH model 650A). The test cell was a typical three-electrode cell system with the fabricated α-Fe_2O_3 films as the working electrode, a piece of pure platinum as the counter electrode and an Ag/AgCl (3 M KCl) electrode as the reference electrode. The light source was an AM 1.5 G solar simulation system (WXS-80C-3 AM 1.5 G) with a light intensity of 100 mW cm^{-2}.The electrolyte was 1M NaOH aqueous solution with a pH of ~13.6. The available area of working electrode was fixed to 1.0×1.0 cm^2. The Photocurrent–potential (*J*–*V*) curves were obtained using linear sweep voltammogram in a voltage window of 0.6~1.6 V vs. RHE with a scan rate of 20 mV s^{-1}. Electrochemical impedance spectroscopy (EIS) plots were collected within the frequency range from 0.1 to 100000 Hz at the potential of 1.23 V vs. RHE under AM 1.5 G illumination. Mott–Schottky curves were obtained from 0.2 to 1.3 V vs. RHE in the dark at a frequency of

1000 Hz. The applied potentials vs. Ag/AgCl during the measurements could be converted to the RHE scale using the equation below.

$$E_{RHE}=E_{Ag/AgCl}+0.059\times pH+E^{0}_{Ag/AgCl} \quad (1)$$

Where E_{RHE} is the converted potential vs. RHE. $E_{Ag/AgCl}$ represents the experimental result vs. Ag/AgCl and $E^{0}_{Ag/AgCl}$ is 0.197 V at ambient temperature of 25 °C.

Applied bias photon-to-current efficiency (ABPE) was calculated using the equation below.

$$ABPE\ (\%) = \frac{J\times(1.23-V_b)}{P_{light}}\times 100\% \quad (2)$$

where J refers to the photocurrent density (mA cm^{-2}). V_b represents the applied bias vs. RHE (V), and P_{light} is the total light intensity of AM 1.5 G (100 mW cm^{-2}).

Incident photon to electron conversion efficiency (IPCE) was measured under monochromatic irradiation by using a motorized monochromator (M10; Jasco Corp.) at 1.23 V vs. RHE, which was calculated using the following equation.

$$IPCE\ (\%) = \frac{J\times 1240}{\lambda\times P_{light}}\times 100\% \quad (3)$$

In which J, λ and P_{light} refer to is the photocurrent density (mA cm^{-2}), the wavelength of light (nm) and the power density of monochromatic light (mW cm^{-2}), respectively.

The water oxidation photocurrent density could be calculated by the following formula,

$$J_{PEC} = J_{abs}\times\eta_{sep}\times\eta_{inj} \quad (4)$$

In which J_{abs} is the photocurrent density assuming that all absorbed photon can convert into current. η_{sep} is the separation efficiency of photogenerated holes that reach to the catalytic surface. η_{inj} is the injection efficiency of photogenerated holes that inject into the electrolyte. With the presence of Na_2SO_3 (hole scavenger), the holes that arrived to the surface can be effectively trapped, without influencing the charge separation on the electrode (η_{inj} assumed to be 100%). Therefore, the charge separation efficiency in the bulk (η_{sep}) and surface charge injection efficiency (η_{inj}) could be deduced with following equations.

$$\eta_{sep} = \frac{J^{Na_2SO_3}}{J_{abs}} \quad (5)$$

$$\eta_{inj} = \frac{J^{H_2O}}{J^{Na_2SO_3}} \quad (6)$$

Where J^{H2O} and J^{Na2SO3} are the photocurrent densities obtained in the electrolytes of 1 M NaOH and 1 M Na_2SO_3+1 M NaOH, respectively. The J_{abs} can be calculated by overlapping the UV–vis absorption spectrum and AM 1.5G solar spectrum according to the following equations.

$$J_{abs} = \int \frac{\lambda}{1240} \cdot \varphi\text{AM 1.5G}(\lambda) \cdot \text{LHE d}\lambda \quad (7)$$

$$\text{LHE} = 1 - 10^{-A(\lambda)} \quad (8)$$

Where λ is the wavelength (nm), φAM 1.5G(λ) represents the simulated solar spectral irradiance (W m^{-2} nm^{-1}), LHE is the light harvesting efficiency and A(λ) is the absorbance at wavelength λ.

According to the Mott–Schottky curves, the donor concentration (N_d) can be calculated from the following equation.

$$N_d = \frac{2}{e\varepsilon\varepsilon_0} \times \left[\frac{d\left[\frac{1}{C^2}\right]}{dV_s}\right]^{-1} \quad (9)$$

Where e (1.6×10^{-19} C) represents the electron charge, ε≈80 is the dielectric constant of α-Fe_2O_3, the vacuum permittivity (ε_0) is 8.854×10^{-14} F/cm, V denotes the applied potential on the photoanode and C is the space charge region's capacitance.

The measurement of gas evolution for the whole reaction system was conducting in a sealed reactor. The electrode with an area of 1 cm^2 was immersed in the electrolyte in a three-electrode configuration. Prior to the reaction and sealing processes, the electrolyte was purged with argon gas for 0.5 h. The generated O_2 and H_2 were analysed by injecting 0.5 mL gas into the gas chromatograph with a thermal conductivity detector (TCD) (Shimadzu GC-8AIT, argon carrier). Similarly, AM 1.5 G solar simulation (WXS-80C-3 AM 1.5 G) with a light intensity of 100 mW cm^{-2} was utilized as the light sources directly without adding any light filter.

4.3 Results and discussion

4.3.1 Characterization of the Ni-NC catalyst

The ultrathin Ni-NC was prepared via two steps. A supramolecular precursor was firstly carbonized under an inert atmosphere. After acid-leaching treatment, the obtained hierarchical sheets were then downsized into ultrathin nanosheets by ball milling treatment. The formation of graphitic carbon in Ni-NC during pyrolysis is confirmed by the X-ray diffraction (XRD) patterns and Raman spectra (Figure 4.1).[27] Atomic force

microscopy (AFM) image reveals that the as-prepared Ni-NC presents a two-dimensional (2D) structure with a planar size of ~100 nm and an ultrathin thickness of ~0.8 nm (Figure 4.2). The ultrathin 2D structure would make it easy to wrap onto the well crystalized α-Fe_2O_3 nanorods and then form an intimate interfacial heterostructure. No signals of Ni nanoparticles or clusters can be detected in Ni-NC by the measurements of scanning electron microscopy (SEM), transmission electron microscopy (TEM) and XRD (Figure 4.3a~4.3b and Figure 4.1a). The elemental mapping by TEM-EDS (energy-dispersive X-ray spectroscopy) (Figure 4.4) suggests the existence and uniform distribution of Ni sites and discloses that C, N and O elements disperse homogeneously on the ultrathin nanosheets. The dispersion of Ni atoms on the carbon nanosheets was further confirmed by atomic-resolution aberration-corrected high-angle annular dark-field scanning TEM (HAADF-STEM). As clearly displayed in Figure 4.3c, individual bright spots corresponding to isolated Ni sites (sizes of the spots are ~0.2 nm and the size distributions are shown in Figure 4.5) are well distributed across the carbon matrix.

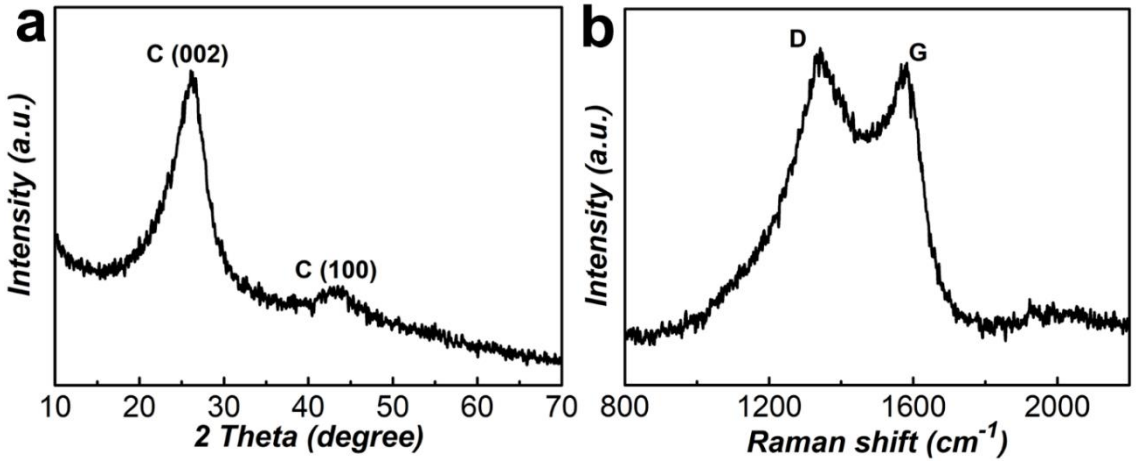

Figure 4.1. a) XRD pattern and b) Raman spectrum of Ni-NC. Note: XRD analysis of Ni-NC showed two distinct characteristic peaks at 26.1 ^{o} and 43.2^{o}, originating from the (002) and (100) planes of graphitic carbon. As shown in Figure 4.1b, the well-resolved D (1,330 cm^{-1}) and G (1,580 cm^{-1}) bands with an I_D/I_G ratio of 1.04 in Raman spectrum corroborated the graphitic nature of Ni-NC.[50]

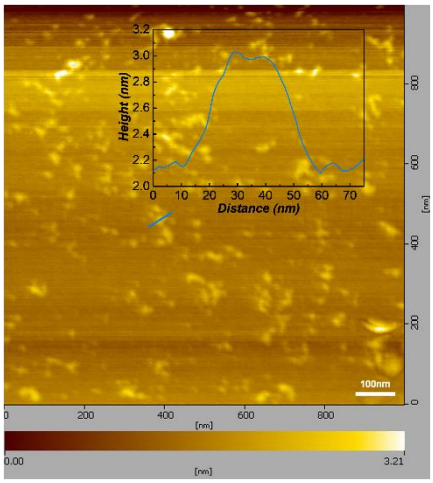

Figure 4.2 AFM image of ultrathin Ni-NC. Inset of AFM image shows the height profile along the blue line.

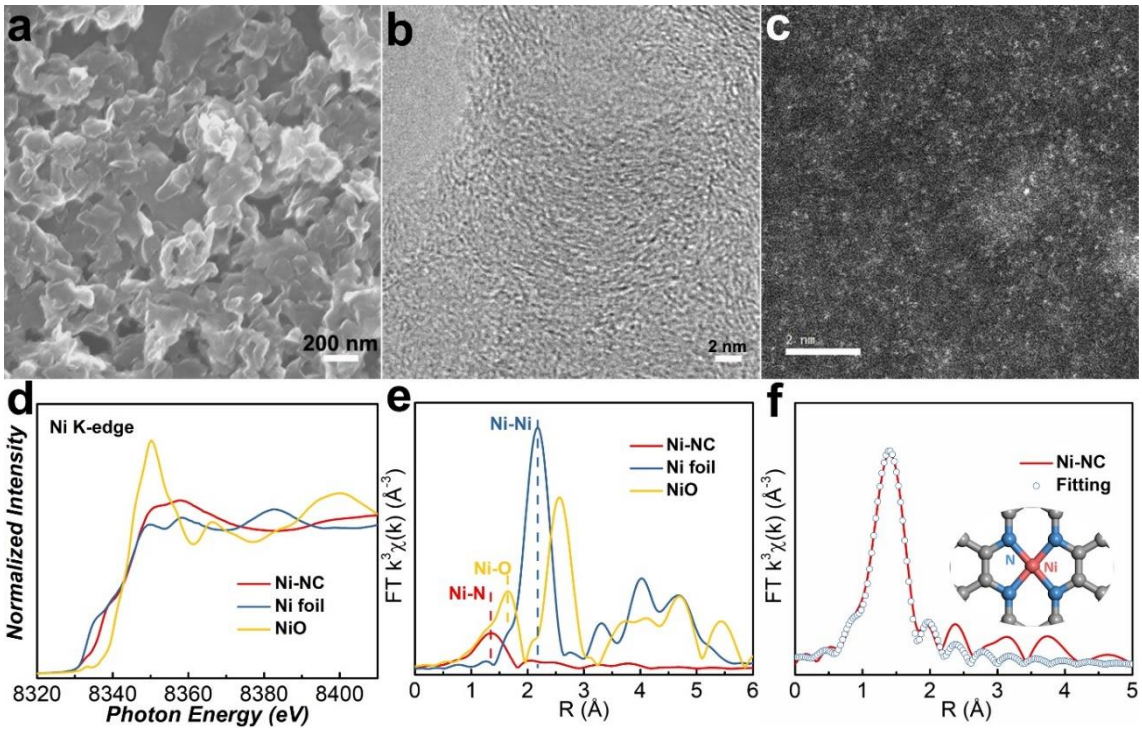

Figure 4.3 Morphology characterization and site coordination analysis of Ni-NC. a) SEM image, b) HRTEM image, c) aberration-corrected HAADF-STEM image, d) Ni K-edge XANES spectra of Ni-NC, Ni foil and NiO, e) Fourier transformed k3-weighted χ(k)-function of the EXAFS spectra for Ni K-edge, f) corresponding EXAFS fitting curve for Ni-NC.

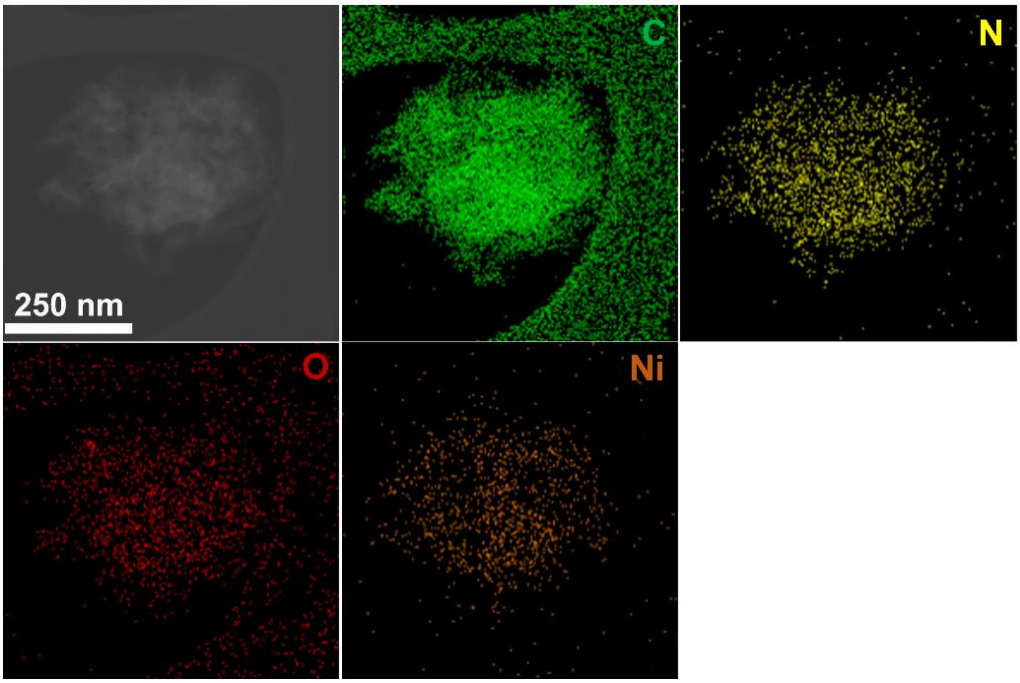

Figure 4.4 Elemental mapping of Ni-NC nanosheets confirming the co-existence of C, N, O and Ni.

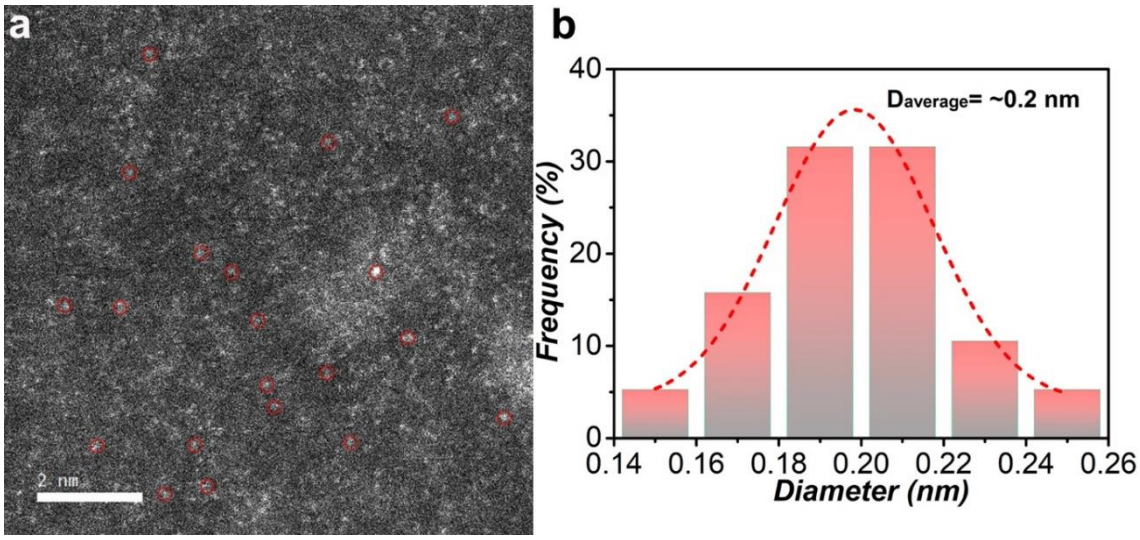

Figure 4.5 a) Aberration-corrected HAADF-STEM image of Ni-NC and b) size distributions of the isolated Ni sites. Note: 20 isolated Ni sites were randomly selected in Figure 4.5a (marked with red circles) and the statistical results in Figure 4.5b show that the average particle size of these isolated Ni sites is ~0.2 nm.

Then the X-ray photoelectron spectroscopy (XPS) measurement was utilized to investigate the chemical composition and elemental states of Ni-NC (Figure 4.6). The Ni *2p* spectrum of isolated Ni sites exhibits two main peaks assigned to Ni $2p_{3/2}$ (854.9 eV)

and Ni $2p_{1/2}$ (872.2 eV), along with the associated satellite features, which coincided well with the reported results that the valence of Ni species is located between Ni(0) and Ni(II) (Figure 4.6b).[33-34] The XPS spectrum of N *1s* in Figure 4.6a can be deconvoluted into pyridinic-N (398.4 eV), Ni-N_x (399.1 eV), pyrrolic-N (400.7 eV), graphitic-N (401.3 eV) and oxidized-N (402.5 eV).[35] The high-resolution C 1s and O 1s spectra in Figure 4.6c~4.6d confirm the existence of abundant oxygen-containing groups in Ni-NC. The oxidation state and local coordination configuration of the Ni atoms in the carbon nanosheets were further determined from the X-ray absorption fine structure (XAFS) measurement. As displayed in the X-ray absorption near-edge structure (XANES) spectra (Figure 4.3d), Ni-NC presents typical signals at 8340 eV ($1s \rightarrow 4p_z$ transition), 8350 eV ($1s \rightarrow 4p_{x,y}$) and 8358 eV ($1s \rightarrow 4p_{x,y}$), the same with that of previously reported single Ni-N dispersed carbon material and nickel phthalocyanine.[35] The appearance of these characteristic peaks originating from Ni-N species proves the existence of Ni-N species in Ni-NC. In addition, the absorption edge position of Ni-NC is located between those for the Ni foil and NiO, confirming again the unique electronic structure of $Ni^{\sigma+}$ ($0 < \sigma < 2$).[33] Figure 4.3e presents the analysis results of the extended X-ray absorption fine structure (EXAFS) spectra. A dominant peak at approximately 1.35 Å in the Ni-NC (shorter than the Ni-O signal at ~1.65 Å in NiO) can be attributed to the scattering interaction between the Ni atoms and N element (Ni-N). Additionally, the Ni-Ni peak at 2.17 Å is not existed in Ni-NC, further validating the atomic dispersed Ni sites on the carbon nanosheets. The coordination of Ni sites was further investigated by EXAFS curve fitting analysis (Figure 4.3f), which verified the Ni-N_4 structure of Ni-NC according to the fitting results (Table 4.1).

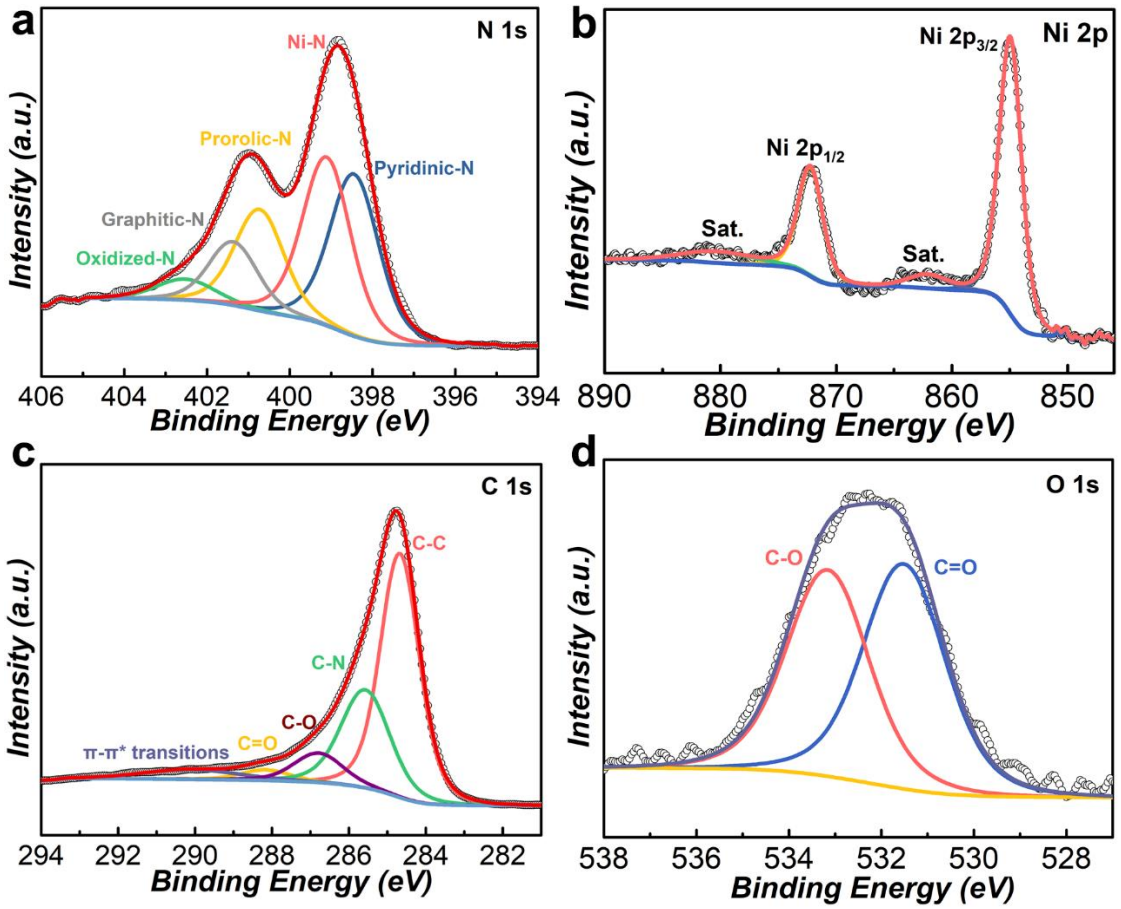

Figure 4.6 High-resolution XPS survey spectra of a) N *1s*, b) Ni *2p*, c) C *1s* and d) O *1s* in Ni-NC.

Table 4.1 Fitting EXAFS data for Ni foil and Ni-NC.

Sample	Path	C.N.	R (Å)	$\sigma^2\times10^3$ (Å^2)	ΔE (eV)	R factor
Ni foil	Ni-Ni	12*	2.48±0.01	6.0±0.2	7.0±0.5	0.001
Ni-NC	Ni-N	3.7±0.6	1.86±0.01	5.2±1.2	-7.5±2.3	0.006

*C.N.: coordination numbers; R: bond distance; σ^2: Debye-Waller factors; ΔE_0: the inner potential correction. R factor: goodness of fit. The obtained XAFS data was processed in Athena (version 0.9.25) for background, pre-edge line and post-edge line calibrations. Then Fourier transformed fitting was carried out in Artemis (version 0.9.25). The k^3 weighting, k-range of 2–10 Å^{-1} and R range of 1–2.2 Å for samples were used for the fitting. The four parameters, coordination number, bond length, Debye-Waller factor and E_0 shift (CN, R, σ^2, ΔE_0) were fitted without anyone was fixed, constrained, or correlated.

4.3.2 Characterization of the modified films with Ni-NC

The ultrathin Ni-NC was then loaded on the surface of α-Fe_2O_3 film. The fabrication processes of α-Fe_2O_3 and α-Fe_2O_3/Ni-NC films are depicted in Figure 4.7a. FeOOH nanorods were firstly deposited on the FTO substrate with a hydrothermal method and then transformed to α-Fe_2O_3 via a two-step calcination process (the morphology conversion of which is displayed in Figure 4.8). Subsequently, the Ni-NC was deposited on the surface of α-Fe_2O_3 by spin coating method, followed by annealing treatment to strengthen the interaction between α-Fe_2O_3 and Ni-NC. The α-Fe_2O_3-Ni-NC and α-Fe_2O_3-Ni-NC-300 signify the samples without and with optimized annealing treatment, respectively.

From the results of XRD patterns and UV–vis spectra in Figure 4.9, it can be deduced that the Ni-NC and annealing treatment at 300 ^oC have negligible effect on the structure and optical absorption property of α-Fe_2O_3 film. The obtained α-Fe_2O_3 film consists of numerous nanorods array with a one-dimensional wormlike structure and a thickness of approximately 350 nm (Figure 4.7b and Figure 4.11). The surface of bare α-Fe_2O_3 nanorods is relatively smooth according to the TEM images in Figure 4.10. After decorating with Ni-NC, it can be seen from the SEM and TEM images (marked with red arrows) that thin layers of Ni-NC are uniformly dispersed on the surface of α-Fe_2O_3 nanorods (Figure 4.7c~4.7d), indicating compact interaction between α-Fe_2O_3 and Ni-NC. More details can be obtained from the high-resolution TEM (HRTEM) image in Figure 4.7e, clearly displaying the formation of an intimate interfacial heterostructure with ultrathin Ni-NC compactly clinging to the well crystalized α-Fe_2O_3 nanorods. Such a tight contact between ultrathin Ni-NC and α-Fe_2O_3 can facilitate the fast charge transfer through the interface. The existence and distribution of C, N and Ni elements in the Fe_2O_3-Ni-NC-300 are also confirmed by the TEM-EDS elemental mappings in Figure 4.12.

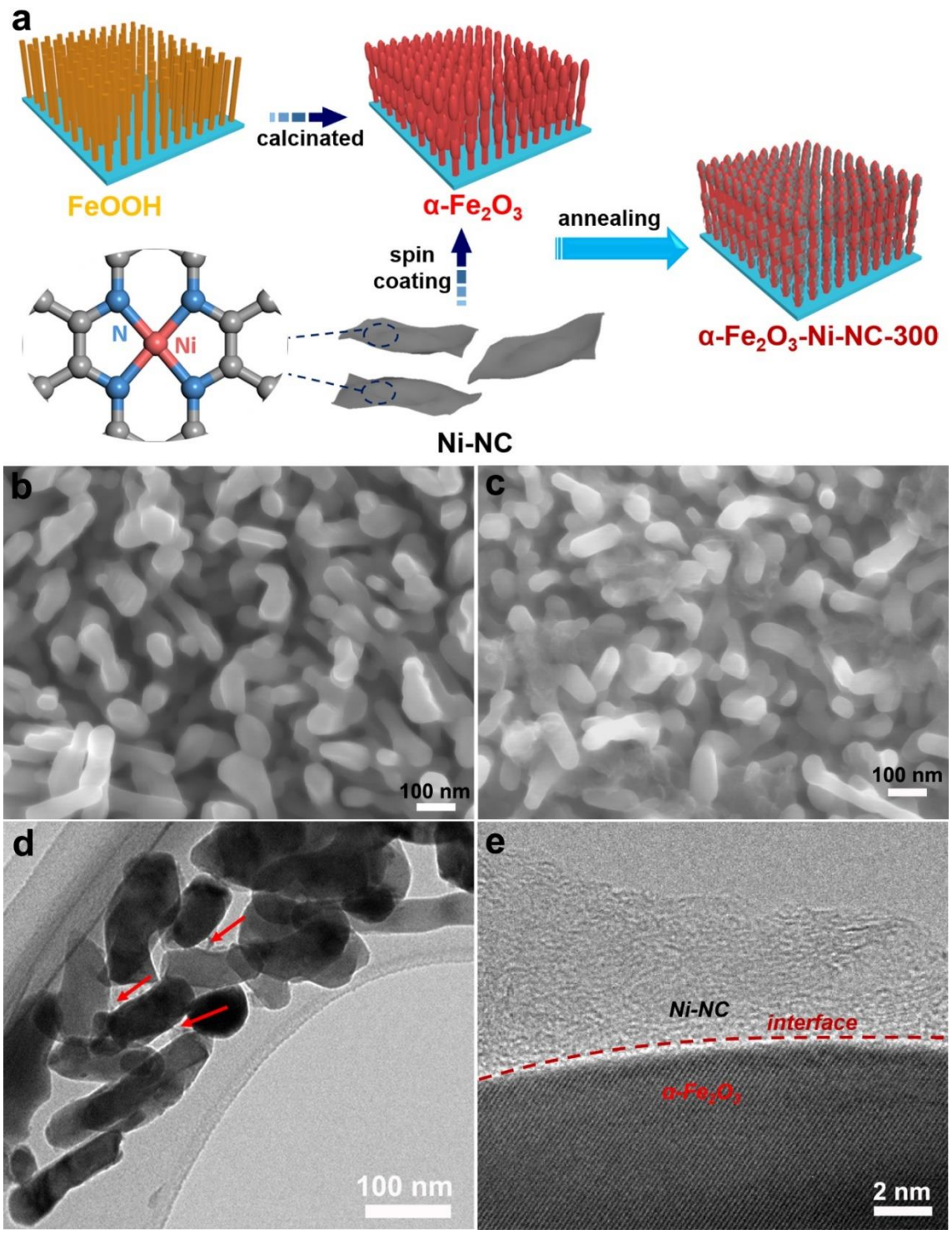

Figure 4.7 a) Scheme of fabrication procedures for α-Fe_2O_3 and α-Fe_2O_3-Ni-NC-300 films; top-view SEM images of b) bare α-Fe_2O_3, c) α-Fe_2O_3-Ni-NC-300; d) TEM image and e) HRTEM image of α-Fe_2O_3-Ni-NC-300.

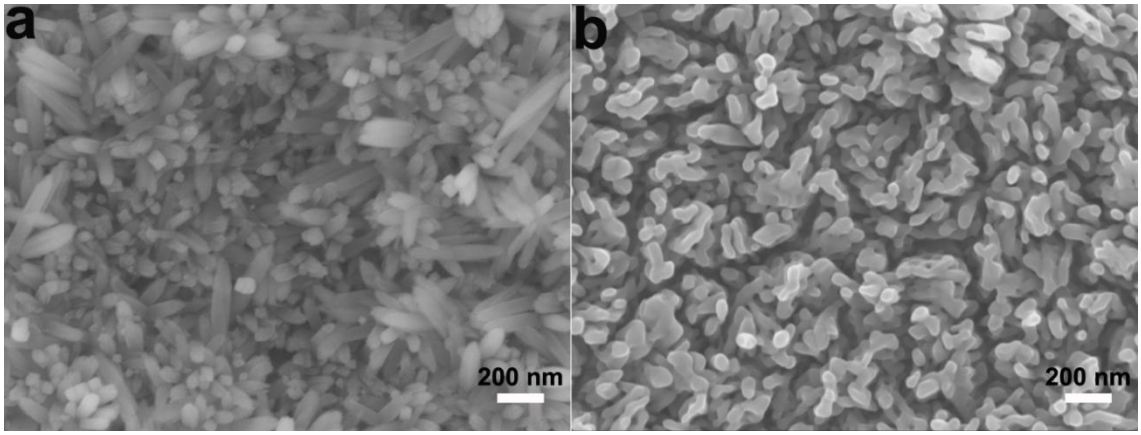

Figure 4.8 Top-view SEM images of a) FeOOH and b) α-Fe_2O_3 after calcinated at 550 ^oC.

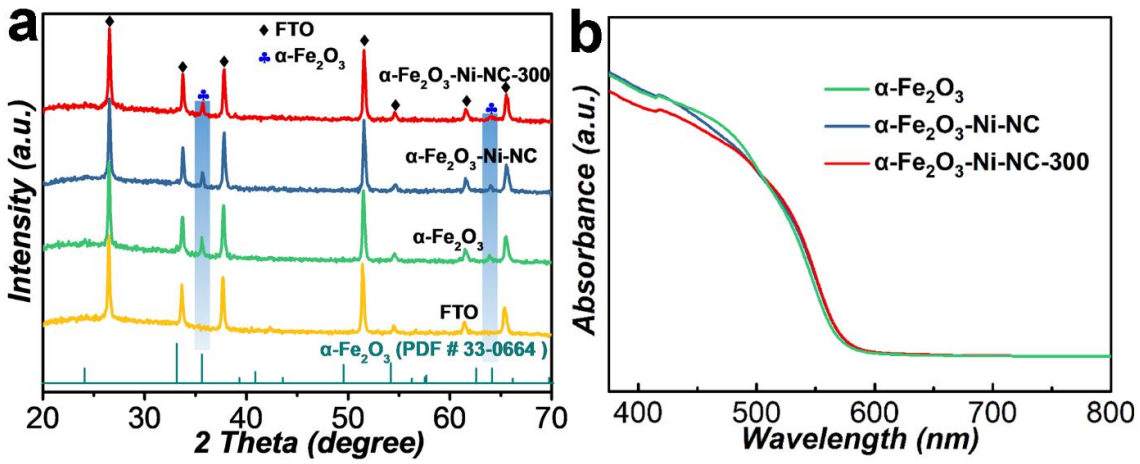

Figure 4.9 a) XRD patterns of α-Fe_2O_3-Ni-NC-300, α-Fe_2O_3-Ni-NC, α-Fe_2O_3 and FTO and b) UV–visible diffuse reflection spectra of α-Fe_2O_3-Ni-NC-300, α-Fe_2O_3-Ni-NC and α-Fe_2O_3.

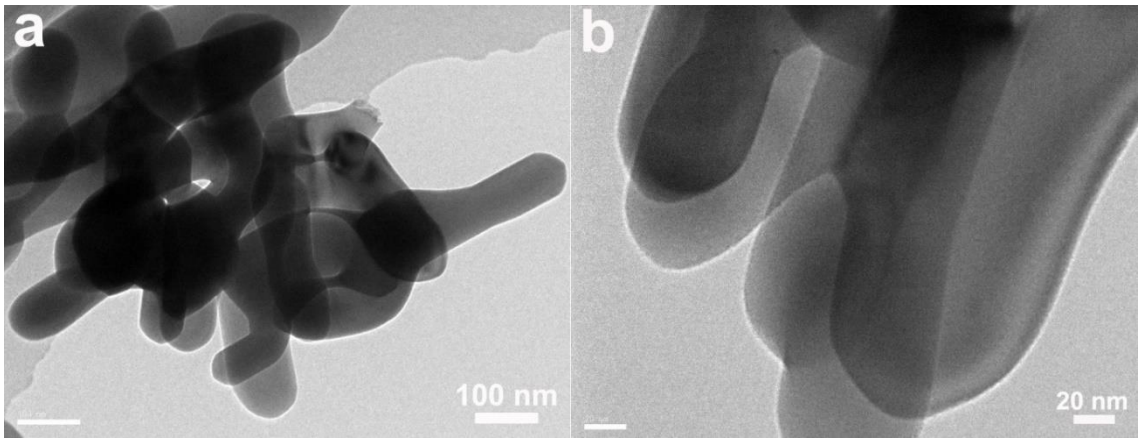

Figure 4.100 TEM images of pure α-Fe_2O_3 nanorods.

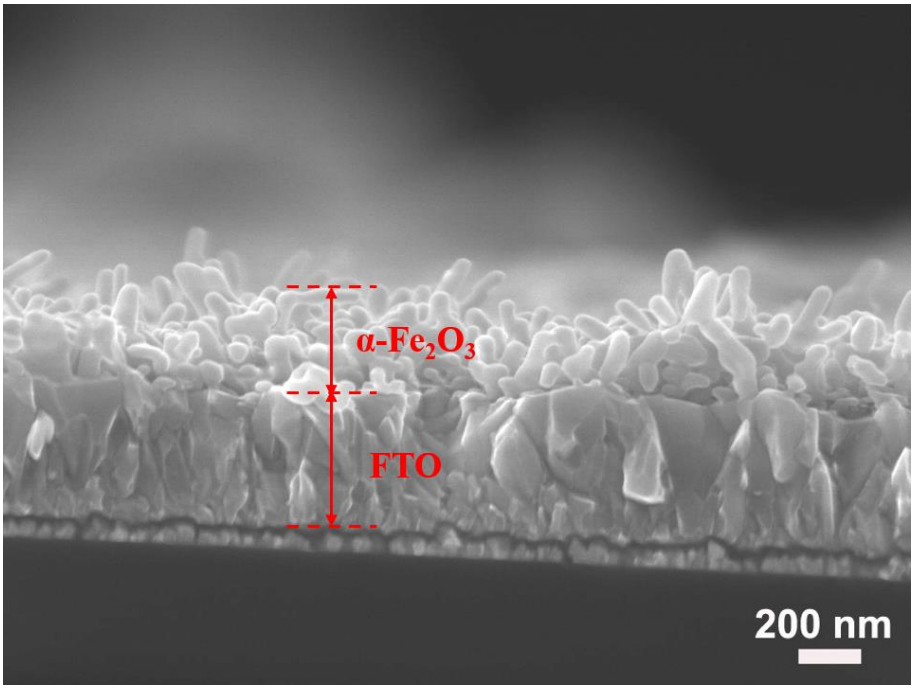

Figure 4.11 Cross-section SEM image of α-Fe_2O_3 nanorods.

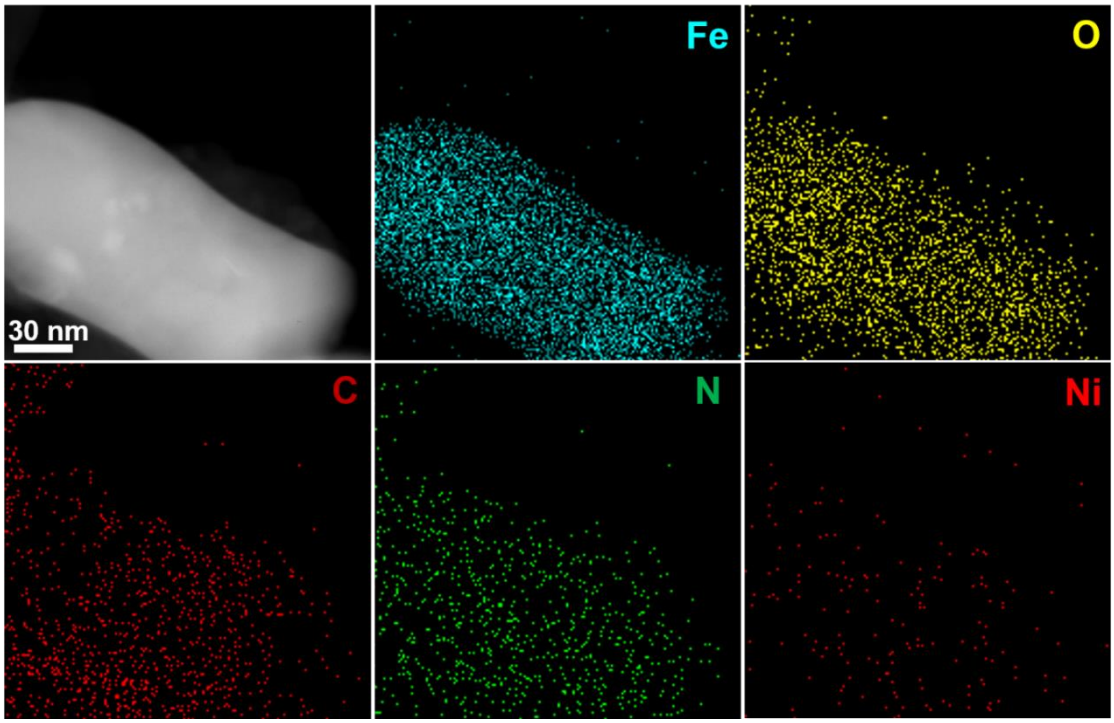

Figure 4.12 Elemental mapping of α-Fe_2O_3-Ni-NC, further confirming the decoration of Ni-NC on the surface of α-Fe_2O_3 nanorod.

4.3.3 PEC performance of different photoanodes

The PEC performance of different photoanodes was measured under AM 1.5 G irradiation with a standard three-electrode system in 1 M NaOH solution. As displayed in Figure 4.13a, the pristine α-Fe_2O_3 photoanode displays a low photocurrent density of 0.83 mA cm^{-2} at 1.23 V vs. RHE. With the direct deposition of Ni-NC, a slight enhancement (1.15 mA cm^{-2}), as a poor interaction between two phases of α-Fe_2O_3 and Ni-NC, is obtained for α-Fe_2O_3-Ni-NC photoanode. Interestingly, when the annealing method was utilized to reinforce this interaction, it is found that the annealing temperature is significantly affecting the catalytic activity for PEC water oxidation. The α-Fe_2O_3-Ni-NC-200 presents a photocurrent density of 1.33 mA cm^{-2} at 1.23 V vs. RHE, showing mild enhancement compared with α-Fe_2O_3-Ni-NC. Upon increasing the annealing temperature to 300 °C, the highest photocurrent density of 1.85 mA cm^{-2} at 1.23 V vs. RHE was attained, which is over two times than that of bare α-Fe_2O_3 and comparable to the recently reported results of hematite-based photoanodes (Table 4.2). However, further increasing the annealing temperature to 400 °C leads to a decrease of photocurrent density to 1.46 mA cm^{-2} at 1.23 V vs. RHE, which is attributed to the structure change with the appearance of photoelectrochemically inactive magnetite phase according to the XRD results (Figure 4.14).[36] This phenomenon signifies that the annealing treatment should have an additional impact on the photoanodes except for the reinforced contact between α-Fe_2O_3 and Ni-NC (will be discussed in more details later).

The significantly enhanced PEC performance of α-Fe_2O_3-Ni-NC-300 was further confirmed by the applied bias photon-to-current conversion efficiency (ABPE) (Figure 4.13b), incident photo-to-electron conversion efficiency (IPCE) (Figure 3.13c) and transient photocurrent measurements (Figure 4.13d). A maximum ABPE value of 0.18 % is obtained at 1.04 V vs. RHE by α-Fe_2O_3-Ni-NC-300. The IPCE value of α-Fe_2O_3-Ni-NC-300 demonstrates an integral triple increment compared with the bare α-Fe_2O_3 photoanode, achieving a maximum IPCE value of 30.4% at a wavelength of 360 nm. A sensitive photocurrent response, with the highest steady photocurrent density of 1.81 mA cm^{-2}, is achieved by α-Fe_2O_3-Ni-NC-300 photoanode, indicating the efficient transfer of photogenerated holes for the water oxidation with reduced recombination.[16] Intriguingly, the α-Fe_2O_3-Ni-NC-300 photoanode also exhibits an impressive stability over 15 h at 1.23 V vs. RHE under consecutive AM 1.5 G irradiation, still retaining approximately 90 % of the initial photocurrent density (Figure 4.15a). The yields of evolved H_2 and O_2 are

linear with respect to the irradiation time, with a stoichiometric ratio of ≈2:1 and a high Faradaic efficiency of 94.9% (Figure 4.15b). In brief, the remarkable PEC water oxidation activity of α-Fe_2O_3-Ni-NC-300 is owing to the robust single Ni sites (Figure 4.16 and relevant discussions) and optimized annealing treatment.

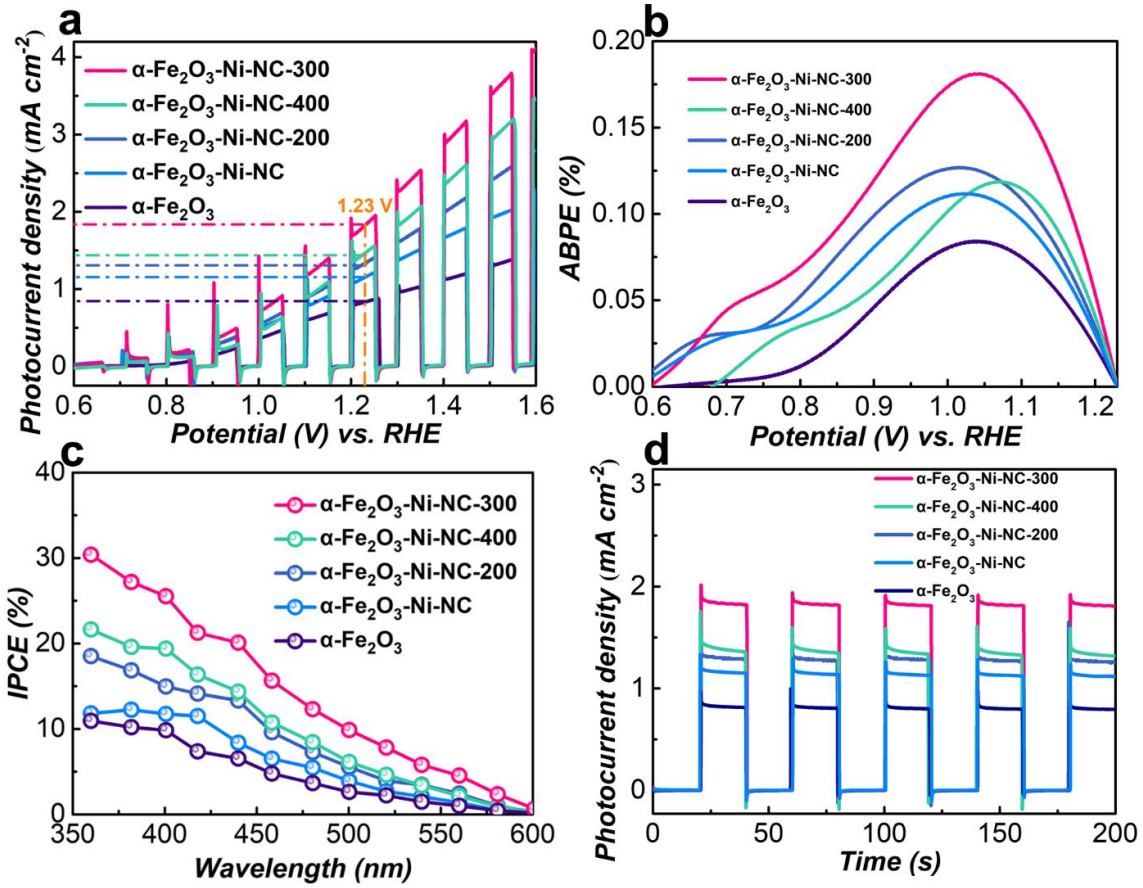

Figure 4.13 a) *J*–*V* curves, b) ABPE spectra, c) IPCE spectra and d) chopped current–time curves of bare α-Fe_2O_3, α-Fe_2O_3-Ni-NC, α-Fe_2O_3-Ni-NC-200, α-Fe_2O_3-Ni-NC-300 and α-Fe_2O_3-Ni-NC-400 photoanodes. The measurements of IPCE spectra and current–time curves were conducted at 1.23 V vs. RHE under AM 1.5 G illumination.

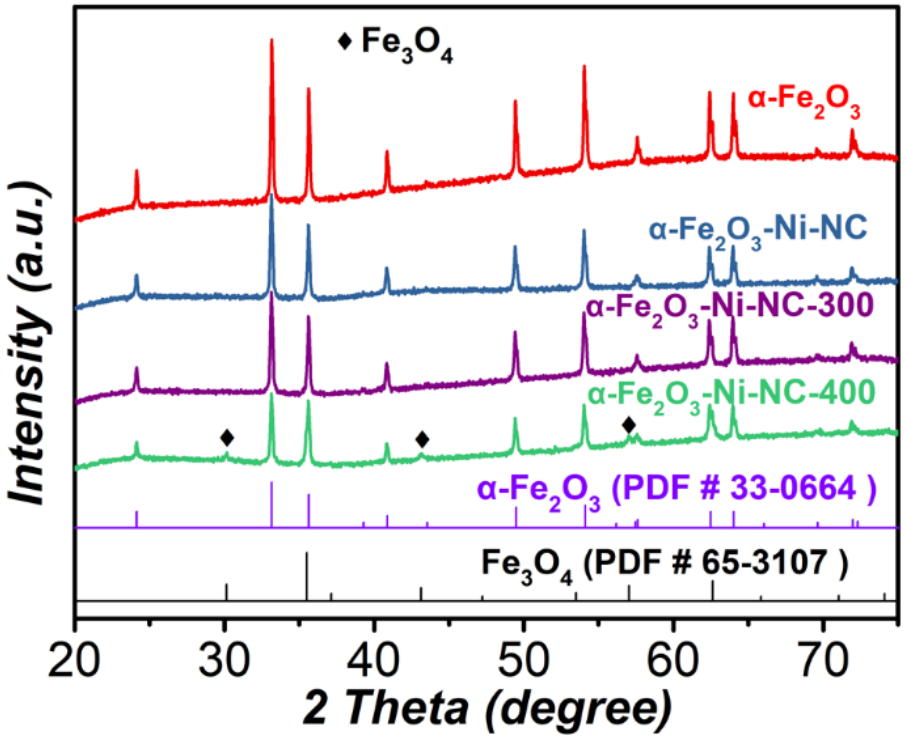

Figure 4.14 XRD patterns of α-Fe_2O_3, α-Fe_2O_3-Ni-NC, α-Fe_2O_3-Ni-NC-300 and α-Fe_2O_3-Ni-NC-400 powders. The standard diffraction peaks of α-Fe_2O_3 (hematite) and Fe_3O_4 (magnetite) are shown for reference.

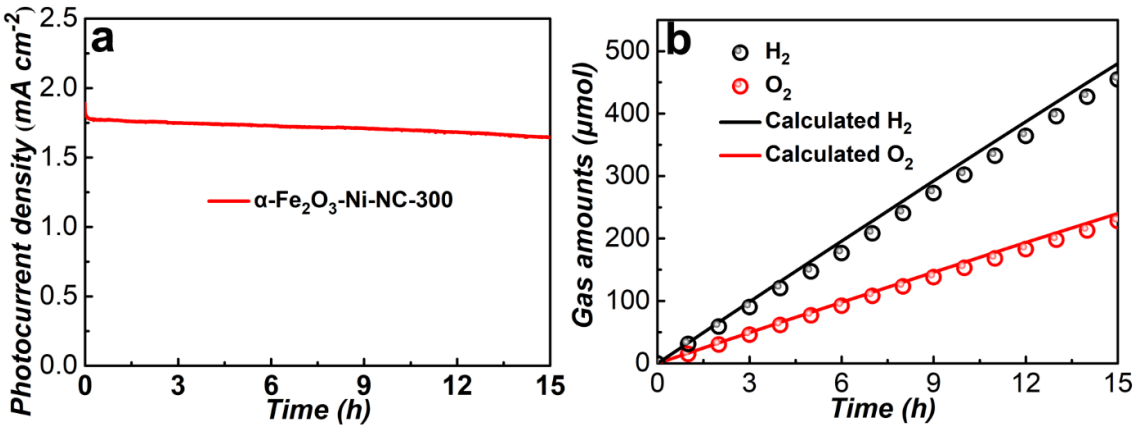

Figure 4.15 a) Stability test of α-Fe_2O_3 and α-Fe_2O_3-Ni-NC-300 photoanodes for 15 h. b) Gas evolution curves of α-Fe_2O_3-Ni-NC-300 photoanode under AM 1.5 G illumination at 1.23 V vs. RHE for 15 h.

Table 4.2 Comparison of our photoanode to other α-Fe_2O_3-based photoanodes in recent years.

Photoanodes	Current Density at 1.23 V vs. RHE (mA cm^{-2})	Stability	IPCE Value (%)
Ni:FeOOH/Fe_2O_3[48]	1.40	~5% decay after 10 h	38.6 at 1.23V (350 nm)
Zr-α-Fe_2O_3 NT[49]	1.50	No decay after 5 h	25.7 at 1.23V (370 nm)
Rh-F-Fe_2TiO_5/α-Fe_2O_3[50]	2.12	N.A.	37 at 1.25V (370 nm)
M:B-Fe_2O_3[51]	1.92	No decay after 18 h	35 at 1.50V (370 nm)
Fe_2TiO_5/Fe_2O_3/Pt[52]	1.00	N.A.	37 at 1.50V (340 nm)
TiO_2/Ti:Fe_2O_3 BNR[53]	2.50	~5% decay after 50 h	63 at 1.23 V (350 nm)
Co/E-I-Sn-α-Fe_2O_3[54]	2.2	~ 4% decay after 10 h	27 at 1.23V (330 nm)
α-Fe_2O_3/FeOOH[55]	1.21	~ 3% decay after 2.5 h	N.A.
α-Fe_2O_3/FeOOH[56]	0.85	4.4% decay after 70 h	20.2 at 1.23 V (400 nm)
α-Fe_2O_3/graphene[57]	1.64	No decay after 1 h	32 at 1.23 V (300 nm)
CDots/Co_3O_4-Fe_2O_3[58]	1.48	N.A.	28 at 1.23 V (370 nm)
C-Co-Ti-Fe_2O_3[59]	2.24	No decay after 2 h	40 at 1.23 V (370 nm)
S|NiNx−PC/EG/Fe_2O_3[60]	1.58	~ 5% decay after 3 h	30.9 at 1.23 V (300 nm)
α-Fe_2O_3-Ni-NC-300	**1.85**	**~10% decay after 15 h**	**30.4 at 1.23 V (360 nm)**

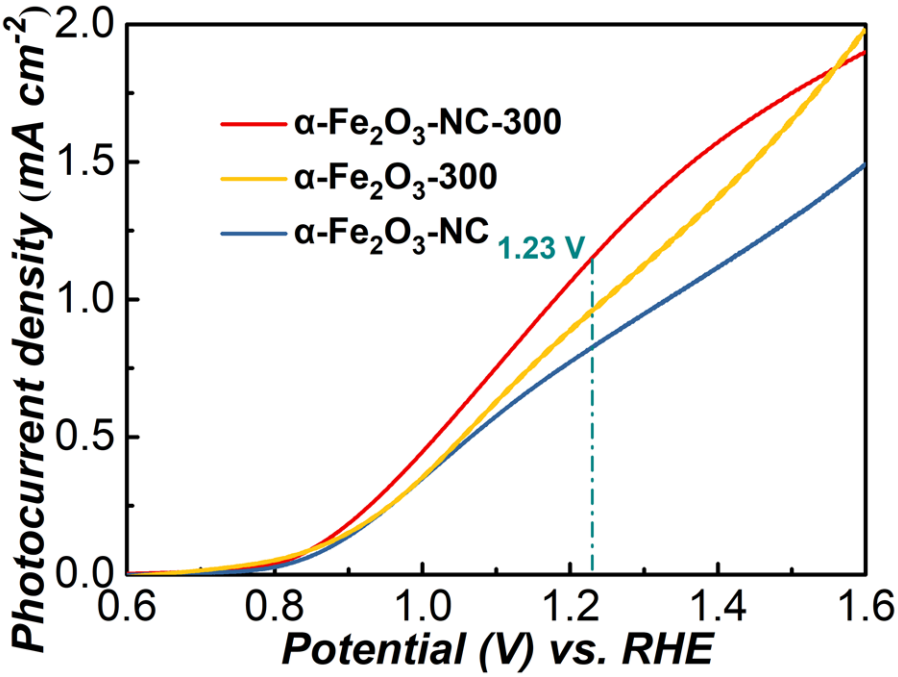

Figure 4.16 *J–V* curves of α-Fe_2O_3-NC-300, α-Fe_2O_3-300 and α-Fe_2O_3-NC. Note: The photocurrent density at 1.23 V vs. RHE of α-Fe_2O_3-NC without the Ni active sites keeps almost unchanged compared with the pure α-Fe_2O_3. After annealing at 300 °C, the photocurrent density at 1.23 V vs. RHE increases to 1.16 mA cm^{-2}. In addition, the α-Fe_2O_3-300 presents a photocurrent density of 0.95 mA cm^{-2} at 1.23 V vs. RHE. The slightly enhanced activity can be attributed to the generated oxygen defect induced by annealing in the inert atmosphere.

4.3.4 Research on catalytic mechanism

In order to understand the exact reason for the enhancement of water oxidation performance by the annealing process, the chemical composition and electronic structure of the samples were characterized by XPS measurement. The Fe *2p* spectrum of pristine α-Fe_2O_3 (Figure 4.19a) displays two distinct peaks of Fe $2p_{3/2}$ at 710.8 eV and Fe $2p_{1/2}$ at 724.5 eV with a satellite peak located at 718.8 eV, which is the typical feature of α-Fe_2O_3.[37-38] After annealing at 300 °C, the intensity of the signal at ~716.0 eV (corresponding to the satellite peak of Fe^{2+} species)[36, 39-40] slight increases in comparison to the bare α-Fe_2O_3 (Figure 4.17). These results suggest the generation of oxygen vacancies in α-Fe_2O_3 structure, which is further confirmed by analyzing the O *1s* spectra in Figure 4.18.[38] After the integration of α-Fe_2O_3 with Ni-NC, the binding energy of Fe *2p* in α-Fe_2O_3-Ni-NC keeps almost unchanged compared with the pure α-Fe_2O_3 (Figure 4.19a). In contrast, for the α-Fe_2O_3-Ni-NC-300 with annealing treatment, an interesting shift to lower binding energy, which can be attributed to the strong electron-donating behavior from Ni-NC to α-Fe_2O_3,[41-42] is observed in Fe *2p* spectra compared with the pristine α-Fe_2O_3. Additionally, the Fe *2p* peak intensity at around 716.0 eV of α-Fe_2O_3-Ni-NC-300 has almost no increase compared with the α-Fe_2O_3-Ni-NC from the spectra overlay in Figure 4.20, which is different from the result in Figure 4.17. This phenomenon indicates that most of the generated oxygen vacancies in the bulk of α-Fe_2O_3 during the annealing process are consumed with the introduction of Ni-NC.[41] This explanation is verified by the comparison of O *1s* XPS spectra of α-Fe_2O_3-Ni-NC and α-Fe_2O_3-Ni-NC-300. As shown in Figure 4.19b, owing to the oxygen-containing groups in the Ni-NC, the peak at ~532.6 eV (O_{III}) appears in the O *1s* spectra of both α-Fe_2O_3-Ni-NC and α-Fe_2O_3-Ni-NC-300, which is consistent with the O *1s* spectrum in Figure 4.6d. Interestingly, after annealing treatment, the peak intensity of O_{III} displays a obvious decrease and an extra peak appears at ~530.8 eV (O_{IV}). As the oxygen-containing groups in Ni-NC is stable

during the annealing process on the basis of Figure 4.21, the decreased intensity of O_{III} can be attributed to the consumption by filling into the oxygen vacancies.[41-42] Therefore, the additional signal of O_{IV} is deduced to be the Fe−O−C at the interfaces of α-Fe_2O_3 and Ni-NC, which can also be validated according to the results in previous reports that the binding energy of O *1s* in Fe−O−C bond is about 1~3 eV higher than the Fe−O.[30, 43] In this regard, the variation of the O *1s* spectrum in α-Fe_2O_3-Ni-NC-300 can be ascribed to the chemical interaction between the Ni-NC and α-Fe_2O_3 due to the patching effect between oxygen-containing groups in the Ni-NC and the oxygen vacancies. This elucidation can be further verified by the performance test and chemical compositions of α-Fe_2O_3-Ni-NC annealed at 300 °C in the air (α-Fe_2O_3-Ni-NC-300-air) in Figure 4.22~4.23. As shown in Figure 4.22, the α-Fe_2O_3-Ni-NC-300-air displays a photocurrent density of 1.31 mA cm^{-2} at 1.23 V vs. RHE, which is much lower than the α-Fe_2O_3-Ni-NC-300 (1.85 mA cm^{-2} at 1.23 V vs. RHE). In this case, the annealed α-Fe_2O_3-Ni-NC in the air is much different from that in the Ar gas. In order to further confirm the variation of chemical compositions on the surface of α-Fe_2O_3-Ni-NC after annealing in the air, XPS measurement was conducted. As shown in Figure 4.23, no obvious difference can be observed from the overlap of Fe *2p* and O *1s* XPS spectra before and after annealing in the air, signifying that chemical interaction between α-Fe_2O_3 and Ni-NC did not occur during the annealing processes in the air.

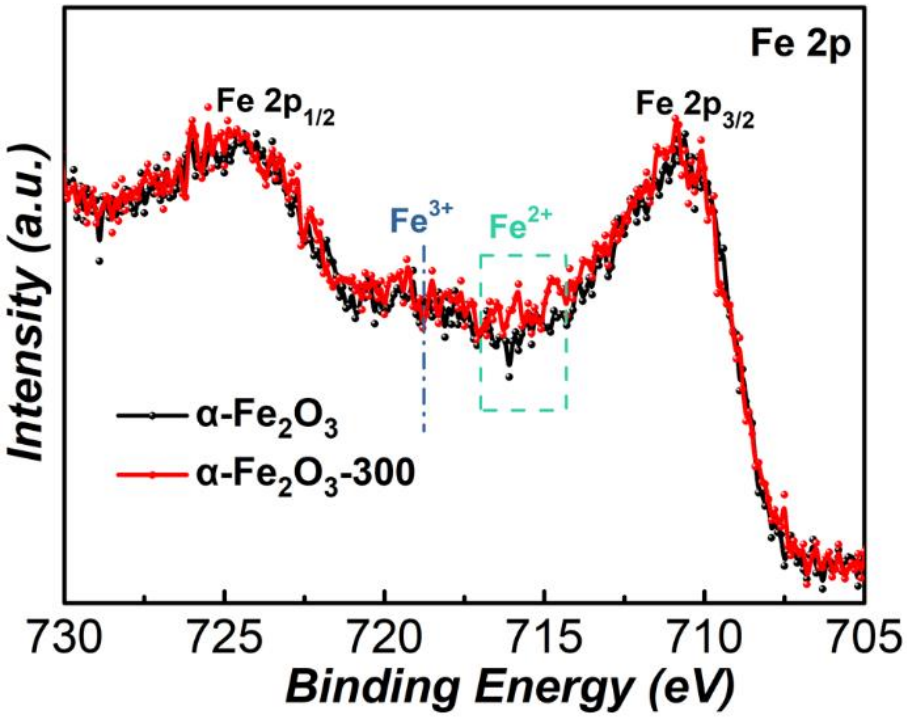

Figure 4.17 Overlay of Fe *2p* XPS spectra of α-Fe_2O_3 and α-Fe_2O_3-300 samples. The vertical dashed lines highlight the satellite peaks for Fe^{3+} and Fe^{2+} species.

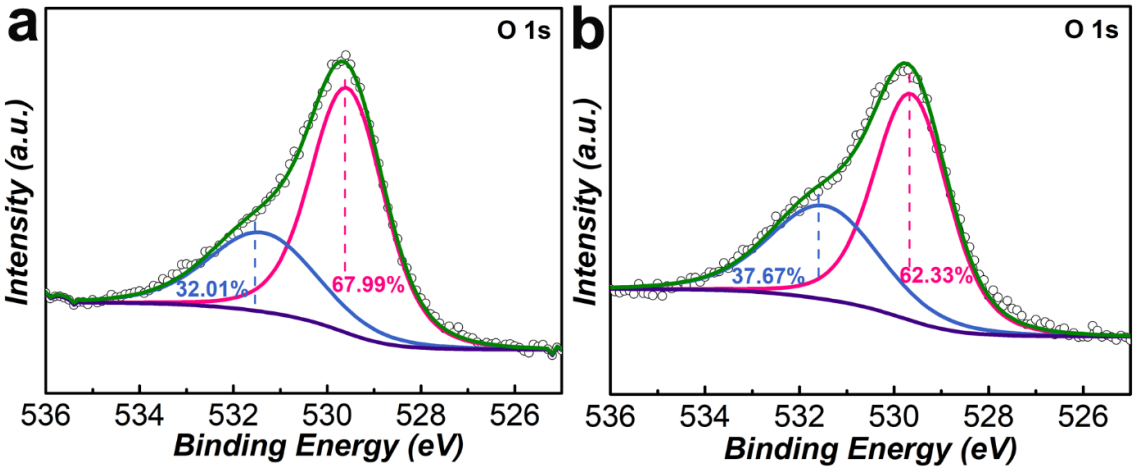

Figure 4.18 O *1s* XPS spectra of a) α-Fe_2O_3 and b) α-Fe_2O_3-300.

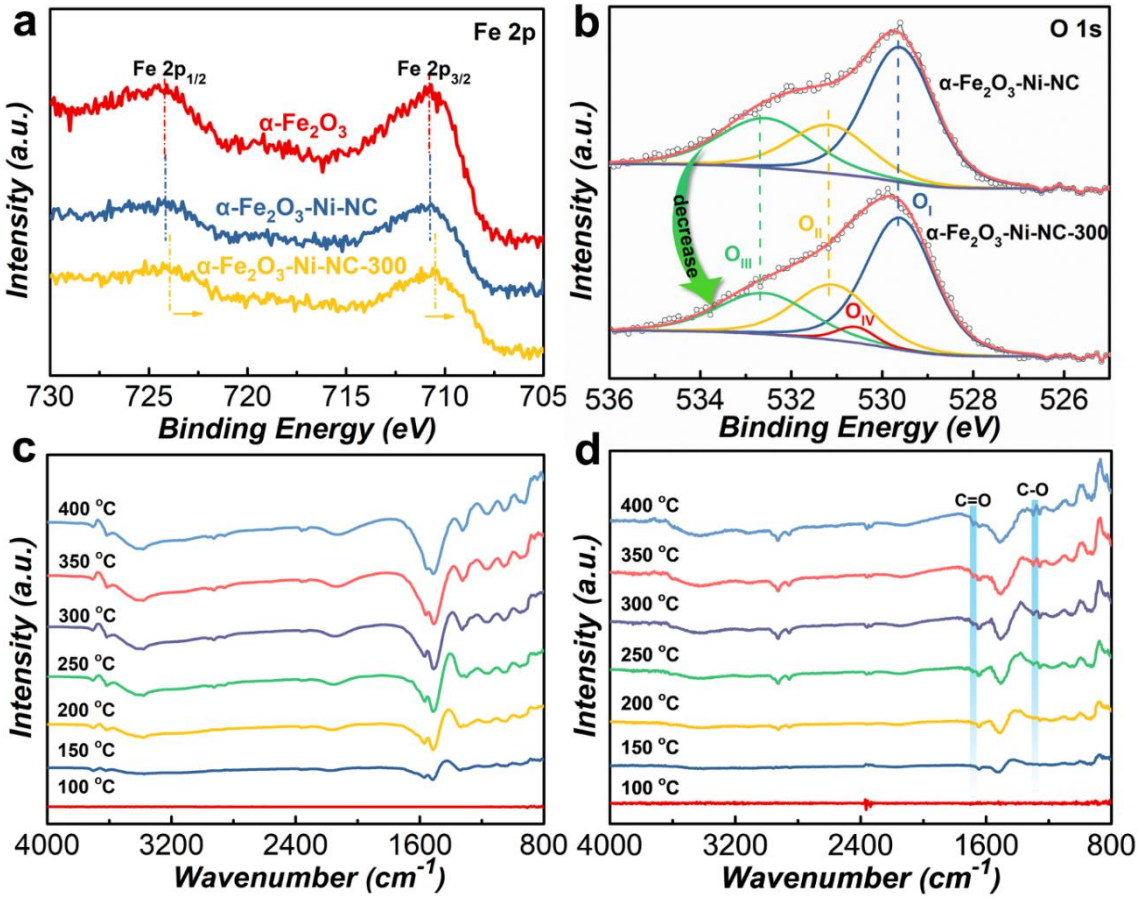

Figure 4.19 a) Fe *2p* XPS spectra of α-Fe_2O_3, α-Fe_2O_3-Ni-NC and α-Fe_2O_3-Ni-NC-300, b) O *1s* XPS spectra of α-Fe_2O_3-Ni-NC and α-Fe_2O_3-Ni-NC-300 (O_I: the lattice oxygen bonded with Fe; O_{II}: the defect sites with a low oxygen coordination; O_{III}: the oxygen-

containing groups in Ni-NC; O_{IV}: the newly formed Fe–O–C bond), in situ FT-IR spectra of c) α-Fe_2O_3 and d) α-Fe_2O_3-Ni-NC measured under increased temperature.

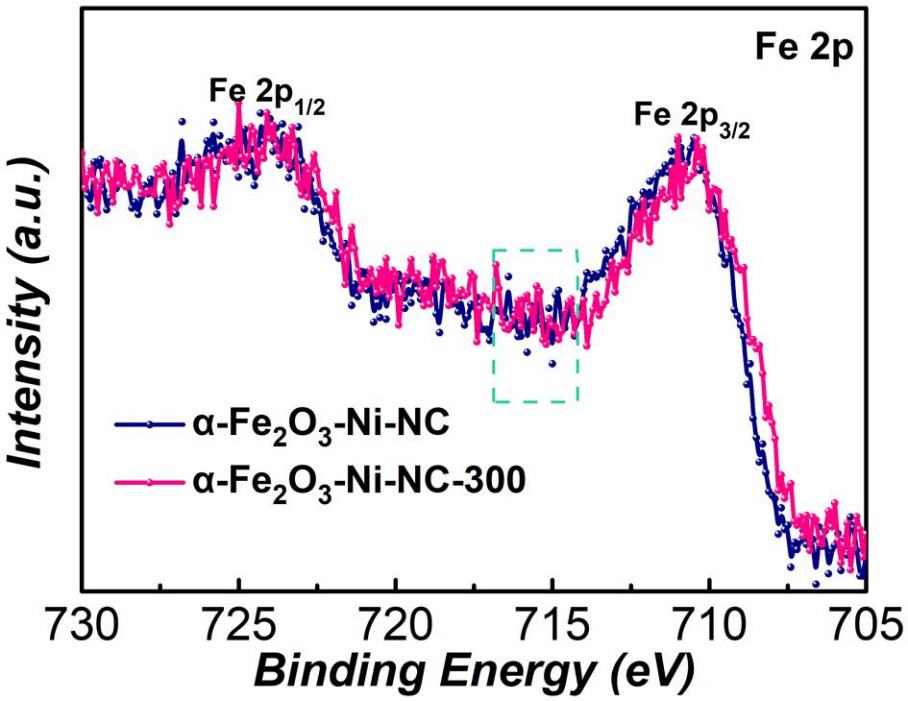

Figure 4.20 Overlay of Fe *2p* XPS spectra of α-Fe_2O_3-Ni-NC and α-Fe_2O_3-Ni-NC-300 samples. The dashed lines highlight the position of satellite peak for Fe^{2+} species.

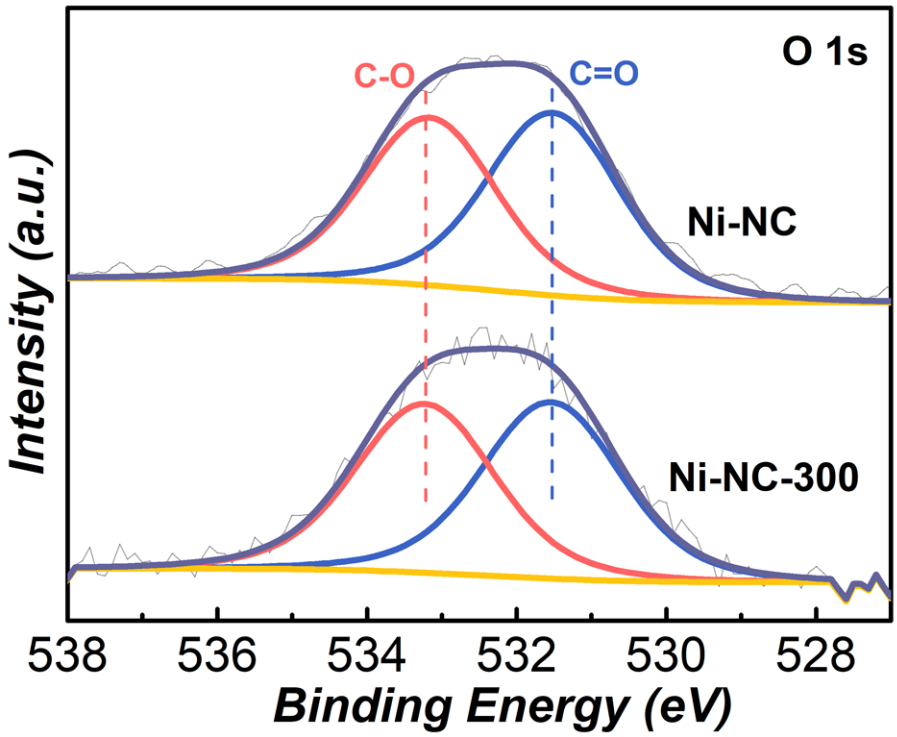

Figure 4.21 The comparison of O *1s* XPS spectra before and after annealing at 300 °C.

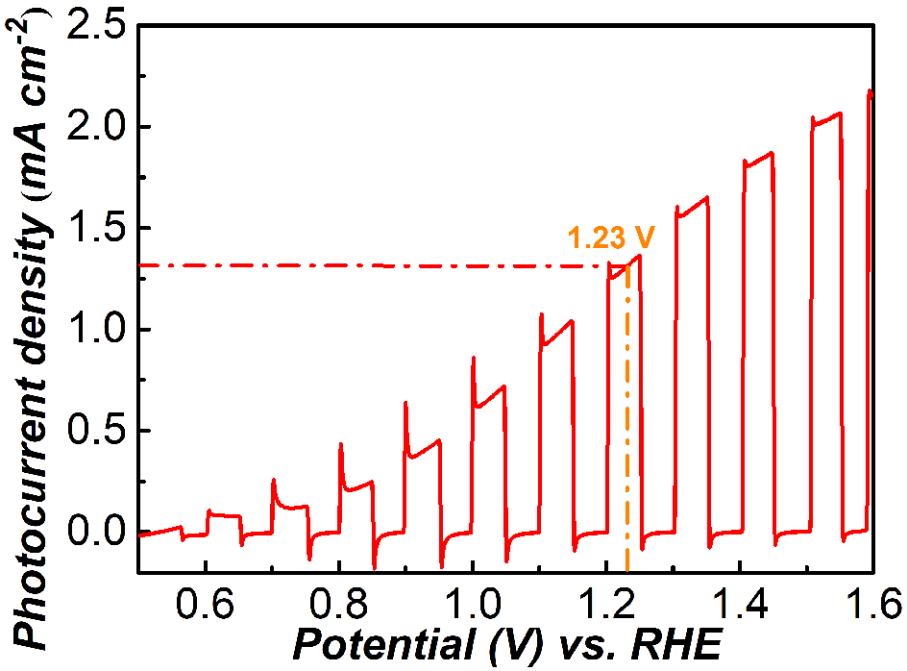

Figure 4.22 *J–V* curve of α-Fe_2O_3-Ni-NC-300-air photoanode under AM 1.5 G illumination.

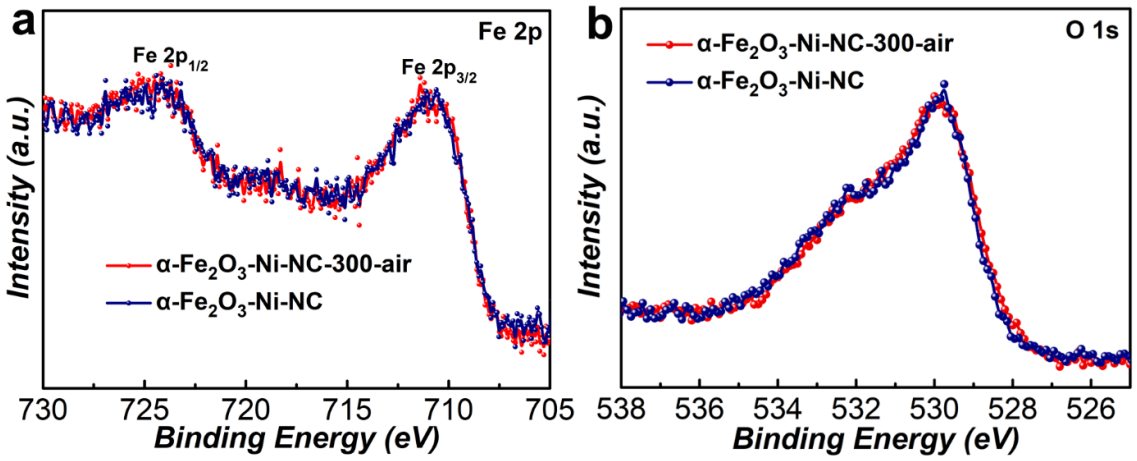

Figure 4.23 Overlay of a) Fe *2p* and b) O *1s* XPS spectra of α-Fe_2O_3-Ni-NC and α-Fe_2O_3-Ni-NC-300-air.

To further investigate the interfacial structure and interaction evolution in α-Fe_2O_3-Ni-NC with annealing, in situ Fourier transform infrared spectroscopy (FT-IR) experiment was conducted in argon atmosphere at gradually increased temperatures, in which the samples were measured and the signal detected at 100 ^oC was used as the background. As shown in Figure 4.19c, the calcination-time dependent infrared spectra of pure α-Fe_2O_3 present gradually decreased absorbance with elevated temperature. This phenomenon may be attributed to the decomposition and desorption of the adventitious carbon and

water, which were absorbed on the surface during the preparation process or from the air.[44-45] After integrating α-Fe_2O_3 with Ni-NC, the calcination-time dependent infrared spectra (Figure 4.19d) of α-Fe_2O_3-Ni-NC display a similar tendency for the gradually decreased absorbance. However, an obvious signal shows gradually decreased absorbance at ~1690 cm^{-1}, which is attributed to the stretch of C=O bond. According to the O *1s* XPS spectrum of Ni-NC, this C=O signal is ascribed to the oxygen-containing groups in Ni-NC. As correlated with this, a gradually increased absorbance at ~1270 cm^{-1} is observed, which indicates the progressive formation of C–O bond with the elevated temperature. Intriguingly, the in situ FT-IR spectra of bulk Ni-NC (Figure 4.24) do not show any obvious change with the increasing temperature. In this case, the variation of the signals of C=O and C–O groups should originate from the chemical interaction at the interfaces between α-Fe_2O_3 and Ni-NC, which is consistent with the XPS results.

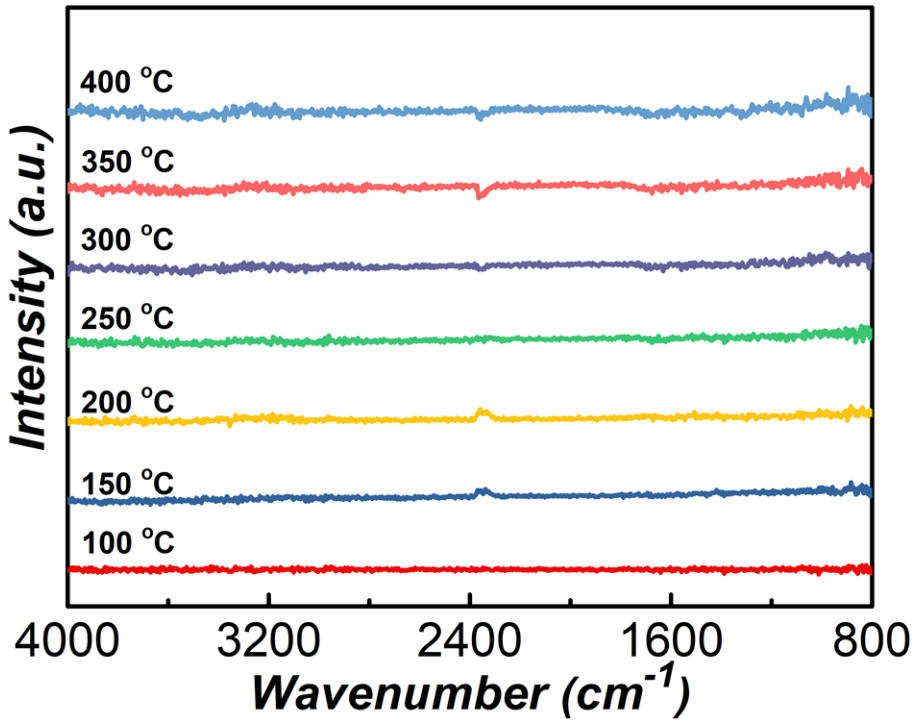

Figure 4.24 In situ FT-IR spectra of bare Ni-NC measured at increased temperature.

As identified by XPS and in situ FT-IR analysis, the newly formed bond is induced by chemical interaction at the interface of α-Fe_2O_3 and Ni-NC during the annealing process, which may act as the fast charge transfer channels. In order to understand and confirm the underlying mechanism of this interaction for the performance enhancement, kinetics of photocarriers in different photoanodes were studied by several electrochemical measurements. To verify the effect of Ni-NC and annealing process on the charge transfer

behaviors, the charge separation efficiency (η_{sep}) and surface charge injection efficiency (η_{inj}) were measured and quantified by using Na_2SO_3 as a hole scavenger (Figure 4.25a). As shown in Figure 4.26a and Figure 4.26b, the α-Fe_2O_3-Ni-NC-300 achieves η_{sep} of 28.1% at 1.23 V vs. RHE according to the integrated current density (J_{abs}) (Figure 4.25b), which is much higher than those of α-Fe_2O_3-Ni-NC (19.6%) and bare α-Fe_2O_3 (16.5%). These results indicate that the improved separation efficiency of α-Fe_2O_3-Ni-NC-300 is mainly attributed to the chemical interaction between α-Fe_2O_3 and Ni-NC. Additionally, the above tendency can also be obtained for η_{inj} over α-Fe_2O_3-Ni-NC-300, with the highest η_{inj} value of 64.8% at 1.23 vs. RHE. The above results verify that the chemical interaction between α-Fe_2O_3 and Ni-NC can reduce the charge recombination and facilitate the charge separation in the photoanode.

The charge transfer processes in different photoanodes were then visualized by electrochemical impedance spectroscopy (EIS) under illumination at 1.23 V vs. RHE (Figure 4.26c). The typical Nyquist plots of different photoanodes were fitted by the equivalent circuit model (inserted in Figure 4.26c). All the simulated parameters are summarized in Table 4.3, in which the similar series resistances (R_s) indicating the working conditions for the photoanodes are almost identical. Furthermore, the resistances in the semiconductor (R_{bulk}) for photoanodes of α-Fe_2O_3-Ni-NC (125.3 Ω) and α-Fe_2O_3-Ni-NC-300 (96.6 Ω) are both lower than the bare α-Fe_2O_3 (131.2 Ω), suggesting the enhanced charge mobility due to the increased carrier density by the incorporation of carbon nanosheets. The values of carrier density (N_d) are calculated from the slope of Mott-Schottky curves (Figure 4.27), manifesting the n-type semiconductor feature of all samples. As shown in Table 4.3, the N_d values are promoted from 1.12×10^{20} cm^{-3} of bare α-Fe_2O_3 to 9.19×10^{20} cm^{-3} of α-Fe_2O_3-Ni-NC-300, demonstrating the enhanced conductivity and facilitated charge transfer processes in the semiconductor. Additionally, the charge transfer resistance at the photoanode/electrolyte interface (R_{ct}) presents a dramatical decrease, which varied from 334.6 Ω of pure α-Fe_2O_3 to 184.4 Ω of α-Fe_2O_3-Ni-NC-300, signifying the enahced injection efficiency of photogenerated holes into electrolyte on α-Fe_2O_3-Ni-NC-300 photoanode.

To further elucidate the charge carrier dynamics of the photoanodes, room-temperature photoluminescence (PL) and time-resolved transient photoluminescence delay (TRPL) measurements were performed. Figure 4.28 depicts that all the samples exhibit a narrow emission band centered at ~675 nm. The α-Fe_2O_3-Ni-NC-300 displays the lowest PL

intensity than the other two samples, indicating the reduced recombination and fastest separation of photogenerated charge carriers.[46] From the analysis of TRPL spectra in Figure 4.26d, the average carrier life-time of α-Fe_2O_3 is calculated to be 2.33 ns (Table 4.4), which is consistent with the property of short photocarriers life-time. Meanwhile, the α-Fe_2O_3-Ni-NC-300 displays a much longer lifetime of 4.41 ns compared with bare α-Fe_2O_3 and α-Fe_2O_3-Ni-NC, further manifesting enhanced charge transfer efficiency and decreased recombination rate.[47]

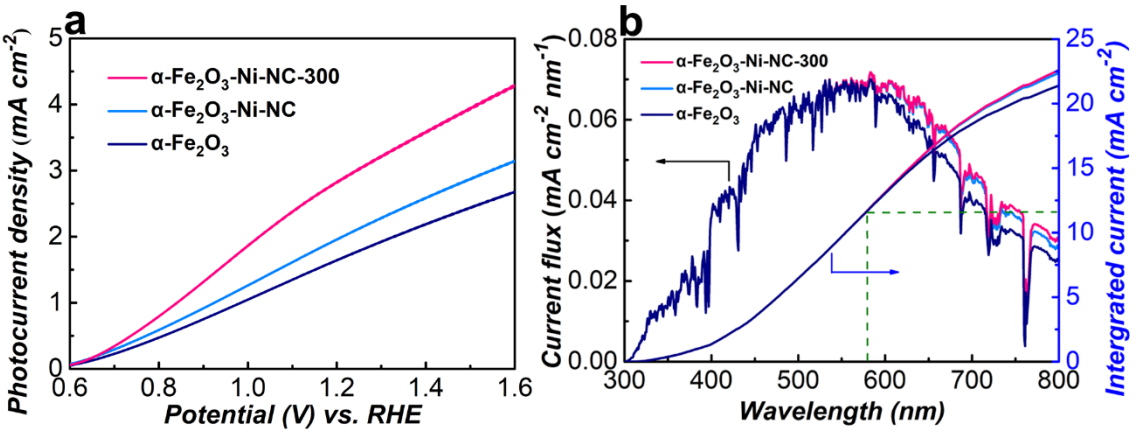

Figure 4.25 a) *J–V* curves of pristine α-Fe_2O_3, α-Fe_2O_3-Ni-NC and α-Fe_2O_3-Ni-NC-300 with Na_2SO_3 as the hole scavenger; b) The calculated current density flux and integrated current density (J_{abs}) of α-Fe_2O_3, α-Fe_2O_3-Ni-NC and α-Fe_2O_3-Ni-NC-300 photoanodes.

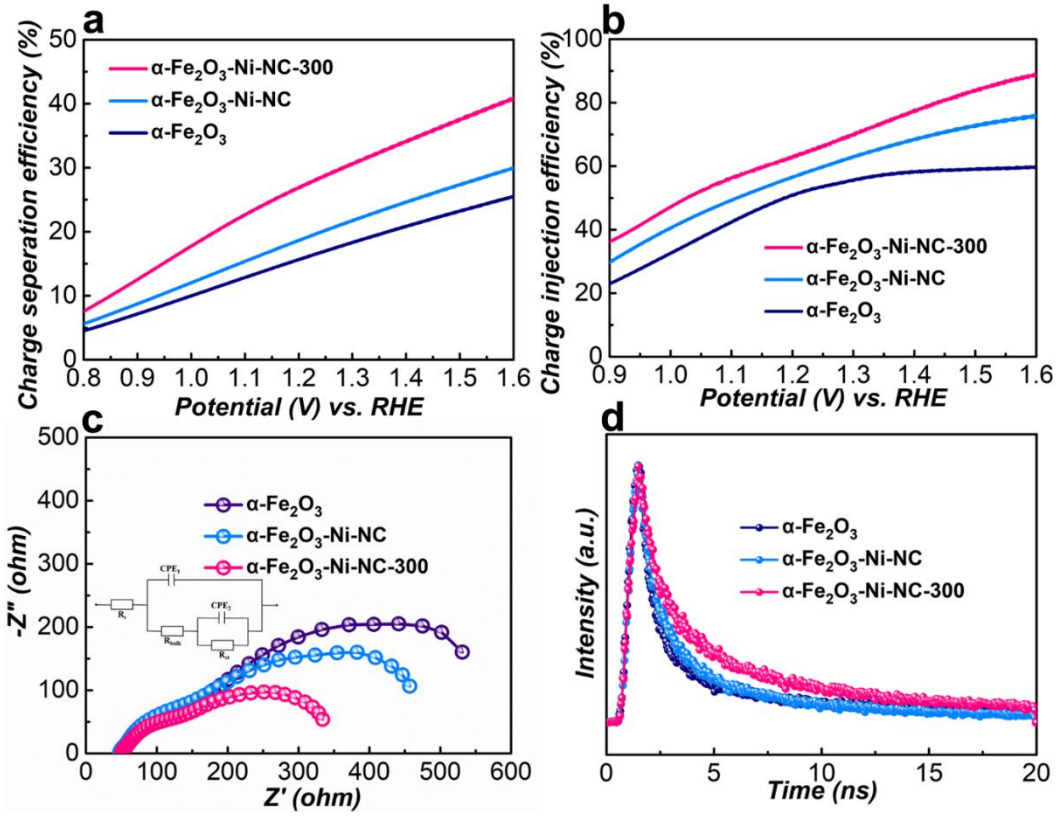

Figure 4.26 a) Bulk charge separation efficiencies, b) Surface charge injection efficiencies on the surface, c) EIS plots and d) time-resolved PL spectra of bare α-Fe_2O_3, α-Fe_2O_3-Ni-NC and α-Fe_2O_3-Ni-NC-300 photoanodes.

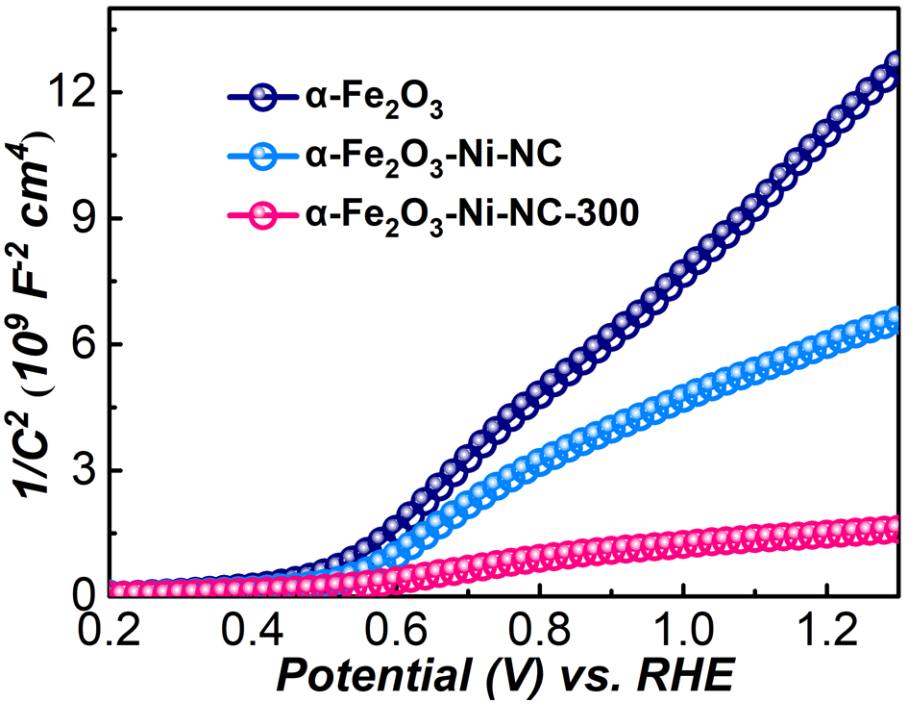

Figure 4.27 Mott–Schottky plots of α-Fe_2O_3, α-Fe_2O_3-Ni-NC and α-Fe_2O_3-Ni-NC-300.

Table 4.3 EIS results of different photoanodes calculated by the equivalent circuit model and carrier densities obtained from Mott-Schottky plots.

Photoanode	R_s (Ω)	R_{bulk} (Ω)	R_{ct} (Ω)	Carrier Density (cm^{-3})
α-Fe_2O_3	52.9	131.2	334.6	1.12×10^{20}
α-Fe_2O_3-Ni-NC	50.6	125.3	297.3	2.01×10^{20}
α-Fe_2O_3-Ni-NC-300	53.1	96.6	184.4	9.19×10^{20}

Table 4.1 Kinetic parameters for the TRPL decay curves.

Sample	A_1	τ_1 (ns)	A_1	τ_2 (ns)	$\tau_{average}$ (ns)
α-Fe_2O_3	1433.18	0.48	643.93	3.00	2.33
α-Fe_2O_3-Ni-NC	1479.63	0.67	721.22	3.90	3.06
α-Fe_2O_3-Ni-NC-300	1177.35	0.81	842.79	5.21	4.41

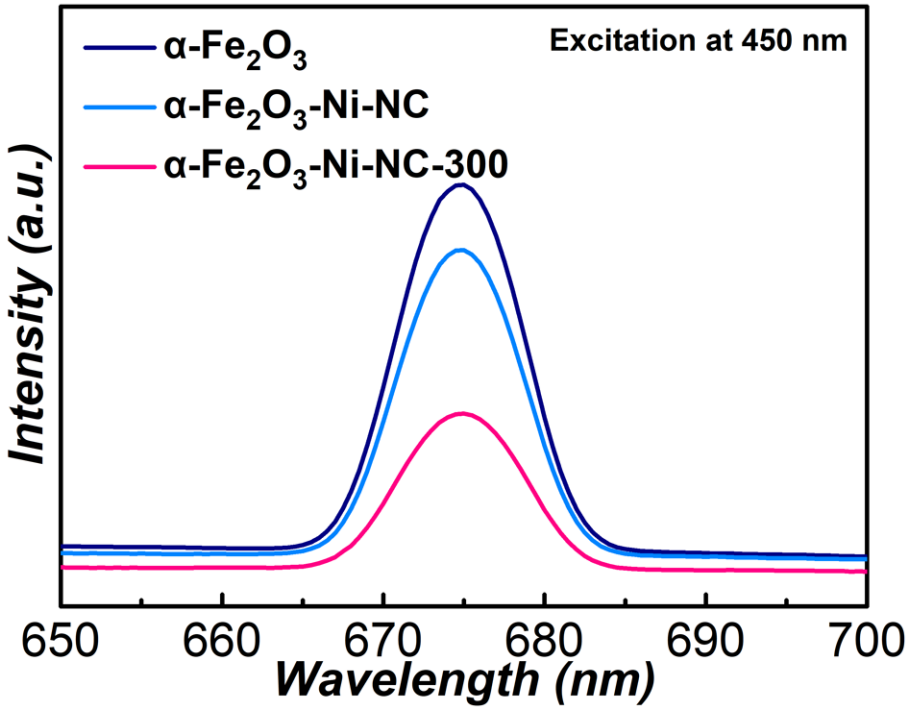

Figure 4.28 Steady-state PL spectra of α-Fe_2O_3, α-Fe_2O_3-Ni-NC and α-Fe_2O_3-Ni-NC-300.

According to the above results and discussion, a possible mechanism was proposed for the construction of chemical interaction between α-Fe_2O_3 and Ni-NC. As shown in Scheme 4.1a, without annealing treatment, the interaction between α-Fe_2O_3 and Ni-NC is physical adsorption, leading to a slow charge transfer at the interface. During the annealing process, oxygen vacancies would be generated on the surface of α-Fe_2O_3. Then the abundant oxygen-containing function groups on the Ni-NC would be easy to filled in these deficient sites driven by the high temperature (Scheme 4.1b). Eventually, new chemical bond of Fe–O–C could be formed at the interface of α-Fe_2O_3 and Ni-NC, which acted as extra interfacial channels for the facilitated charge transfer (Scheme 4.1c). Consequently, the interfacial carrier path induced by the chemical interaction and the distinct single-nickel sites work collaboratively to achieve efficient PEC water oxidation.

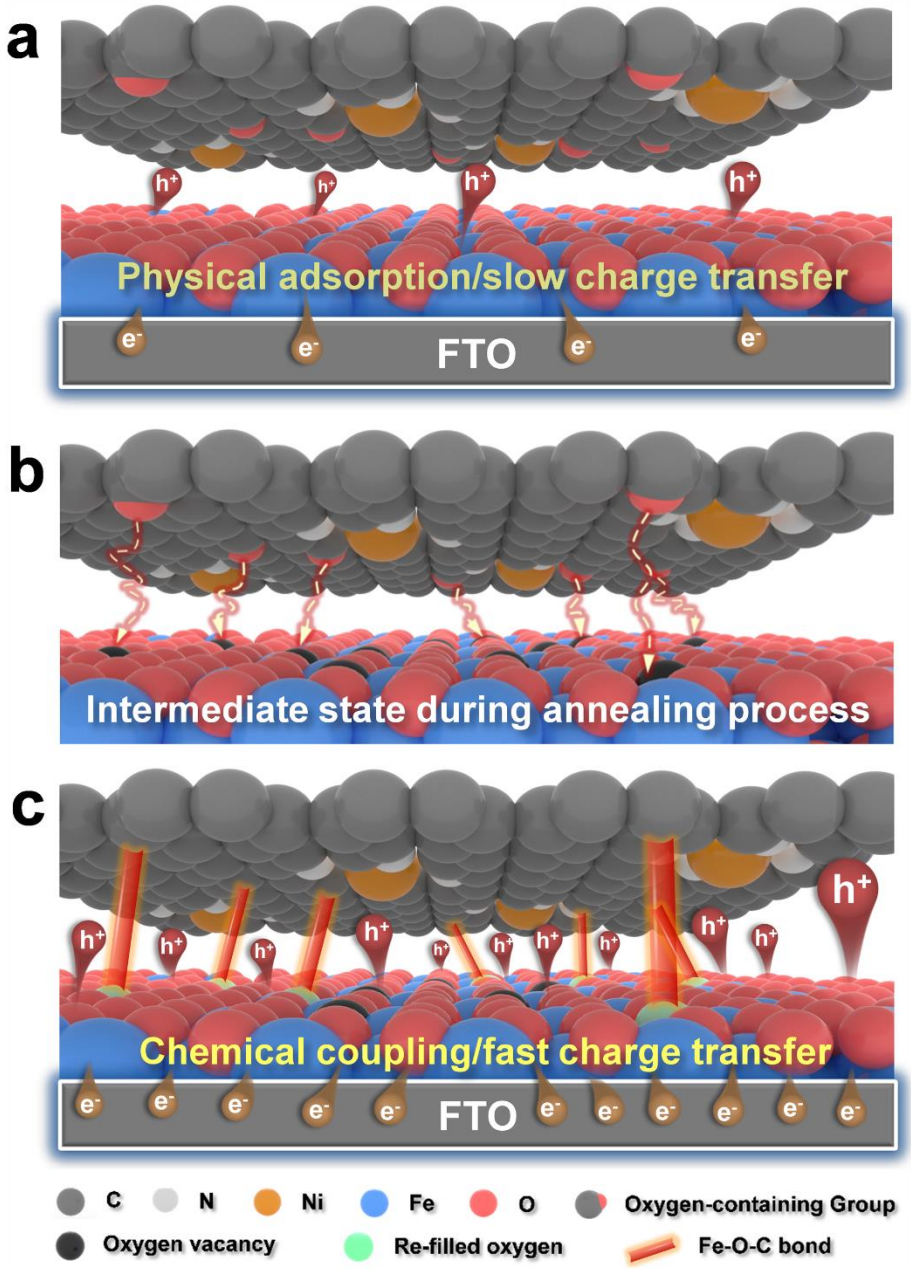

Scheme 4.29 a) Illustration of physical adsorption and slow charge transfer in α-Fe_2O_3-Ni-NC system without annealing treatment. (b) Intermediate state during the annealing process with the generation of oxygen vacancies on α-Fe_2O_3. (c) Scheme of fast charge transfer with the chemical coupling created by facile calcination treatment for α-Fe_2O_3-Ni-NC-300.

3.4 Conclusions

In conclusion, our study demonstrates an efficient PEC water oxidation system of α-Fe_2O_3-Ni-NC-300, resulting in a high photocurrent density of 1.85 mA cm^{-2} (2.2-fold enhancement than the pure α-Fe_2O_3) at 1.23 V vs. RHE under AM 1.5 G illumination.

The insight into the remarkable enhancement verifies that chemical interaction is constructed at the interface between α-Fe_2O_3 and Ni-NC. The chemical coupling can facilitate efficient charge carries transfer occurred at the interface and the isolated Ni active sites can fully utilize the collected holes from α-Fe_2O_3, hence achieving an impressive PEC water oxidation. This work elucidates the vital role of chemical interaction between semiconductor and OEC in PEC water oxidation process and explores the huge potential of integrating interface modulation and single-atom catalysts for efficient photoelectrocatalysis.

References

[1] A. Fujishima, K. Honda, *Nature* **1972**, *238*, 37.

[2] M. Grätzel, *Nature* **2001**, *414*, 338.

[3] T. Hisatomi, J. Kubota, K. Domen, *Chem. Soc. Rev.* **2014**, *43*, 7520.

[4] S. Wang, G. Liu, L. Wang, *Chem. Rev.* **2019**, *119*, 5192.

[5] I. Roger, M. A. Shipman, M. D. Symes, *Nat. Rev. Chem.* **2017**, *1*, 0003.

[6] Y. He, T. Hamann, D. Wang, *Chem. Soc. Rev.* **2019**, *48*, 2182.

[7] W. Wang, M. Xu, X. Xu, W. Zhou, Z. Shao, *Angew. Chem. Int. Ed.* **2020**, *59*, 136.

[8] M. G. Walter, E. L. Warren, J. R. McKone, S. W. Boettcher, Q. Mi, E. A. Santori, N. S. Lewis, *Chem. Rev.* **2010**, *110*, 6446.

[9] Z. Luo, B. Liu, H. Li, X. Chang, W. Zhu, T. Wang, J. Gong, *Small Methods 2019*, *3*, 1900212.

[10] N.-T. Suen, S.-F. Hung, Q. Quan, N. Zhang, Y.-J. Xu, H. M. Chen, *Chem. Soc. Rev.* **2017**, *46*, 337.

[11] K. Sivula, F. Le Formal, M. Grätzel, *ChemSusChem* **2011**, *4*, 432.

[12] Y. Lin, G. Yuan, S. Sheehan, S. Zhou, D. Wang, *Energy Environ. Sci.* **2011**, *4*, 4862.

[13] Y. Lin, S. Zhou, S. W. Sheehan, D. Wang, *J. Am. Chem. Soc.* **2011**, *133*, 2398.

[14] Y. Ling, G. Wang, D. A. Wheeler, J. Z. Zhang, Y. Li, *Nano Lett.* **2011**, *11*, 2119.

[15] G. Yang, Y. Li, H. Pang, K. Chang, J. Ye, *Adv. Funct. Mater.* **2019**, *29*, 1904622.

[16] S. S. Yi, B. R. Wulan, J. M. Yan, Q. Jiang, *Adv. Funct. Mater.* **2019**, *29*, 1801902.

[17] W. Liu, H. Liu, L. Dang, H. Zhang, X. Wu, B. Yang, Z. Li, X. Zhang, L. Lei, S. Jin, *Adv. Funct. Mater.* **2017**, *27*, 1603904.

[18] Y. Hou, X. Zhuang, X. Feng, *Small Methods* **2017**, *1*, 1700090.

[19] F. Lin, S. W. Boettcher, *Nat. Mater.* **2014**, *13*, 81.

[20] R. Li, Y. Liu, H. Li, M. Zhang, Y. Lu, L. Zhang, J. Xiao, F. Boehm, K. Yan, *Small Methods* **2019**, *3*, 1800344.

[21] L. Zhang, Y. Jia, G. Gao, X. Yan, N. Chen, J. Chen, M. T. Soo, B. Wood, D. Yang, A. Du, *Chem* **2018**, *4*, 285.

[22] H. Fei, J. Dong, Y. Feng, C. S. Allen, C. Wan, B. Volosskiy, M. Li, Z. Zhao, Y. Wang, H. Sun, *Nat. Catal.* **2018**, *1*, 63.

[23] X.-F. Yang, A. Wang, B. Qiao, J. Li, J. Liu, T. Zhang, *Acc. Chem. Res.* **2013**, *46*, 1740.

[24] C. Gao, S. Chen, Y. Wang, J. Wang, X. Zheng, J. Zhu, L. Song, W. Zhang, Y. Xiong, *Adv. Mater.* **2018**, *30*, 1704624.

[25] J. Wang, Z. Li, Y. Wu, Y. Li, *Adv. Mater.* **2018**, *30*, 1801649.

[26] Y. Zhu, W. Sun, J. Luo, W. Chen, T. Cao, L. Zheng, J. Dong, J. Zhang, M. Zhang, Y. Han, *Nat. Commun.* **2018**, *9*, 1.

[27] Y. Hou, M. Qiu, M. G. Kim, P. Liu, G. Nam, T. Zhang, X. Zhuang, B. Yang, J. Cho, M. Chen, *Nat. Commun.* **2019**, *10*, 1.

[28] Y. Hou, M. Qiu, T. Zhang, J. Ma, S. Liu, X. Zhuang, C. Yuan, X. Feng, *Adv. Mater.* **2017**, *29*, 1604480.

[29] H. Kaneko, T. Minegishi, K. Domen, *Chem. Eur. J.* **2018**, *24*, 5697.

[30] J. Zhou, H. Song, L. Ma, X. Chen, *Rsc Adv.* **2011**, *1*, 782.

[31] Z. Zhang, F. Ahmad, W. Zhao, W. Yan, W. Zhang, H. Huang, C. Ma, J. Zeng, *Nano Lett.* **2019**, *19*, 4029.

[32] P. Chen, N. Zhang, S. Wang, T. Zhou, Y. Tong, C. Ao, W. Yan, L. Zhang, W. Chu, C. Wu, *Proc. Natl. Acad. Sci.* **2019**, *116*, 6635.

[33] C. Zhao, X. Dai, T. Yao, W. Chen, X. Wang, J. Wang, J. Yang, S. Wei, Y. Wu, Y. Li, *J. Am. Chem. Soc.* **2017**, *139*, 8078.

[34] H. J. Qiu, Y. Ito, W. Cong, Y. Tan, P. Liu, A. Hirata, T. Fujita, Z. Tang, M. Chen, *Angew. Chem. Int. Ed.* **2015**, *54*, 14031.

[35] H. B. Yang, S.-F. Hung, S. Liu, K. Yuan, S. Miao, L. Zhang, X. Huang, H.-Y. Wang, W. Cai, R. Chen, *Nat. Energy* **2018**, *3*, 140.

[36] Y. Ling, G. Wang, H. Wang, Y. Yang, Y. Li, *ChemSusChem* **2014**, *7*, 848.

[37] T. Fujii, F. De Groot, G. Sawatzky, F. Voogt, T. Hibma, K. Okada, *Phys. Rev. B* **1999**, *59*, 3195.

[38] Z. Wang, X. Mao, P. Chen, M. Xiao, S. A. Monny, S. Wang, M. Konarova, A. Du, L. Wang, *Angew. Chem. Int. Ed.* **2019**, *131*, 1042.

[39] Y. Makimizu, J. Yoo, M. Poornajar, N. T. Nguyen, H.-J. Ahn, I. Hwang, S. Kment, P. Schmuki, *J. Mater. Chem. A* **2020**.

[40] Y. Ling, G. Wang, J. Reddy, C. Wang, J. Z. Zhang, Y. Li, *Angew. Chem. Int. Ed.* **2012**, *51*, 4074.

[41] B. Jin, Y. Cho, Y. Zhang, P. Li, K. Zhang, K.-S. Lee, J. H. Park, *Nano Energy* **2019**, *66*, 104110.

[42] X. Cheng, G. Dong, Y. Zhang, C. Feng, Y. Bi, *Appl. Catal. B: Environ.* **2020**, *267*, 118723.

[43] C. Combellas, M. Delamar, F. Kanoufi, J. Pinson, F. I. Podvorica, *Chem. Mater.* **2005**, *17*, 3968.

[44] J. Balajka, M. A. Hines, W. J. DeBenedetti, M. Komora, J. Pavelec, M. Schmid, U. Diebold, *Science* **2018**, 361, 786.

[45] B. M. Comer, Y.-H. Liu, M. B. Dixit, K. B. Hatzell, Y. Ye, E. J. Crumlin, M. C. Hatzell, A. J. Medford, *J. Am. Chem. Soc.* **2018**, *140*, 15157.

[46] X. Ning, B. Lu, Z. Zhang, P. Du, H. Ren, D. Shan, J. Chen, Y. Gao, X. Lu, *Angew. Chem. Int. Ed.* **2019**, *58*, 16800.

[47] Z. Zhang, I. Karimata, H. Nagashima, S. Muto, K. Ohara, K. Sugimoto, T. Tachikawa, *Nat. Commun.* **2019**, *10*, 1.

[48] L. Cai, J. Zhao, H. Li, J. Park, I. S. Cho, H. S. Han, X. Zheng, *ACS Energy Lett.* **2016**, *1*, 624.

[49] C. Li, A. Li, Z. Luo, J. Zhang, X. Chang, Z. Huang, T. Wang, J. Gong, *Angew. Chem. Int. Ed.* **2017**, *56*, 4150.

[50] J. Deng, X. Lv, K. Nie, X. Lv, X. Sun, J. Zhong, *ACS Catal.* **2017**, *7*, 4062.

[51] H.-J. Ahn, K.-Y. Yoon, M.-J. Kwak, J. Park, J.-H. Jang, *ACS Catal.* **2018**, *8*, 11932.

[52] L. Wang, N. T. Nguyen, X. Huang, P. Schmuki, Y. Bi, *Adv. Funct. Mater.* **2017**, *27*, 1703527.

[53] Z. Luo, T. Wang, J. Zhang, C. Li, H. Li, J. Gong, *Angew. Chem. Int. Ed.* **2017**, *56*, 12878.

[54] M. Li, Y. Yang, Y. Ling, W. Qiu, F. Wang, T. Liu, Y. Song, X. Liu, P. Fang, Y. Tong, *Nano Lett.* **2017**, *17*, 2490.

[55] J. Y. Kim, D. H. Youn, K. Kang, J. S. Lee, *Angew. Chem. Int. Ed.* **2016**, *55*, 10854.

[56] Q. Yu, X. Meng, T. Wang, P. Li, J. Ye, *Adv. Funct. Mater.* **2015**, *25*, 2686.

[57] S. A. Carminati, A. do Nascimento Barbosa, A. L. M. de Freitas, F. L. Freire Jr, F. L. Souza, A. F. Nogueira, *J. Catal.* **2019**, *372*, 109.

[58] P. Zhang, T. Wang, X. Chang, L. Zhang, J. Gong, *Angew. Chem. Int. Ed.* **2016**, 55, 5851.

[59] K. Feng, A. Wei, Z. Kang, J. Zhong, *Appl.Catal. B: Environ.* **2019**, *258*, 117962.

[60] Y. Hou, M. Qiu, M. G. Kim, P. Liu, G. Nam, T. Zhang, X. Zhuang, B. Yang, J. Cho, M. Chen, *Nat. Commun.* **2019**, *10*, 1.

Chapter 5 Conclusions and future prospects

5.1 General conclusions

In this thesis, the main objective is to design and develop efficient hematite-based photoanodes via novel co-catalyst design and modulating the interface between the α-Fe_2O_3 and co-catalyst by inserting a hole transfer mediator/constructing direct chemical interaction for efficient charge transfer. Also, the findings in this study develop new understandings of co-catalyst design for the α-Fe_2O_3-based PEC water oxidation system and highlight the importance of semiconductor/co-catalyst interface modulation for the overall photoelectrocatalytic processes.

The detailed study could be concluded in the following parts.

1. Ultrathin cobalt-manganese nanosheets: an efficient platform for enhanced photoelectrochemical water oxidation with electron-donating effect

In this part, ultrathin Co-Mn nanosheets was constructed as co-catalyst for α-Fe_2O_3 films and the electron-withdrawing/donating effect between $Co(OH)_x$ and Mn_3O_4 was investigated to enhance the activity of photoanodes for PEC water oxidation. This approach favors in attaining an advantageous co-catalyst/semiconductor interface to reduce recombination of photogenerated charge carries and enhance their transfer efficiency. Compared with bare α-Fe_2O_3 photoanode, the optimized photoanode exhibited a remarkable photocurrent density of 2.09 mA cm^{-2} at 1.23 V vs. RHE under AM 1.5 G illumination and an impressive cathodic shift (~ 200 mV) of onset potential. Furthermore, Co-Mn nanosheets could also significantly enhance the ABPE values of α-Fe_2O_3 even at a lower potential and provide a remarkable resistance against photo-corrosion with an excellent stability for over 10 h. Detailed mechanism investigation unveiled the pivotal role of electron-donation effect from Mn_3O_4 to $Co(OH)_x$ resulting in efficient charge injection processes and thus dramatically enhanced PEC water oxidation performance. This work provides deep understanding on the electron-withdrawing/donating effect for catalytic materials with multi-metallic sites, which possesses huge potentials in solving the current dilemma for large-scale applications of PEC water splitting.

2. A universal strategy boosting photoelectrochemical water oxidation by utilizing MXene nanosheets as hole transfer mediators

In this part, it was demonstrated that the insertion of MNs served as excellent hole transfer mediators in α-Fe_2O_3/co-catalyst photoanodes for PEC water oxidation. The introduction of the ultrathin MNs enabled the formation of Schottky junction with α-Fe_2O_3, providing a strong built-in electric field with an additional driving force to suppress the charge recombination. Then the co-catalyst could perform a much better catalytic activity due to the facilitated hole transfer from α-Fe_2O_3 to the co-catalyst surface. As a result, the Co-Pi/MNs/α-Fe_2O_3 photoanode exhibited a 2-fold enhancement of photocurrent density from 0.84 to 2.54 mA cm^{-2} at 1.23 V vs. RHE and a cathodic shift of onset potential by ~250 mV from 0.82 to 0.57 V vs. RHE under AM 1.5 G illumination, comparing with the bare α-Fe_2O_3. A remarkable photocurrent density of 3.20 mA cm^{-2} at 1.23 V vs. RHE and a high ABPE of 0.49% were achieved on Co-Pi/MNs/α-Fe_2O_3 under front illumination, which is among the very best PEC performance for α-Fe_2O_3 based photoanodes. This impressive function of MNs was also applicable for other co-catalysts (such as NiOOH and FeOOH) and photoanode materials (such as $BiVO_4$, WO_3 and ZnO). Furthermore, the optimized burying of MNs by the co-catalyst layer alleviated the self-oxidation, thereby prolonging the stability of Co-Pi/MNs/α-Fe_2O_3 for 20 h. Our work proposes a universal strategy for enhancing the charge transfer efficiency of the photoanodes by inserting a mediator between the semiconductor and co-catalyst and highlights the potential for application of MNs in solar energy conversion devices.

3. Constructing chemical interaction between hematite and carbon nanosheets with single active sites for efficient photoelectrochemical water oxidation

In this part, an efficient PEC water oxidation system of α-Fe_2O_3-Ni-NC-300 was designed, resulting in a high photocurrent density of 1.85 mA cm^{-2} (2.2-fold enhancement than the pure α-Fe_2O_3) at 1.23 V vs. RHE under AM 1.5 G illumination. The insight into the remarkable enhancement verified that chemical interaction was constructed at the interface between α-Fe_2O_3 and Ni-NC. The chemical coupling could facilitate efficient charge carries transfer occurred at the interface and the isolated Ni active sites could fully utilize the collected holes from α-Fe_2O_3, hence achieving an impressive PEC water oxidation. This work elucidates the vital role of chemical interaction between semiconductor and OEC in PEC water oxidation process and explores the huge potential of integrating interface modulation and single-atom catalysts for efficient photoelectrocatalysis.

5.2 Future prospects

Although some achievements have been made in developing efficient hematite-based materials for PEC water oxidation, there are many challenges towards the significant enhancement in PEC water splitting, especially for bias-free photocathode coupled with photoanode PEC system. Some issues listed below are worthy of special attention:

(1) To date, the properties of co-catalysts are still far from satisfying the requirement of practical usage. There is a large space to further improve the performance of co-catalysts. Novel materials like metal-free materials, molecular materials, or MOFs are all worthy to be explored for expanding the family of co-catalysts and offering more options. In addition, the working mechanisms of co-catalysts have not yet been stated clearly. Thus, further rationally designed experiment verifications, through characterizations, maintain to be conducted in order to provide much more powerful evidences and specific explanations. In addition, theoretical calculations, especially density functional theory study, are of equal importance to make up the defects of experimental measurements.

(2) Although significant progress has been made in the past decade, continuous innovations and new understandings of interface engineering are required to meet the demand for the development of photoanodes with higher efficiencies and to drive the PEC water splitting finally into practical application. In particular, future innovations should be made in materials and approaches. The selection of materials for the use of surface protection, surface-state passivation, and selective charge extraction is currently quite limited. New deposition approaches would be needed to adapt these coating materials to semiconductors sensitive to the deposition conditions. Meanwhile, gaining deeper understanding of the interface energetics, the dynamic behaviors of interfaces during operation, and the electrolyte and temperature dependence of interface properties is also important for the design of robust interfaces.

(3) Bias-free photocathode coupled with photoanode system and stand-alone photovoltaic cell integrating photo-electrocatalytic cell tandem device with suitable photoelectrode materials are two promising design strategies to efficiently convert water into hydrogen under sunlight illumination. Although some achievements have been obtained, many challenges remain to be solved in the future. For instance, promotion of light harvesting efficiency and enhanced separation of photogenerated electron–hole pairs for both photocathode and photoanode materials, the development of more efficient co-catalysts, superior photoanode and photocathode materials with matched band positions

to form a Z-scheme junction system, matched bandgap of photoelectrode and semiconductor in solar cell to absorb more ample visible light, optimal configuration for both photocathode–photoanode system and PV-PEC cells.

Acknowledgement

At first, I would like to express my deep and sincere gratitude to my supervisor Prof. Jinhua Ye for her valuable guidance, kind help and constant encouragement throughout my Ph.D. studies and personal life. Her proficiency, intelligence, and unparalleled instruction ensure the progress of my Ph.D. research project, and these impacts will benefit me through my whole life. I would also like to extend my sincere appreciation of the academic freedom and great platform that Prof. Ye offered. I am so appreciative and lucky to meet such a nice supervisor.

I am also grateful to my supervisors, Prof. Takao Masuda and Prof. Naoto Shirahata. Thank you for all your suggestions and kind help during my PhD study.

Then, I would like to thank Dr. Yunxiang Li, who gave me a lot of advice for my research. I also want to thank all the members in the Photocatalytic Materials Group in NIMS and the persons who have helped me. I would like to express my thanks to Dr. Huiwen Lin, Dr. Xusheng Wang, Ms. Sijie Li, Mr. Shunqin Luo, Mr. Xiaohui Ren, Mr. Qi Wang, Mr. Bowen Deng, Ms. Lan Li, Prof. Kun Chang, Dr. Shengyao Wang, Dr. Hui Song, Dr. Li Shi, Dr. Xuelian Yu, Dr. Kang Peng, Mr. Davin Philo, Dr. Hong Pang, Dr. Fumihiko Ichihara, Dr. Tetsuya Kako and Ms. Kanae Hasegawa and Ms. Haruna Kurokawa for their kind helps in both experiments and daily life.

At last, I would like to thank my parents, other family members and friends for their support and belief in me.